CONSTRAINING NEUTRON-CAPTURE CROSS SECTIONS ON ^{151,153}ND FOR THE *INTERMEDIATE* NEUTRON-CAPTURE PROCESS

By

Hannah Christine Berg

A DISSERTATION

Submitted to
Michigan State University
in partial fulfillment of the requirements
for the degree of

Physics—Doctor of Philosophy

2026

ABSTRACT

For decades, scientists believed that the most of the universe's heavy elements were created by only two main processes in stars—one slow (s) and one rapid (r). However, stellar observations have revealed chemical signatures that cannot be interpreted by combining these processes. Because of this discrepancy, the astrophysical i process was introduced (i for intermediate between s and r). The astrophysical site for the i process is not known, therefore multiple possible sites have been proposed. To be able to understand where it can take place, uncertainties for important neutron-capture reactions need to be reduced.

This thesis focuses on new results from an experiment at Argonne National Laboratory, to constrain neutron-capture reactions of importance to the i process. We specifically studied the β decay of rare isotopes of praseodymium $\left(^{152,154}\mathrm{Pr}\right)$ into neodymium $\left(^{152,154}\mathrm{Nd}\right)$. The experiment measured the γ-rays and excitation energy of ^{152,154}Nd. The uncertainties of these reactions are believed to influence the production of europium and samarium in simulations of a potential i process site.

Because the actual i process happens in extreme stellar environments involving short lived nuclei, we cannot replicate some of these reactions. Due to the short half-lives of the nuclei involved, it is impossible to create targets. Instead, we used an indirect method to determine how these nuclei behave when they decay. By measuring two key nuclear properties: the nuclear level density (how many energy states a nucleus can inhabit) and the γ-ray strength function (probability to emit γ rays as a function of energy), we were able to constrain the probability of capturing neutrons on ^{151,153}Nd for the first time.

Using these newly constrained reaction rates, we could see how this reduction in nuclear uncertainties affected astrophysical simulations of potential i-process sites. Now, given a specific stellar environment, we can better predict how much europium or samarium will be produced.

ACKNOWLEDGMENTS

Dear reader, please consider this a preliminary version of my acknowledgements. This will be a short version so that I can show my gratitude to you before the final thesis submission.

First I want to thank my fantastic research group at FRIB for all of the support, teamwork, joy, and learning you have helped me experience. My amazing office mates, it has been amazing sharing a space and so many good moments.

A special thank you to my supervisor Artemis Spyrou, you have been vital for my growth as a researcher and you have encouraged me to push myself out of my comfort zone. You are a great teacher and have helped me become a better teacher in turn.

Thank you to my committee members, those who were there for the first committee meetings, and to those here at the culmination. Thank you to Heiko Hergert, Sean Liddick, Alyssa Gaiser and Dan Hayden for the enthusiasm, questions, and support during my work.

To the people at University of Oslo, thank you for welcoming me and including me every time I am lucky enough to visit. A special thank you to Sunniva Siem for the great research discussions, your mentoring and support all the way from when I was an undergraduate till today.

My friends, my roomates, my people, far and wide, my time in grad school would have been impossible without you. You have made life fun, you have taught my new skills, and I hope you know I am missing all of you. My family, you have always been my biggest cheerleaders, you are there when needed and also when I do not know I need support. Mamma og pappa, jeg er kjempeglad i dere og setter pris paa dere. Peter, du er en fantastisk fin person of venn. Elizabeth, du er brukbar og brukanes og jeg er takknemmelig for dine skarpe øyne her. David, Berit, Ariana og Amalie, dere er en konstant kilde av glede i livet mitt. Victoria, jeg blir glad hver gang du ringer og ekstra glad når jeg kan få deg til å le.

Finally, the biggest and most important thank you to my dear David. You have been a rock and I do not think words can do justice to how much I appreciate you. With all my love, you are the best.

TABLE OF CONTENTS

LIST OF TABLES

LIST OF FIGURES

CHAPTER 1

INTRODUCTION

Have you ever looked at the night sky and wondered what happens in the stars? How are they created, how do they burn, and how do stars die? Have you ever wondered how elements are made? These are some of the big questions for humankind, and more specifically in nuclear astrophysics: how are heavy elements created in stars? This thesis will help solve a small part of this mystery by looking at how the element europium can be created in stars.

Let us imagine someone staring at the stars and wondering how they and the universe came to be. Instead of pondering when humankind first started to wonder where matter came from, a brief overview of a more recent scientific history of nuclear astrophysics is given here. Before nuclear physics was invented[1], there have been many scientific theories that tried to explain the mechanisms that made stars burn.

A historically impactful review paper in nuclear astrophysics titled "Synthesis of the Elements in Stars" in nuclear astrophysics was published in 1957 by E. Margaret Burbidge, G. R. Burbidge, William A. Fowler, and F. Hoyle [1] (B2FH). Even today, many of the processes described within have been proven correct, and it is frequently referenced in nuclear astrophysics. Some things have changed with the birth of multi-messenger nuclear astrophysics, as we can combine different astronomical observation techniques, and collaborate across disciplines to fully try to understand where heavier elements are created and how they come to be. Where humankind cannot go, we instead extrapolate our knowledge. This is especially true in nuclear astrophysics, as nucleosynthesis occurs far away, all across the universe.

In this thesis, an introduction to important nuclear physics terminology, nuclear astrophysics, and the modeling of reactions and nucleosynthesis is presented in Chapter 2 and Chapter 3. The experimental setup and methods are detailed in Chapter 4, with the background subtraction detailed in Chapter 5. From the background-subtracted data, the β-Oslo method was applied to find the functional form of the nuclear level density, and the γ-strength function for ^{151,153}Nd in Chapter 6.

[1] Or one can argue, discovered.

The functional forms of these statistical properties were normalized to available neodymium data in Chapter 7. With the statistical properties of ^{151,153}Nd constrained, the results of the constrained cross sections and reaction rates for ^{151,153}Nd(n,γ)^{152,154}Nd are presented in Chapter 8, along with their impact on the astrophysical i process. Finally, the summary and conclusions are presented in Chapter 9.

CHAPTER 2

NUCLEAR PHYSICS PRIMER

To put this thesis work into context, it is essential to understand nuclear properties and how they affect the current understanding of nucleosynthesis in various stellar sites. This chapter focuses on relevant nuclear properties.

2.1 Basic nuclear properties

In nuclear physics, understanding the fundamental properties of nuclei is essential before exploring more complex phenomena. A primary tool in nuclear science is the chart of nuclides, which plots the neutron number (N) against the proton number (Z), as seen in Figure 2.1. This chart displays all discovered nuclei along with their specific properties. Consequently, having a clear understanding of the chart of nuclides and knowing how to interpret nuclear properties and systematics is vital.

To distinguish nuclei from one another, a specific notation is used. Each nucleus is composed of A nucleons, where A represents the mass number. A nucleus is typically denoted as ${}^{A}X$, where X is the chemical symbol for the element. If the proton number, Z, is relevant to the discussion, it can be explicitly denoted as ${}^{A}_{Z}X$. The number of neutrons is then determined by the mass number minus the number of protons: $N = A - Z$.

2.1.1 Isotopes, isotones, and isobars

Isotopes are nuclei with the same number of protons, but different numbers of neutrons, ${}_{Z}X$. Isotones have the same number of neutrons, N, but a different number of protons. Finally, isobars are nuclei with the same mass number A. In Figure 2.1, each row shows the isotopes, each column shows the isotones, and the isobars appear on the diagonal, with the same mass numbers. Additionally, the magic numbers for nucleons are marked in Figure 2.1. Magic numbers are when orbitals in the nucleus are filled for neutrons or protons, akin to the electron shells in elements for the noble gases. The magic numbers are $N = Z = 2, 8, 20, 28, 50, 82$. Nuclei with magic numbers of neutrons and/or protons are more stable than their neighbors.

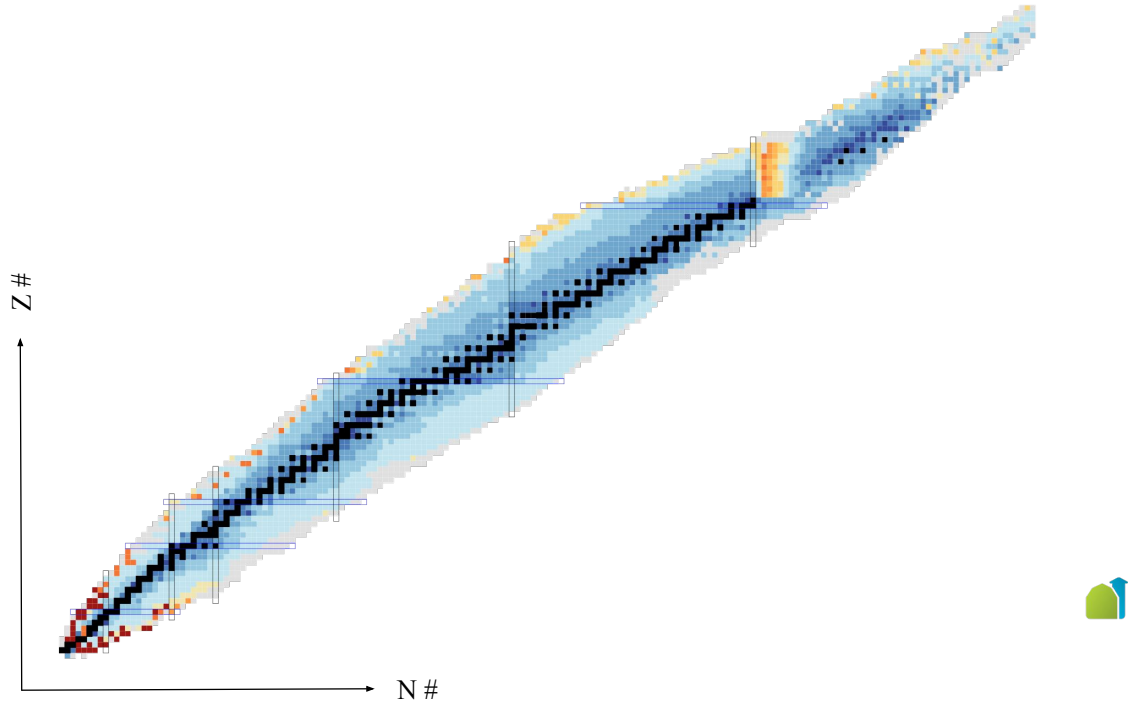

Figure 2.1 Chart of nuclei, with the neutron number versus the proton number. The highlighted columns and rows are the magic numbers. Black represents stable isotopes ($t_{1/2} > 10^{15}$ s), while the the rest are unstable nuclei, with the range going from the shortest half-lives in red ($t_{1/2} < 10^{-15}$ s) towards the darkest blue ($t_{1/2} = 10^{15}$ s) as the half-lives increases. Figure from [2].

2.1.2 Spin and parity

Two of the most important properties for a nucleus are the spin and parity, denoted as J^{π}. The spin of a nucleus is the total angular momentum, $\vec{J}$. Protons and neutrons have intrinsic spin, s of $1/2$. Additionally, the nucleus also has the orbital angular momentum, l. With this, $\vec{J} = \vec{s} + \vec{l}$. The parity ($\pi$), denotes if the wave function of the nucleus is invariant under spatial inversion. The parity is related to the orbital angular momentum l via $\pi = (-1)^l$.

A simplified way to find the spin and parity (J^{π}) of a nucleus, is by looking at the unpaired nucleons to determine J and the product of all the parities π. With this in mind, the ground state of all even-even nuclei is 0^+. If the nucleus is odd-even or even-odd, only the unpaired nucleon affects the spin and parity, leading to half-integer spins. For the odd-odd nuclei, the ground state spin is usually determined from the combined angular momenta of the unpaired neutron and unpaired proton, leading to integer spins.

2.1.3 Binding energy and Q-values

The binding energy (BE) of a nucleus denotes the amount of energy needed to break the nucleus apart into its constituent protons and neutrons. A common way to illustrate the strength of the binding energy is to divide it by the mass number A; this average binding energy is denoted as BE/A. The average binding energy per nucleon is shown in Figure 2.2, with some important nuclei highlighted. For the lighter mass nuclei, the effect of magic numbers is evident in the doubly-magic ^{4}He and ^{16}O.

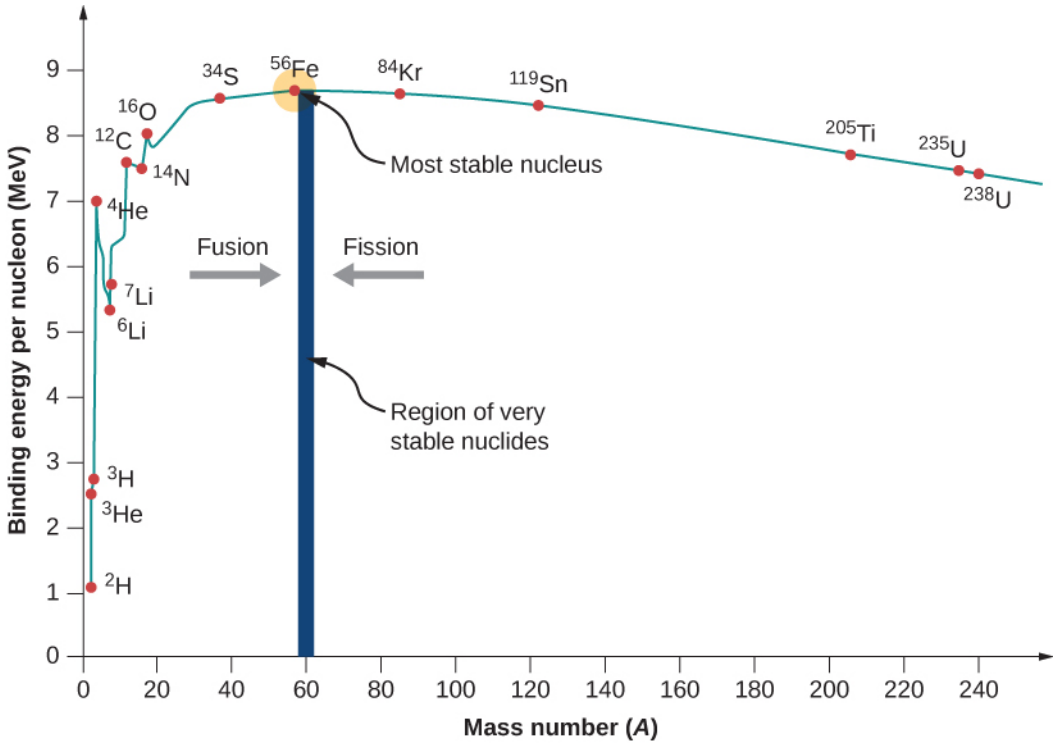

Figure 2.2 Plot showing the average binding energy in MeV per nucleon (A). Figure is Fig. 10.3.2 from [3].

The easiest way to figure out which elements can be made in stars is to look at the binding energy (BE) of the nucleus. The binding energy is how much energy goes into keeping the nuclei together in the nucleus. When fusing nuclei together, the binding energy of the new compound nucleus has to increase for it to be able to generate energy.

For any given nucleus, one can measure the energy required to remove a neutron or a proton, defined as the neutron separation energy (S_n) and the proton separation energy (S_p), respectively.

This is essentially the binding energy of the last nucleon.

In nuclear reactions and radioactive decays, the Q-value denotes the amount of energy released or absorbed. From this, a positive Q-value indicates a spontaneous process, while a negative value indicates that additional energy is required to proceed.

2.2 β-decay

One of the types of radioactive decay is β decay, which can happen when a nucleus is unstable, and has a positive Q_β value.

In the case of a neutron-rich nucleus, it can β^- decay as described in Equation (2.1),

$$n \rightarrow p + e^- + \overline{\nu}_e, \tag{2.1}$$

where a neutron (n) is converted into a proton (p), an electron (e^-), and an antineutrino ($\overline{\nu}_e$). Conversely, on the proton-rich side, a nucleus can undergo β^+ decay via

$$p \rightarrow n + e^+ + \nu_e. \tag{2.2}$$

Additionally, in proton-rich nuclei, β^+ decay competes with an additional process, namely electron capture, as described in Equation (2.3):

$$p + e^- \rightarrow n + \nu_e. \tag{2.3}$$

For β decay, both the spin (J) and the parity (π) are important. In this work, we assume that the β decay follows the selection rules for allowed transitions. There are two types of allowed transitions in β decay: Fermi, and Gamow-Teller. Fermi transitions involve the leptons being emitted with a total orbital angular momentum of zero and their spins coupled to zero ($S = 0$). This means that the spins of the leptons are pointing in opposite directions, resulting in no change in the total angular momentum of the nucleus. In Gamow-Teller decay, the spins of the leptons sum to $S = 1$, which allows the total angular momentum of the nucleus to change by up to one unit.

For allowed transitions, both Fermi and Gamow-Teller decays involve no change in parity ($\Delta\pi$ = no) or angular momentum ($L = 0$). The allowed change in the total nuclear angular momentum is $\Delta I = 0, \pm 1$. This is critical for the analysis, as it informs which discrete states in the

daughter nucleus can be populated via allowed decays. Higher order transitions are possible; they are referred to as forbidden transitions. However, the forbidden transitions are suppressed compared to allowed decays.

2.3 γ decay

In the case of an excited nucleus de-exciting via γ, the photon transfers a specific amount of angular momentum, L. The amount of angular momentum transferred is the multipole of the transition. A dipole transition corresponds to $L = 1$, a quadrupole to $L = 2$, an octupole to $L = 3$, and so forth. The multipole order is constrained by the spin of the initial state (J_i) and the spin of the final state $\left(J_f\right)$ by:

$$\left|J_i - J_f\right| \leq L \leq J_i + J_f. \tag{2.4}$$

For γ transitions from $0^+ \rightarrow 0^+$, the angular momentum must be greater than 0, as the intrinsic spin of a photon is 1. For the $L = 0$ case, internal conversion may instead occur, as described in Section 2.4.

Transitions are either electric (E) or magnetic (M) in nature. Multipole transitions are generally denoted as XL, where X is either E or M. An electric transition corresponds to changes in the charge distribution of the nucleus, while a magnetic transition is caused by changes in the magnetic moments. For dipole transitions, parity is conserved in magnetic transitions, while it changes in $E1$ transitions. In general, the parity change $\Delta\pi$ is determined by

$$\pi_E(L) = (-1)^L, \tag{2.5}$$

$$\pi_M(L) = (-1)^{L+1}. \tag{2.6}$$

$$\tag{2.7}$$

The probability of a γ transition decreases as L increases. In general, electric transitions (EL) are more probable than magnetic transitions (ML) of the same order. The probabilities of these transitions are often measured in Weisskopf units, which assume that the transition probability depends on a single nucleon contributing to the decay.

2.4 Internal conversion

Internal conversion is a form of decay where the nucleus de-excites via energy transfer to one of the electrons in the atom. This energy transfer leads to the ejection of the conversion electron. The conversion electron usually comes from the closest major electron shell (K), but it is possible that it comes from the L and M shells [4].

Internal conversion is dominant for $0^+ \rightarrow 0^+$ transition ($L = 0$). For higher multipoles, there can be competition between decay via γ emission and internal conversion. This internal conversion is often more likely when there is a small energy gap between two states or a large difference in spins between the initial and final states, and the γ emission is suppressed.

The probability of internal conversion is measured by the internal conversion coefficient, α. The higher the α coefficient, the more likely it is to internally convert, rather than decay via γ emission. For stable and less exotic isotopes, it is possible to measure the likelihood of internal conversion when the level structure is well known. For more unstable nuclei, there are calculation methods which can predict the internal conversion probability [4].

This internal conversion is important in many ways, and impacts the β-Oslo method. In the β-Oslo method, the excitation energy, E_x, is found by summing the γ-ray energy, E_γ. If there are internal conversions present, these affect the extracted total excitation energy, as there will be energy missing due to internal conversions. This will lead to some systematic uncertainties, as the excitation energy will be systematically underestimated. The different ways to account for this internal conversion will be further discussed in Chapter 6.

2.5 Deformation

A nucleus with no deformation can be viewed as a perfect sphere. This is not the case for all nuclei; the degree of deformation is measured by the quadrupole deformation parameter, β_2, where $\beta_2 = 0$ represents a spherical shape. The two most common forms of deformation are prolate or oblate deformation, often likened to the shapes of a pumpkin and an American football. Prolate nuclei have $\beta_2 > 0$, while oblate nuclei have $\beta_2 < 0$. Within isotopic chains, deformations usually follow specific systematics. For instance, it can often increase with the neutron number.

Additionally, it is also possible to observe shape coexistence [5], where both spherical states and deformed states are present in the same nucleus.

Increasing deformation changes the configuration of rotational bands and affects the level structure. This is significant as we are interested in the trends of resonances in nuclei and how they depend on deformation. The stable neodymium isotopes have been studied in length since the 1970s, including how the GDR changes into two components as the neutron number N increases for even-numbered isotopes. The deformation of neodymium isotopes increases with the number of neutrons, going from no deformation for ^{142}Nd to well deformed around ^{152}Nd. As the neutron number increases even further, it is believed that the ground state of the nucleus remains deformed.

2.6 Compound nucleus reactions

One useful property in nuclear reactions is that of the compound nucleus. During a reaction, a short-lived compound nucleus is formed in a highly excited state. In this highly excited state, the system reaches statistical equilibrium. A key feature of a compound nucleus is that it does not "recall" how it was formed; its decay is independent of its formation method.

We can use this property to create a specific compound nucleus of interest via different reaction channels. The reaction we aim to constrain in this work is neutron capture followed by γ-ray emission denoted as $^{A}\mathrm{X}(\mathrm{n},\gamma)^{A+1}\mathrm{X}$. For this work, we utilize β^- decay, where our compound nucleus of interest $\left(^{A+1}\mathrm{X}\right)$ is the child nucleus in the β decay chain. This is a practical method for producing and studying short-lived radioactive nuclei of interest.

When nuclear reactions populate levels above the known discrete levels in the compound nucleus, the statistical properties of the nucleus become important. The statistical properties relevant to this work are the nuclear level density (NLD) and the γ-ray Strength Function (γSF). The nuclear level density is the number of levels in the nucleus per energy interval, while the γ-strength function is a measure of how probable a γ-decay is as a function of E_γ. For nuclear reactions, the Optical Model Potential is used to describe the potential for the interaction(s).

2.6.1 Nuclear Level Density (NLD)

When examining a nucleus and its energy levels, one can measure discrete energy levels and transitions among them. However, as the excitation energy increases, the spacing between these discrete levels decreases. Eventually, these levels are too close to distinguish, where the distance between the levels is on the same order of magnitude as the level width (Γ). The region above the discrete levels is called the quasi-continuum. After entering the quasi-continuum region, as excitation energy increases further, the energy levels begin to overlap, as each level has a certain width. This is known as the continuum region.

The nuclear level density (NLD) is a measure of how many energy levels exist per energy interval. This concept is typically used to describe the NLD above the discrete region, specifically in the quasi-continuum and above.

If parity is ignored, the NLD $\rho(E, J)$ can be decomposed into two parts:

$$\rho(E, J) = f(J)\rho(E), \tag{2.8}$$

where $f(J)$ is the spin distribution and the NLD $\rho(E)$ is independent of the spin. This decomposition is important for the subsequent analysis, as this thesis explicitly takes the spin distribution into account.

The spin distribution is a function that describes the expected distribution of spins, and usually relies on something called the spin cut-off (σ) parameter. There are several different ways to model the spin distribution, one such is described in Section 2.6.1.1.

An example of NLD extracted using the Oslo method (described in Chapter 6) is shown in Figure 2.3 for ^{164}Dy [6] (filled black squares), together with discrete levels as a black histogram. The NLD at the neutron separation energy, $\rho\,(S_n)$, is indicated by an open black square. At lower energies, the NLD follows the discrete levels; this is expected, as the NLD is typically normalized to both discrete levels and $\rho\,(S_n)$. Above the discrete levels, NLD increases exponentially with the excitation energy.

When extracting level densities with the β-Oslo method, as discussed in Chapter 6, it is an absolute partial level density. This is due to the specific spin population of the compound nucleus.

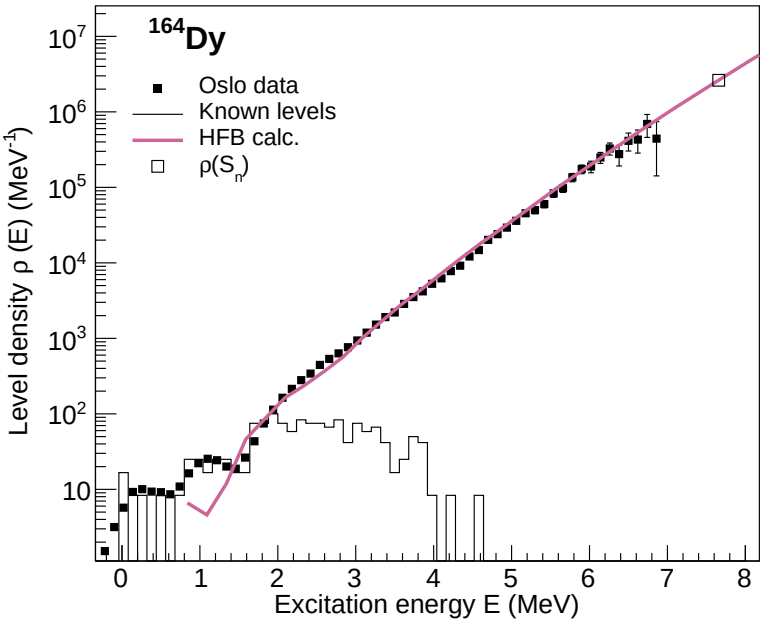

Figure 2.3 The extracted NLD of ^{164}Dy (filled black squares), together with discrete levels (black line). The level density at the neutron separation energy is shown (open square) together with the adjusted Hartree-Fock-Bogoliubov model (red line). Figure taken from Ref. [6].

When populating the compound nucleus through β decay, we assume only allowed transitions occur. This restricts the spin change from the parent nucleus by $\Delta J = 0, \pm 1$ with no change in parity ($\Delta\pi = 0$). If an isomer with a different J^π exists in the parent nucleus, it may be possible to populate a broader range of spins in the child nucleus. As we include the dipole γ-ray transmission from the first γ in the cascade, another $L \pm 1$ is added along with both parities.

2.6.1.1 Spin cut-off parameter

One of the model-dependent variables used in the Oslo method is the spin cut-off parameter. There are several different models that can be used for this, which in turn means this leads to systematic uncertainties when it is used. In the present work, the Fermi gas spin distribution was used. The Fermi gas spin distribution, $R_F(E_x, J)$ is defined as

$$R_F(E_x, J) = \frac{2J+1}{2\sigma^2} \exp\left(\frac{-(J+1/2)^2}{2\sigma^2}\right), \tag{2.9}$$

where J is the spin, σ^2 is the spin cut-off parameter defined as:

$$\sigma^2 = \left(0.83A^{0.26}\right)^2, \tag{2.10}$$

where A is the mass number.

2.6.1.2 Level density models

To model nuclear level densities, we can use frameworks derived from statistical physics. These include, but are not limited to, the Constant Temperature model, the Back-Shifted Fermi Gas model, and semi-microscopic models, as detailed below. The theoretical models are crucial for nuclear astrophysics as stellar nucleosynthesis simulations rely on them when experimental data is unavailable.

Constant Temperature Model

The Constant Temperature (CT) model [7], [8] is frequently used to describe experimental data, as seen in Ref. [9], [10] and references therein, especially when extrapolating to energies below 10 MeV; it has shown significant overlap with level densities measured in that range. This model assumes that the nucleus remains at a thermal equilibrium, as the added excitation energy is primarily used to break nucleon pairs rather than increase the temperature. The NLD is defined as:

$$\rho\left(E\right) = \frac{1}{T} e^{(E_x - E_0)/T}, \tag{2.11}$$

with ρ being the level density as a function of energy, while the effective temperature T and energy shift E_0 are free parameters in the CT model. This model assumes equiparity (an equal distribution of parities).

Back-Shifted Fermi Gas

Another common model used for describing level densities or for extrapolation to $\rho(S_n)$ is the Back-Shifted Fermi Gas (BSFG) model. The standard Fermi gas model treats neutrons and protons as non-interacting fermions within a potential well. However, as the basic model fails to account for pairing effects, it was later corrected by an energy shift, resulting in the BSFG model:

$$\rho(E) = \frac{e^{\sqrt{a(E-E_1)}}}{12\sqrt{2}\,\sigma^{1/4}\,(E - E_1)^{5/4}}, \tag{2.12}$$

where a is the level density parameter, E_1 the energy shift, and σ is the spin cut-off parameter. A similar formulation often used is:

$$\rho\left(E_x\right) = \frac{1}{\sqrt{2\pi}} \frac{\sqrt{\pi}}{12} \frac{\exp\left(2\sqrt{aU}\right)}{a^{1/4}U^{5/4}}, \tag{2.13}$$

where $U = E_x - \Delta$. Here, Δ is an empirical parameter describing the odd-even effects in the nuclei [11], and a is the level density parameter related to the spacing of the single-particle states near the Fermi surface.

Semi-Microscopic models

TALYS, a Hauser-Feshbach code, includes several theoretical models described in detail in Ref. [11]. Some of these microscopic models are better at reproducing nuclear level densities on a large scale and can be adjusted to experimental data. For example, "Model 5" in TALYS utilizes the Hartree-Fock-Bogoliubov (HFB) plus combinatorial approach [12]. This model includes a phenomenological damping function to describe the transition from spherical to deformed nuclei. In TALYS, these level densities are provided in a tabular format up to 200 MeV and for spins up to $J = 49$ [11]. An example of this HFB model, adjusted to experimental NLD data for ^{164}Dy, is presented in Figure 2.3 (red line); it shows good agreement with the experimental data and intersects with $\rho\left(S_n\right)$.

2.6.2 γ-ray Strength Function (γSF)

The γ-ray Strength Function (γSF) is a measure of the nuclear γ-decay probability as a function of the emitted γ-ray energy, E_γ. In this work, we extract the γSF for magnetic and electric dipole transitions, denoted as $f_{M1}(E_\gamma)$ and $f_{E1}(E_\gamma)$. At higher excitation energies, the γSF is dominated by the Giant Dipole Resonance (GDR), while other resonances can contribute significantly at lower energies. These resonances appear as "bumps" in the γSF spectrum. Common examples include pygmy or scissors resonances. At low energies, a phenomenon known as the "upbend" or Low-Energy Enhancement (LEE) may occur. These resonances are detailed further in Section 2.6.2.1.

For γ radiation, the probability of emitting a photon with multipolarity L and energy E_γ is described by the transmission coefficient $\mathcal{T}$. As the angular momentum increases, the transmission coefficient decreases. Conversely, the transmission coefficient generally increases with E_γ. The relationship between the γ-ray strength function, $\left(f_{XL}\left(E_\gamma\right)\right)$ and the transmission coefficient ($\mathcal{T}_{XL}$)

is defined as [13]:

$$\mathcal{T}_{XL}(E_\gamma) = 2\pi E_\gamma^{2L+1} f_{XL}(E_\gamma), \tag{2.14}$$

where E_γ is the energy of the emitted γ ray, X denotes an electric (E) or magnetic (M) transition, and L the angular momentum of the transition. This connection encompasses the macroscopic probability of photon emission or absorption with the microscopic properties of the nucleus.

2.6.2.1 Resonances

Several resonances in the nucleus can be investigated through the γSF. Depending on the nuclear properties, these resonances can shift, appear, or disappear. This evolution is visible in Figure 2.4, which shows various resonances in Nd isotopes, including the low-energy enhancement, the Scissors mode, and the Pygmy dipole resonance(s).

Giant dipole resonance (GDR)

The Giant Dipole Resonance is the dominant resonance appearing in all nuclei, typically between 10-15 MeV, and is $E1$ in nature. The GDR can be interpreted as a collective oscillation in which the nucleons resonate against each other.

Mathematically, this can be described by Lorentzian functions such as the Generalized Lorentzian (GLO) [13] or the Simple Modified Lorentzian model (SMLO) where E_{SMLO} is the GDR centroid, σ_{SMLO} is the resonance strength, and $\Gamma\left(E_\gamma, T\right)$ is defined as:

$$\Gamma\left(E_\gamma, T\right) = \frac{\Gamma_{\mathrm{SMLO}}}{E_{\mathrm{SMLO}}}\left(E_\gamma + \frac{(2\pi T)^2}{E_{\mathrm{GDR}}}\right), \tag{2.15}$$

where Γ_{SMLO} is the width, and T the temperature of the nucleus.

Recent descriptions of the GDR by Quasi-Random Particle Approximation (QRPA) calculations

....

Pygmy dipole resonance

The pygmy dipole resonance (PDR) has been theorized as an oscillation of the neutron skin against a neutron-proton core (N=Z=60) [14]. In the Nd-isotopic chain, it is believed to be prevalent in lighter isotopes, but it disappears as the nuclei become more deformed. Consequently,

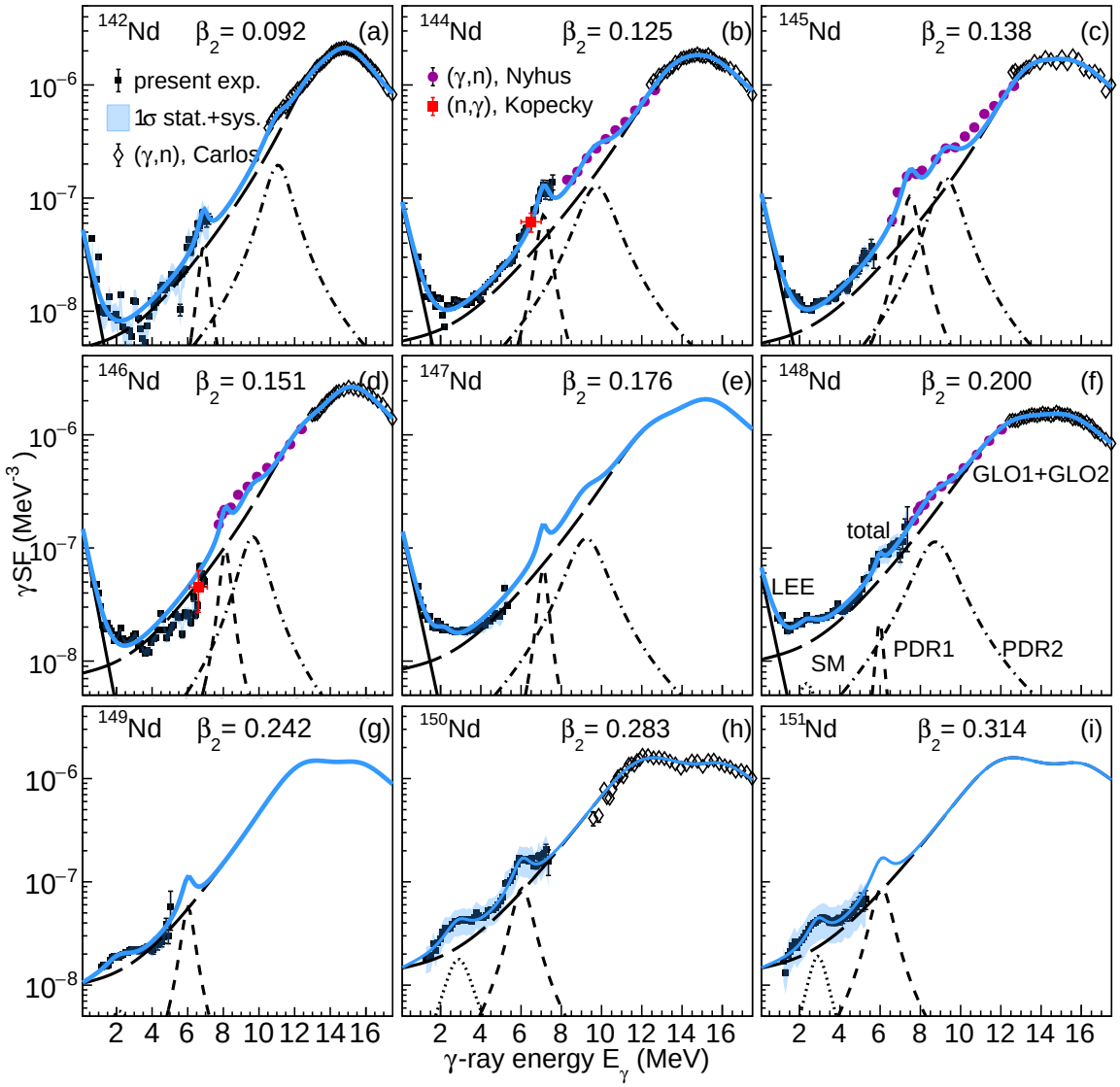

Figure 2.4 Results from Ref. [14] showing the evolution of the low-energy enhancement, the Pygmy resonance, and the Scissors resonance in the Nd-isotope chain. The Giant Dipole Resonance is represented by the long dashed line, the scissors resonance by the dotted line, the pygmy resonance components by dashed and dash-dotted lines, and the low-energy enhancement by the solid line.

the strength of the Pygmy resonance decreases with increasing deformation (β_2). These PDRs are shown as dashed or dash-dotted lines in Figure 2.4.

The Pygmy resonance contribution, $f_{\text{Pygmy}}(E_\gamma)$, can be described with the Standard Lorentzian model (SLO) [11], [15]:

$$f_{\text{Pygmy}}\left(E_\gamma\right) = \frac{1}{3\pi^2\hbar^2c^2}\frac{\sigma_{\text{P}}E_\gamma\Gamma_P^2}{\left(E_\gamma^2 - E_{\text{P}}^2\right)^2 + E_\gamma^2\Gamma_{\text{P}}^2}, \tag{2.16}$$

where E_{P} is the energy of the resonance, Γ_{P} is the width of the Pygmy resonance, and σ_{P} is the magnitude of the resonance.

Scissors resonance

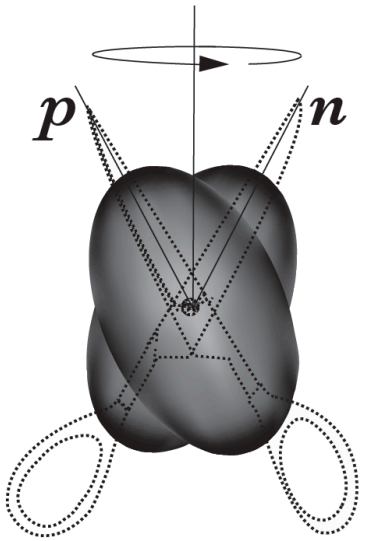

Figure 2.5 Illustration of the resonance of protons and neutrons for the scissors resonance. Figure from [16].

The scissors resonance is named for the collective, "scissors-like" motion of the proton and neutron distributions. This was first theorized in [17] and experimentally confirmed in [18]. An illustration of this motion and the resulting magnetic moment is shown in Figure 2.5.

For the Nd isotopic chain, Guttormsen *et al.* [14] demonstrated a strong presence of the scissors mode as the neutron number increases, as indicated by the black dotted line in Figure 2.4. The data suggest that the Scissors Mode (SM) emerges as the nuclei become more deformed with increasing neutron number, and was modeled with an SLO.

Low Energy Enhancement (LEE)

The "upbend" or low-energy enhancement (LEE) was first measured in ^{57}Fe [19], and has later been observed for several nuclei, as detailed in [20] and references therein. Understanding how the magnitude of the LEE evolves is a key part of characterizing nuclear statistical properties. Currently, there is no conclusive experimental evidence determining whether the LEE is electric or magnetic in nature, although it has been confirmed to be of dipole character [21]. Theoretical models suggest a magnetic nature, but this remains to be verified experimentally.

Generally, the LEE component, f_{LEE}, can be described by an exponential function:

$$f_{\mathrm{LEE}}\left(E_\gamma\right) = C \cdot \exp\left(-\eta E_\gamma\right), \tag{2.17}$$

where C and η are fit parameters, which have no physical meaning in themselves. This parameterization is shown as the solid black line in Figure 2.4.

For the Nd isotopic chain, as the deformation increases, the magnitude of the LEE decreases, as can be seen in Figure 2.4.

2.7 Optical model potential

To describe the potential for nuclear reactions, the Optical Model Potential (OMP) utilizes a complex potential to characterize the interactions between a projectile and a target nucleus. This approach is analogous to classical optics, where a light wave travels through a medium with a complex refractive index. This potential consists of a real part representing the refraction, which deals with the nuclear attraction that governs elastic scattering. The imaginary part represents absorption, which deals with inelastic scattering and capture processes. In the energy regions relevant to nuclear astrophysics, the imaginary potential is often further divided into volume and surface components [11] to account for the fact that low-energy nucleons are primarily absorbed at the nuclear surface. Furthermore, a spin-orbit term is included [11].

For the purpose of this thesis, the local and global phenomenological OMP from Koning and Delaroche [22] was used, which is the default OMP in TALYS. Because this OMP assumes near-spherical nuclides, it might be pertinent to investigate the effect of choosing other OMPs.

CHAPTER 3

NUCLEOSYNTHESIS

With the relevant nuclear properties established, this chapter will look into nucleosynthesis processes and places the research of this thesis into a broader context. First, the processes responsible for producing lighter nuclei are explained in Section 3.2, followed by those for elements heavier than iron in Section 3.3. Subsequently, neutron-capture processes are detailed in Section 3.4, concluding with the impact of nuclear uncertainties on astrophysical simulations in Section 3.5.

3.1 Nuclear astrophysics

In nuclear astrophysics, we rely on observations and modeling to understand nucleosynthesis. From a nuclear physics perspective, we measure important nuclear properties so that we can reduce the impact of nuclear uncertainties in these models. Not all nuclear properties are equally impactful; different nucleosynthesis sites and processes involve different nuclei. To determine which measurements are most crucial, nuclear scientists often rely on sensitivity studies to prioritize research that will most effectively advance the field.

3.2 Light elements

The origin of all light elements is hydrogen. By examining processes such as those occurring in our Sun, we can identify production pathways for heavier elements up to iron. In solar-mass stars, the dominant fusion process is the proton-proton chain, a series of reactions that converts four hydrogen atoms into a ^{4}He nucleus. In stars more massive than the Sun, the CNO cycle is the primary mechanism for hydrogen fusion. In this cycle, carbon, nitrogen, and oxygen act as catalysts to fuse four protons into ^{4}He.

When a star's hydrogen supply dwindles, the lack of outward radiation pressure causes the core to contract and heat up. Once temperatures are sufficiently high, hydrogen ignites in a shell around the core, leading to helium fusion. Simultaneously, the star's outer layers expand and cool. Following helium burning, successive stages of core burning occur: carbon, neon, oxygen, and finally silicon burning, which lead to the end-stage fusion product, ^{56}Fe, depending on the stellar mass.

Up to the mass of iron, heavier elements can be created via stellar fusion. Fusion limits at iron because the binding energy per nucleon reaches its peak at this point and decreases for heavier masses. Consequently, it is no longer energetically favorable to form elements through the fusion of lighter elements, as the process becomes endothermic.

3.3 Beyond Iron

Elements heavier than iron are produced via mechanisms other than fusion, as fusion is no longer energetically favorable. This is illustrated by the binding energy per nucleon ratio (BE/A) shown in Figure 2.2.

Once iron is created, various capture mechanisms drive the nucleosynthesis of heavy elements. Two well-known neutron-capture processes were first discussed in the seminal B2FH paper [1]: the s (slow) and r (rapid) processes. Since then, other processes have been suggested, such as the i (intermediate) and n (neutron) processes. On the proton-rich side, processes such as the γ process also play a role, though this is beyond the scope of this thesis [23].

3.4 Neutron-capture processes

For nucleosynthesis, many of the descriptions and theories stem from [1], though more sites and processes have been introduced and theorized since then. From [1], two main neutron-capture processes were introduced, the s and the r process, where the pathways of these processes are illustrated in Figure 3.1. These are described more in Sections 3.4.1 and 3.4.2 respectively. Later, another process was introduced [24]: the i (intermediate) process, which is discussed in Section 3.4.3.

3.4.1 The slow neutron-capture process

The slow neutron-capture process is a nucleosynthesis process that happens by neutron capture on a stable isotope, followed either by another neutron capture or by β decay towards stability. In the s process, the mean half-life of the β decay is smaller than the mean neutron-capture time $\left(t_{cap} \gg t_{\beta}\right)$. The s process happens over long time periods, with relatively low temperatures and neutron densities and along the valley of stability. The start of the s process pathway from ^{56}Fe is illustrated in Figure 3.1. The primary sites for the s process are low-mass stars in the Asymptotic

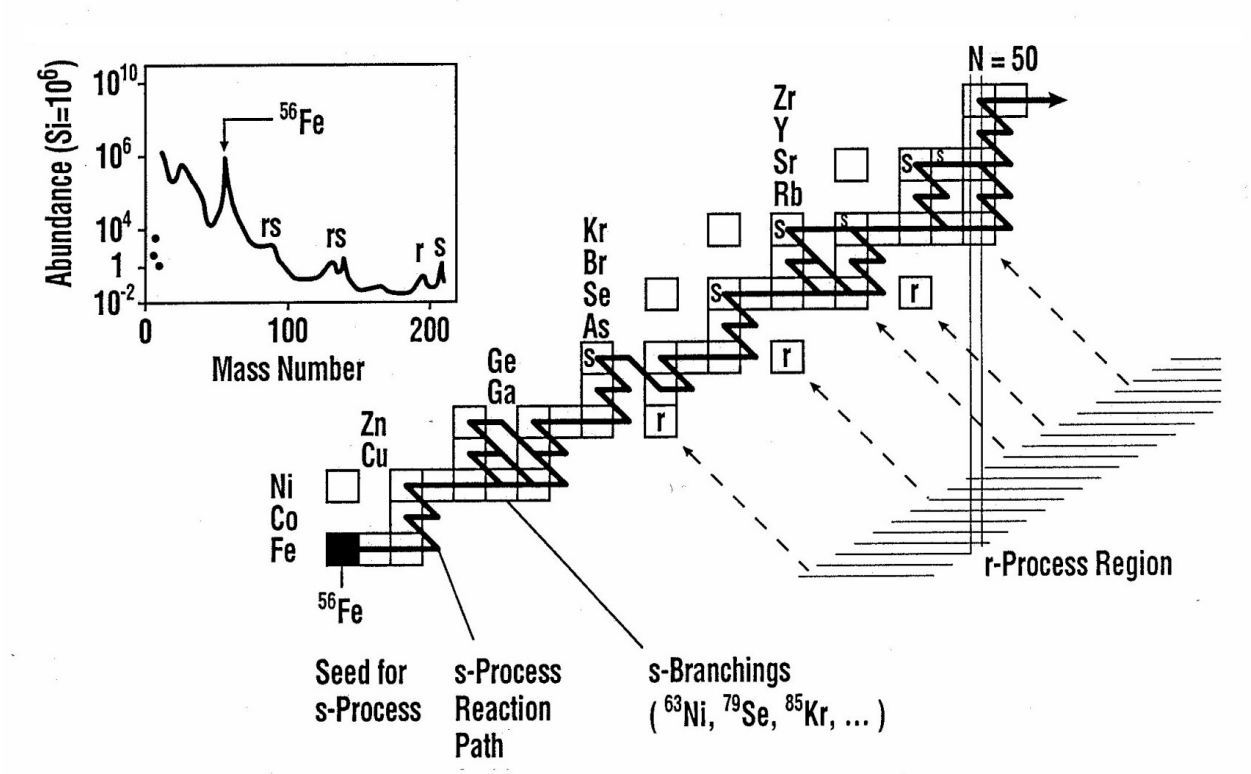

Figure 3.1 Illustration of the start of the s-process path from ^{56}Fe, along with the contribution from the r process marked in the boxes with r, and the abundance distribution. Figure from [25].

Giant Branch (AGB) phase, though production also occurs in massive stars during helium or carbon shell burning.

3.4.2 The rapid neutron-capture process

The r process is a fast, hot, and neutron-dense process $\left(\sim 10^{20}\text{cm}^{-3}\right)$ responsible for producing approximately half of the heavy elements. Nucleosynthesis occurs via a rapid chain of neutron captures toward the neutron drip line. This continues until a "waiting point" is reached: typically at a magic number, where further capture is inhibited by photodisintegration. Once the neutron flux dissipates, these neutron-rich isotopes β-decay toward stability. In this process, β-decay half-lives are much longer than the mean neutron-capture time $\left(t_\beta \gg t_{cap}\right)$. The r process was first confirmed observationally in the GW170817 neutron star merger event [26], where characteristic r-process elements light curves were detected in the accompanying kilonova.

The abundance elements produced in the s-process nucleosynthesis is illustrated in the upper

left-hand corner of Figure 3.1, showing that some of them are shielded by stable elements, which is different from the elements that are produced in the r-process nucleosynthesis.

3.4.3 The intermediate neutron-capture process

The i-process nucleosynthesis happens via a series of neutron captures a few steps away from stability, followed by combinations of β decay and neutron capture. In the i process, β-decay half-lives are comparable to the mean neutron-capture times $\left(t_\beta \approx t_{cap}\right)$, making the pathway highly dependent on the specific stellar environment. Generally in this region, we have some nuclear data available, such as half-lives, discrete states, binding energy, and Q_β–values. However, these nuclei have unknown neutron–capture cross sections, which contributes to uncertainty in the possible reaction pathways.

When looking at the abundance ratios compared to what we expect from the s- and r-process nucleosynthesis, there are discrepancies in what can be predicted and what we observe [27]–[29], as is seen in Figure 3.2. Based on this discrepancy, another nucleosynthesis process is needed with neutron densities in-between that of the s and r process. In the 1970s, the i process was suggested as another form of neutron–capture nucleosynthesis [24], and has been prevalent in literature based on newer astrophysical evidence [29]–[35].

For the i process to occur, convective mixing of hydrogen into a helium-burning zone is required, a phenomenon known as a proton ingestion event (PIE). The fluctuations in the helium-burning shell lead to instability and there will be regular thermal flashes that trigger convection. The start of the proton ingestion event is when the preceding thermal pulse (TP) leads to protons created from the $^{12}\mathrm{C}\,(p,\gamma)^{13}\,\mathrm{N}$, and $^{13}\mathrm{N}\,(\beta^{+})^{13}\,\mathrm{C}$ reactions before the dredge up into the convective envelope [34].

Potential sites for the i process are post-Asymptotic Giant Branch (AGB) stars, very late thermal pulses of post-AGB stars, low-metallicity metal-poor stars, and Rapidly Accreting White Dwarfs (RAWD) [29], [33]. Since the i process cannot be observed directly, any evidence of it happening must be based on abundance distributions of heavy elements. One such place that fits this observed abundance of heavy elements is carbon enhanced metal-poor (CEMP) stars. These old CEMP

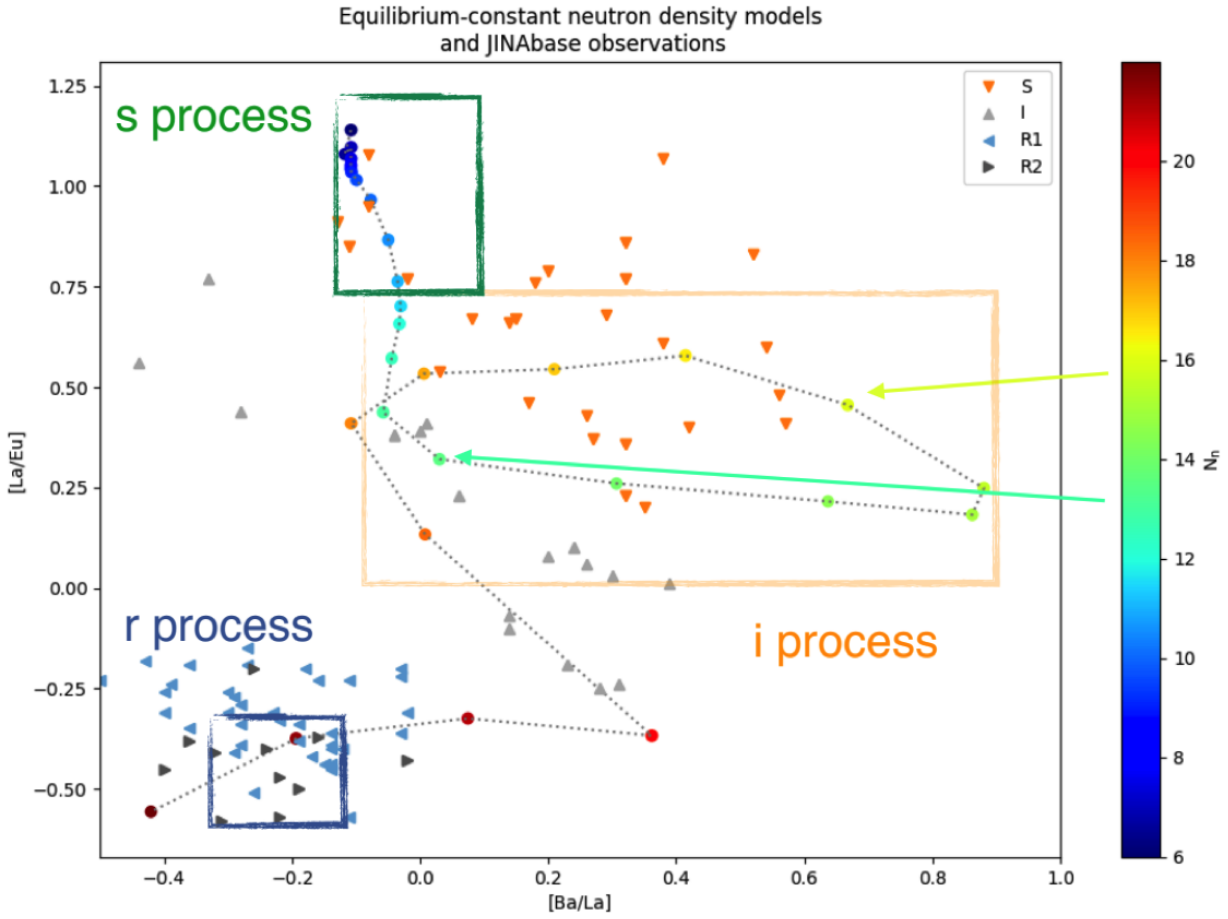

Figure 3.2 Stellar abundance ratios of [La/Eu] vs [Ba/La]. The different types of triangles represent various types of low-metallicity stars. Carbon-enhanced metal-poor stars with a high enhancement of heavy elements are marked as S and I. The observed abundances are from the JINAbase compilation [36]. The dashed line represents abundance ratios from simulations where the neutron density, N_n, has been varied $\left(10^9 - 10^{20} \text{n/cm}^3\right)$. The regions of abundances expected from the s and r process are marked with green and blue boxes respectively, while i process is marked in the orange box. Figure from [37].

stars are believed to be enriched by a single astrophysical process, and carry signatures of single nucleosynthesis processes. For reference, a model calculation that only varies neutron density is shown in Figure 3.2, and this has a significant impact on both the Ba/La and the La/Eu ratio. For these carbon-enhanced metal-poor stars shown in Figure 3.2, this enhancement of heavy elements is typically more than two orders of magnitude higher than the solar abundance of Fe [37].

3.5 Impact of neutron-capture reactions on the i process

Uncertainties in nuclear properties limit the inferences we can draw from stellar observations, and a goal in nuclear astrophysics is to investigate key reactions to better understand stellar nucleosynthesis. This thesis aims to shed light on potential i-process sites by constraining specific neutron capture cross-sections. With all of these nuclear properties in mind, there are certain

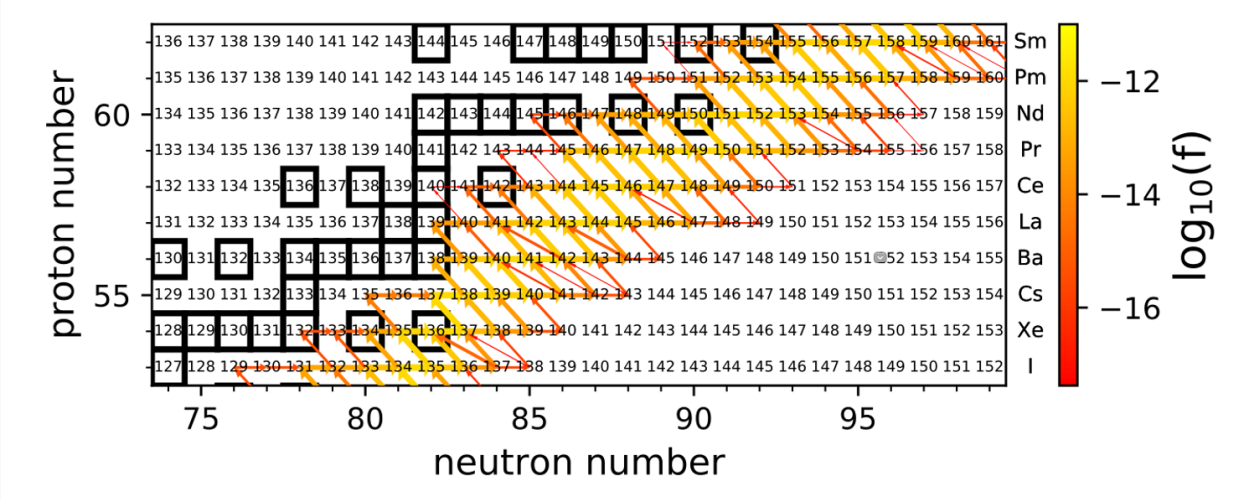

Figure 3.3 Possible reaction pathways for the i process. The absolute pathway is not distinguishable due to uncertainties in reactions. Not all of the possible reactions in the neodymium chain that can create samarium and europium are included in the depiction. Figure from Ref. [32].

nuclei that are more important to understand if we want to accurately predict abundances of heavy elements. In sensitivity studies, these properties can be varied within the uncertainty, which can then indicate which properties are more crucial to constrain. In Denissenkov *et al.* [32], a sensitivity study was carried out on a possible site of i-process nucleosynthesis. In that study, a 1D model of a rapidly accreting white dwarf (RAWD) at a neutron density of $N_n = 3.6 \cdot 10^{14}$ n/cm^3 was used to map potential reaction pathways (Figure 3.3). In Figure 3.3, the neutron fluxes shown

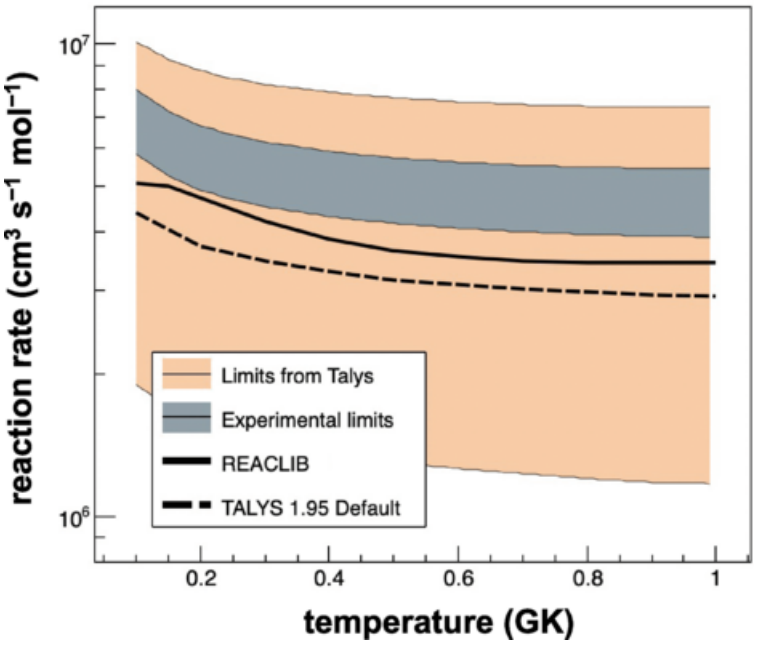

Figure 3.4 The reaction rate of the neutron capture on ^{139}Ba compared to REACLIB [39] in solid black, and the error band from the model uncertainty of TALYS in orange, with the default in the dashed line. Comparatively, Spyrou *et al.* [38] show that their experimental results constrain the reaction rate to about a factor of two. Figure taken from Ref. [38].

superimposed on the chart of nuclei and stable nuclei are marked with black boxes. One such case was understanding the neutron capture reaction rate on ^{139}Ba, which was constrained, Figure 3.4, and the impact on the [La/Eu] to [Ba/La] ratios for i process with this applied in Figure 3.5 [38]. The constrained reaction affects the predicted La abundance.

In Figure 3.4, it can be seen that the resulting constrained reaction rate in gray is higher than the default rate predicted by TALYS 1.95 and the REACLIB predicted rate [39]. TALYS [40], [41] is an open-source software for simulating nuclear reactions, while REACLIB [39] is a database of nuclear reaction rates for astrophysical simulations. From indirect techniques such as the β-Oslo method, this type of constraint to an order of two is typical, but the degree to which theoretical predictions match varies.

From the top part of Figure 3.5, the resulting ratio of [Ba/La] and [La/Eu] within the nuclear uncertainties covers a large range of ratios in the contour plot, assuming a single i-process model with a neutron density of $N_n = 3.16 \times 10^{13}$n cm^{-3} as detailed in [32]. Applying this constrained neutron-capture reaction rate on ^{139}Ba to potential i-process pathways in network calculations,

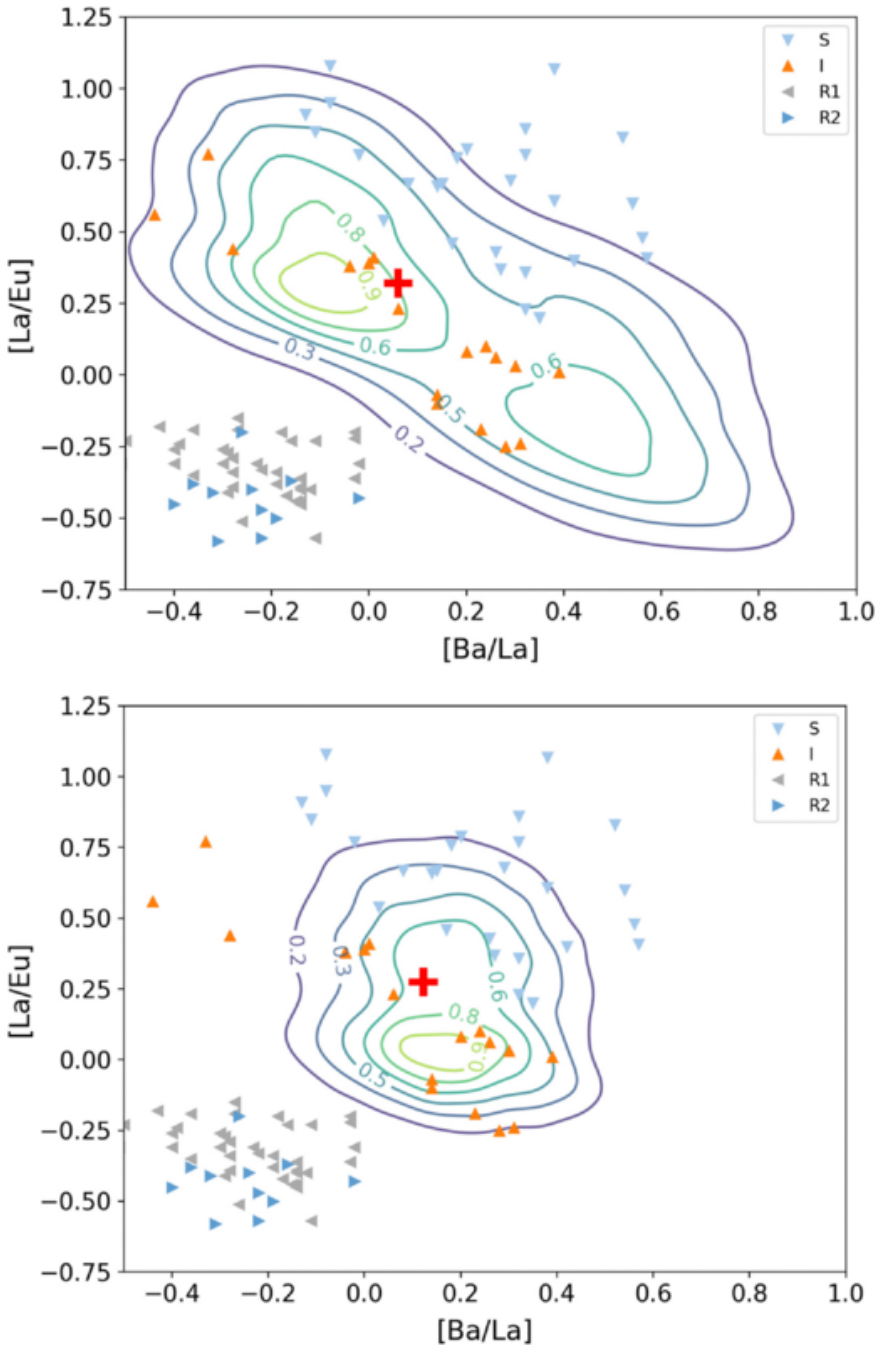

Figure 3.5 Constraining uncertainties in key neutron capture cross-sections can provide insights to potential i-process sites. Top figure shows possible combinations of [La/Eu] to [Ba/La] ratios for i process, with a wide spread due to nuclear uncertainties in the ^{139}Ba(n,γ)^{140}Ba, with the constrained cross-section showing the effect in the bottom plot. Figure taken from Ref. [38].

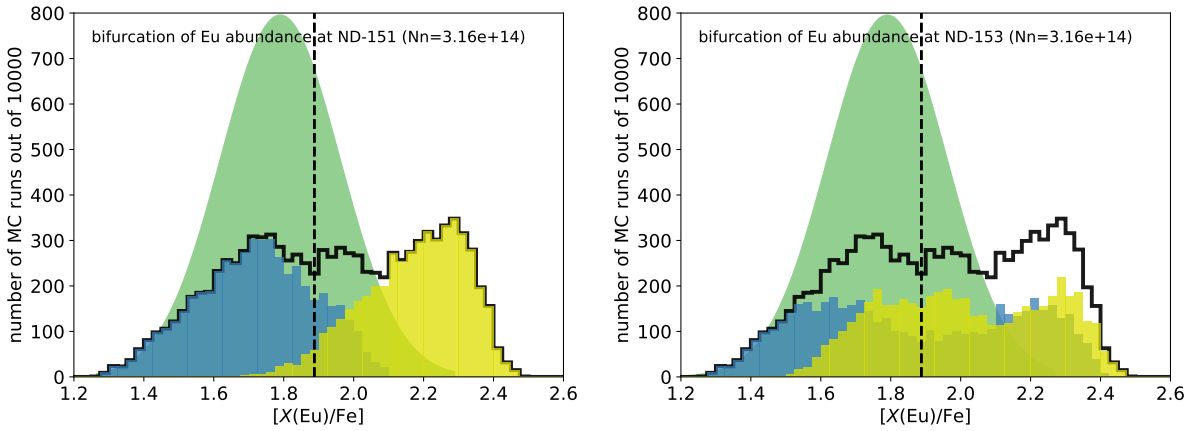

Figure 3.6 In the sensitivity study by Denissenkov *et al.* [32], the nuclear uncertainties from neutron capture in the production of Ba to W was investigated. Based on this, there was bifurcation in the final abundance of Eu that had a large negative correlation to the uncertainty of the neutron capture on ^{151}Nd (left) and a smaller negative correlation with the neutron capture on ^{153}Nd (right). The blue and yellow distributions correspond to rate multiplication factors of less than 1 or more than 1 respectively. The full distribution from the MC simulations is in the solid black line, with the benchmark model shown as a vertical line. The green Gaussian curve is reported data (star CS 31062-050) [42]. Figures from [43].

severely constrains the possible [Ba/La] ratios as seen in the bottom part of Figure 3.5. With this, it is possible to examine the observations of stars to investigate where the simulations match observed abundances.

While the previous work constrained the La abundance, the production of Eu remains largely unconstrained. This is the focus of the present thesis. In the same sensitivity study, there was a strong negative correlation of the neutron-capture rates on ^{151,153}Nd for the final abundances of Eu. Based on these calculations, the upper and lower end of the uncertainty in the neutron captures on ^{151,153}Nd leads to a significant bifurcation in the Eu abundance, see the left side of Figure 3.6. This bifurcation means that the predicted production rate of Eu is split into two distributions due to the nuclear uncertainty. On a similar note, we also need to constrain the neutron capture cross-section on ^{153}Nd as it may also affect the final abundance of Eu, see the right side of Figure 3.6. Here, the distributions largely overlap with no clear bifurcation, but instead have a large spread.

CHAPTER 4

EXPERIMENTAL SETUP

The experiment was performed at the Argonne Tandem Linac Accelerator System (ATLAS) facility at Argonne National Laboratory during September 2022 using the Californium Rare Isotope Breeder Upgrade (CARIBU) facility [44]. The facility used in the experiment is described in detail in Section 4.1. For the experiment, the events were measured using the Summing NaI(Tl) (SuN) scintillator, which is described in Section 4.2. This was done with the radioactive beam implanting into the tape system for activated nuclei (SuNTAN), which is described in Section 4.3. The particle-γ coincidences were measured with a plastic scintillator, SuNSPOT, detailed in Section 4.4. Data acquisition was done using the Digital Data Acquisition System (DDAS). DDAS was used for online analysis and for recording data during the experiment using the XIA Pixie-16 Digitizers [45].

4.1 Facility

CARIBU provided fission fragments from ^{252}Ca, which spontaneously fissions. An overview of the facility shown in Figure 4.1. The fission fragments were extracted and separated with a mass separator, which resulted in isobar contamination. The addition of Multi-Reflection Time-of-Flight Spectrometer (MR-ToF), made it possible to isolate a specific isotope from the isobars. For optimal statistics, the experiment was run without MR-ToF. Without the use of the MR-ToF, there was contamination present in the beam, as other isobars were also implanted in the tape and decayed along with the isotopes of interest. This problem was more prevalent in the 154 isobars, as the abundance of the isotope of interest, ^{154}Pr, was of lower intensity than other isotopes in the beam. The are dictated by the fission fragment yields from ^{252}Ca, which is available in Ref. [46]. For the isobar setting used, the relative yields are presented in Tables 5.1 and 5.2. The subtraction of isobar contamination is described in Chapter 5.

4.2 The Summing NaI(Tl) (SuN) detector

For the experiment, we used the Summing NaI(Tl) (SuN) scintillator detector as our γ-ray detector. SuN is a 16 in. $\times$ 16 in. barrel shaped detector with a 1.8 in. diameter borehole through

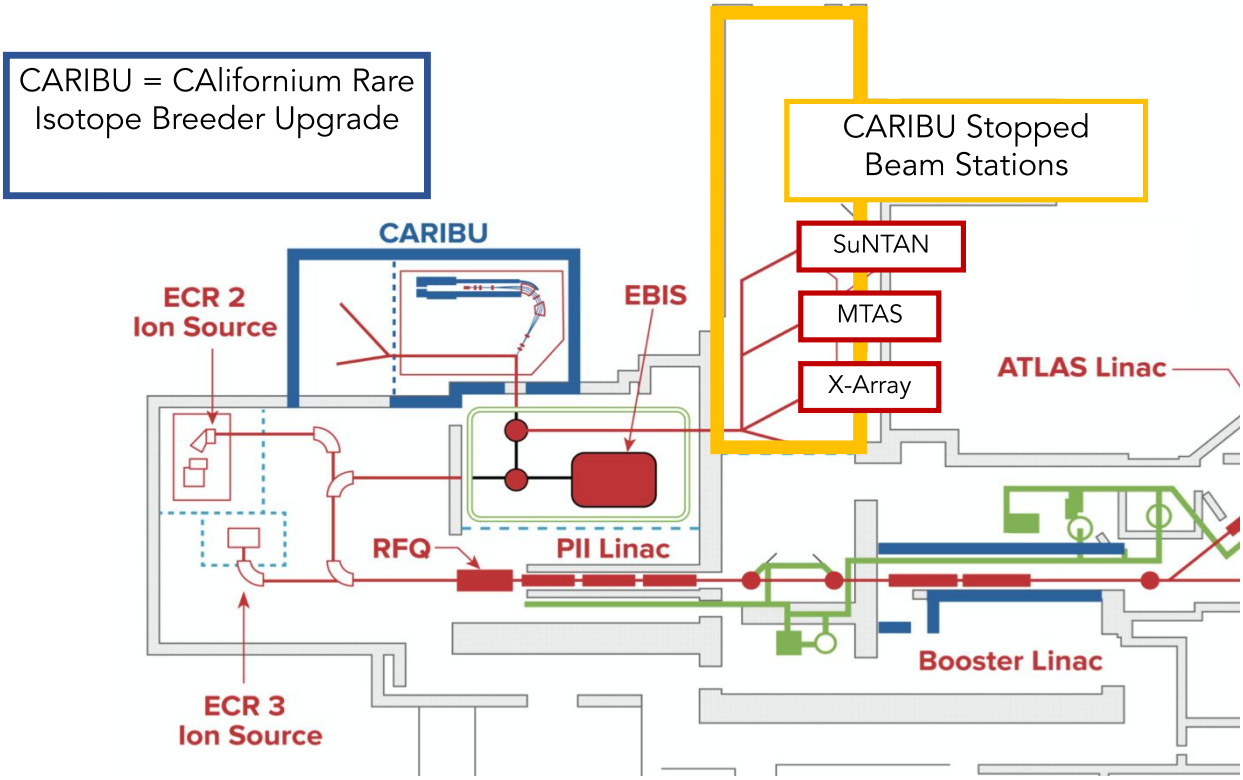

Figure 4.1 Overview of the CARIBU beam line at the ATLAS Facility at Argonne National Laboratory, adapted from Ref. [47].

the beam axis, divided into eight segments made of thallium doped NaI [48]. There are four segments at the bottom, and four at the top, as shown in Figure 4.2. Each segment is optically isolated by 0.5 mm aluminum plates, which are all covered with a 0.25 mm thick reflecting material [48]. Each segment has three high voltage photo-multiplier tubes (PMTs). SuN is a large volume, high-efficiency detector, which makes it possible to conduct something called total absorption spectroscopy (TAS), and has an angular coverage of nearly 4π. At 662 keV, SuN has an average resolution of 6.1(2) %, while at 1173 keV and 1332 keV it has an average resolution of 5.8(2)% [48]. By summing up all the segment energies event-by-event, we extract the total excitation energy of the nucleus. For the aforementioned set of peaks, the summing efficiencies are 85(2)% for and 65(2)% with multiplicity 1 and 2 respectively [48].

4.3 SuNTAN - Tape station for Activated Nuclei

Connected to the setup, is the Tape station for Activated Nuclei (SuNTAN) [49], which is shown in Figure 4.3. This tape was guided by a connected motor, which circulates it into the center of the

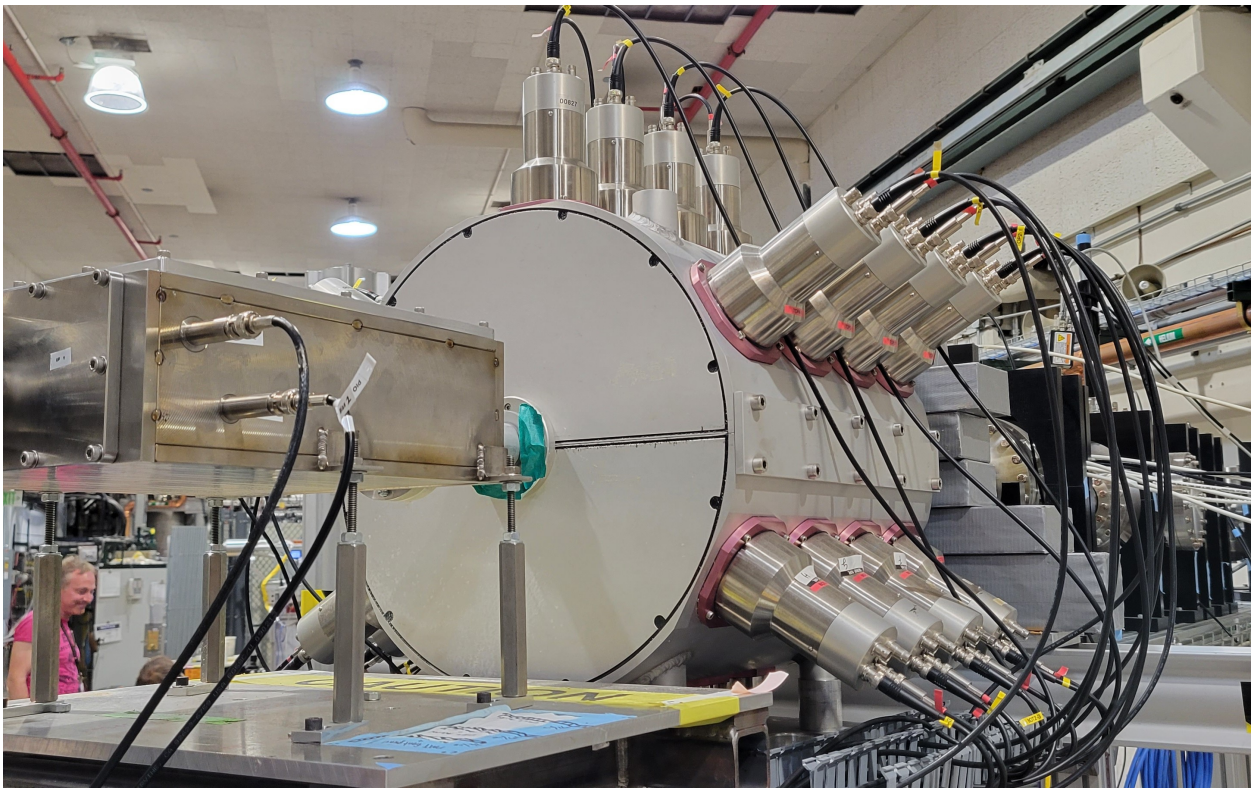

Figure 4.2 Picture of the Summing NaI(Tl) detector, taken during the experiment in September 2022. The detector can be seen having 12 PMTs on each semi-cylinder, with a borehole going throughout the symmetry axis.

SuN detector, for the implantation of the low-energy beam. The tape was connected to a motor, which was able to move the tape step wise. Which was used to move any previously implanted and/or contaminated tape out of the middle of the SuN detector and into the tape storage. The tape storage and tape are also under vacuum. SuN was physically shielded from the tape storage with lead bricks, to reduce any γ induced background. The tape was sufficiently long to stay uncontaminated by the time it made a full rotation for this experiment, as the experiment did not run for long enough for a full revolution of the tape.

4.4 SuNSPOT

The fiber detector is an eight-sided plastic scintillator that was placed in the center of the SuN beamline. Due to space constraints, the light from the fiber detector was collected by 32 alternating wave-shifting optical fibers. On the exterior, the plastic scintillator and the optical fibers were painted with reflective paint, to enhance the efficiency of the detector, by minimizing the amount of

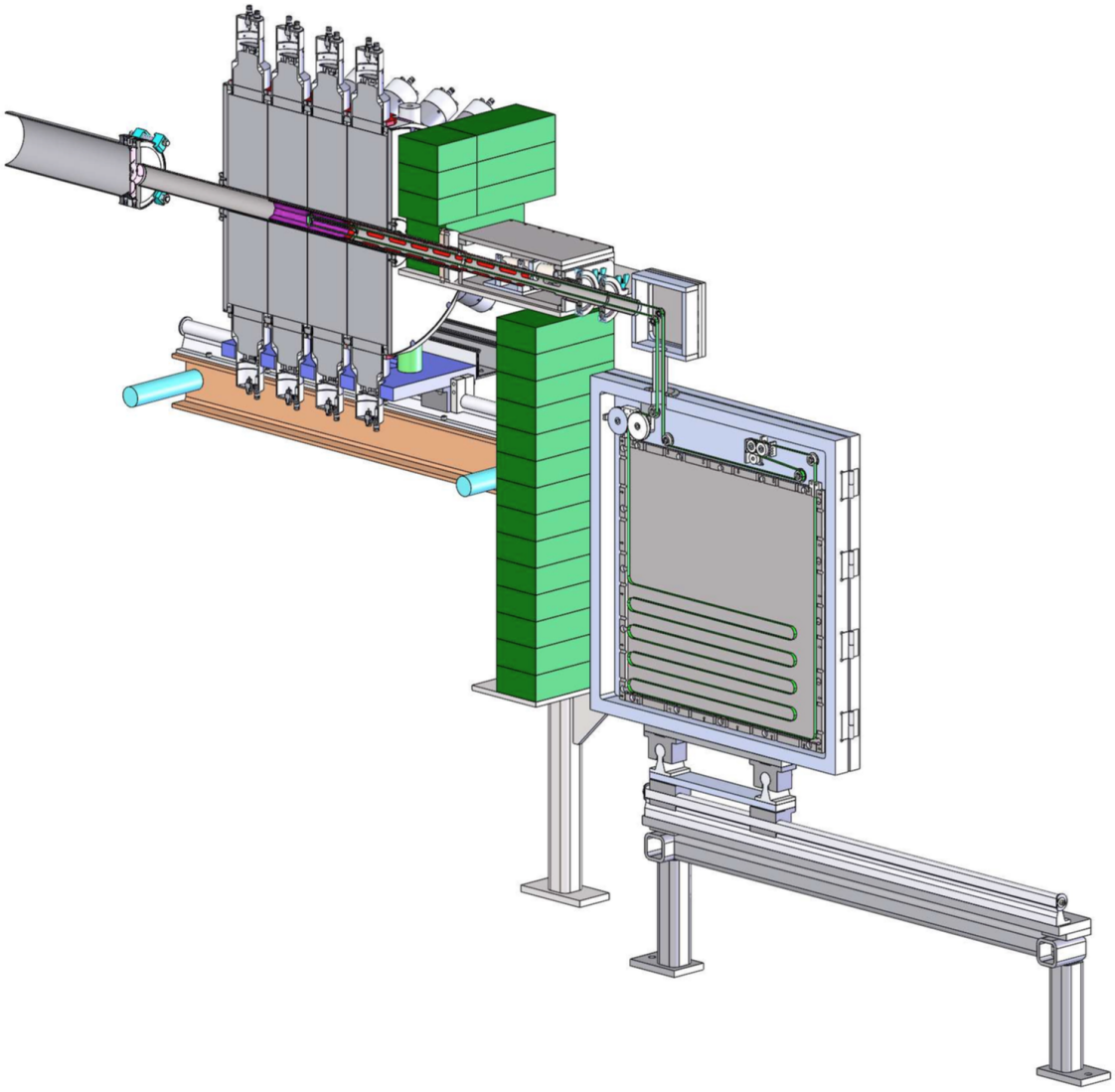

Figure 4.3 Schematic of the SuNTAN setup, from Ref. [49].

light that could escape. Figure 4.4 shows a picture of the plastic scintillator and the 32 fiber optics.

Two PMTs were optically coupled to 16 of the optical fibers each, to collect the fiber signals, see Figure 4.5. The optical fibers have alternating couplings to the two PMTS for noise reduction purposes. Following the β decay, the fiber detector was used to detect the β particle, in this case, the electron. We required both PMTs in the fiber detector to have energies above thresholds, which helped to reduce random noise. The fiber spectra, gated with a coincidence in SuN and a signal in the other fiber detector, are shown in Figure 4.6.

‘

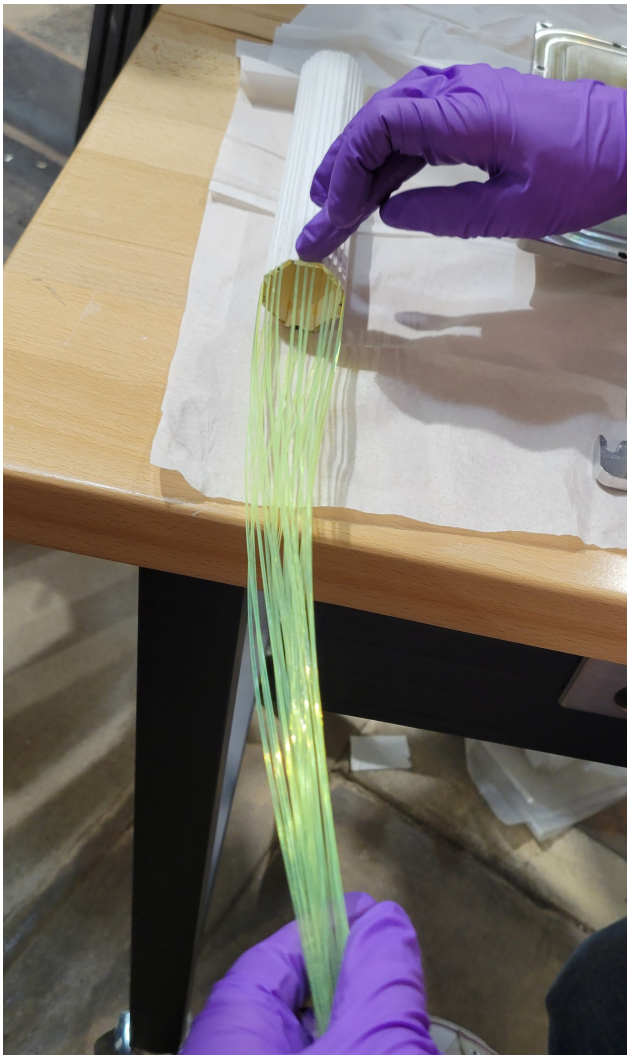

Figure 4.4 Picture of the plastic scintillator, SuNSPOT, with 32 wave-shifting optical fibers glued on the six sides, which is optically coupled to two PMTs to detect the β-particles.

4.5 Gain matching

Since each segment of SuN has three PMTs, the full signal is the sum of the output from all of the three PMTs. This means that the PMTs all have to match within a segment. A rough gain matching was performed before the experiment by adjusting the high voltage of each PMT. Further gain matching was performed during online analysis, and separately for this work offline. To gain match the segment, we recorded long background runs. There is naturally occurring radioactivity from isotopes like ^{40}K, which is present in the room background measurements. ^{40}K has a signature γ ray with an energy of 1460 keV. A Gaussian fit of this peak was performed for each PMT, with a linear background. Then, choosing one of the centrally placed PMTs as the norm with gain = 1,

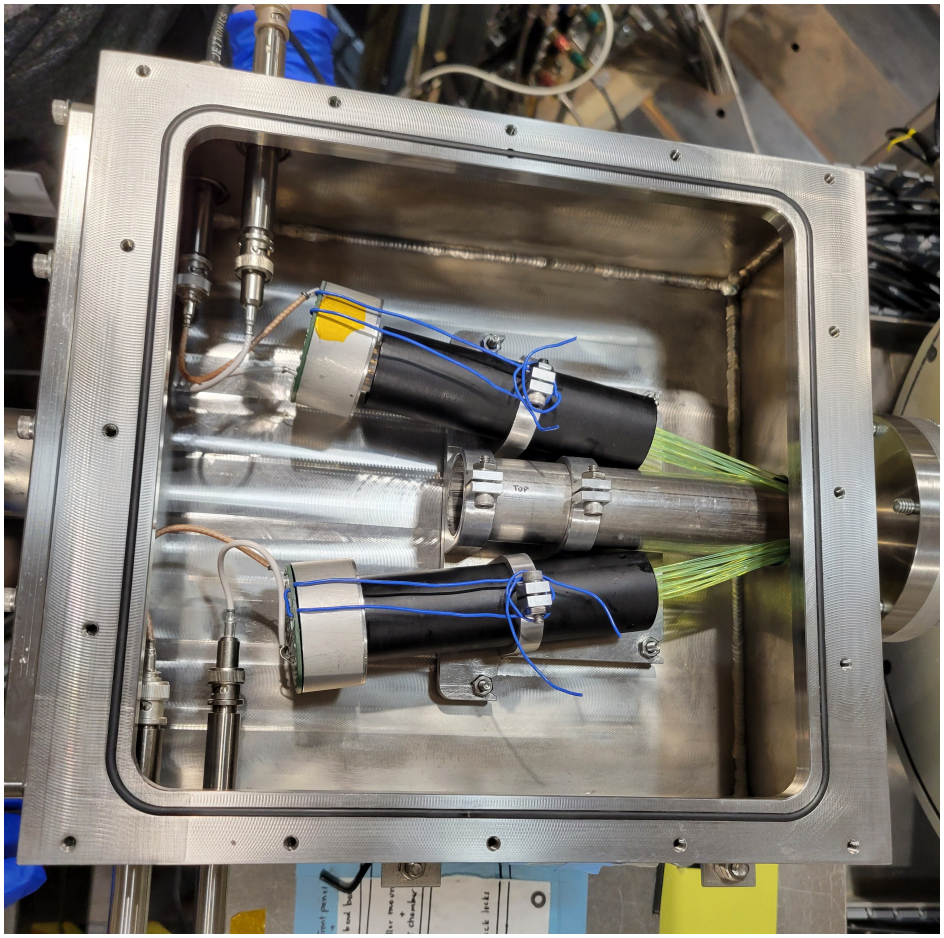

Figure 4.5 Picture of the two PMTs connected to plastic scintillator, SuNSPOT, to detect the β-particles.

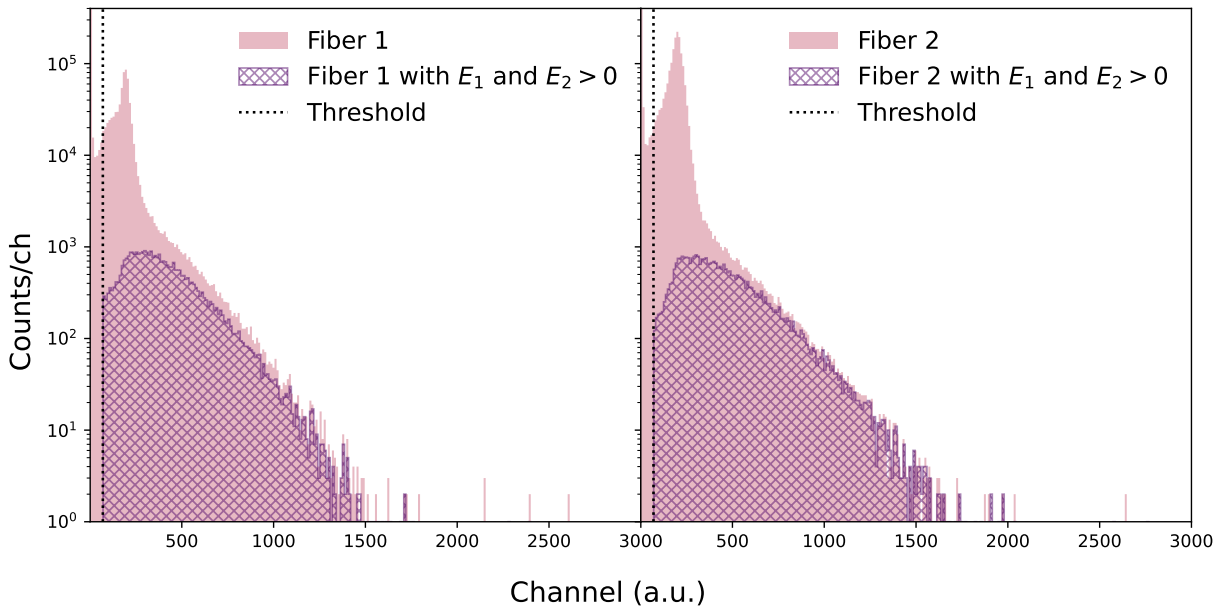

Figure 4.6 Fiber energies for fiber 1 (E_1) and fiber 2 (E_2) detectors. The energy gates are set at the marked locations for them respectively, and gated on the SuN spectra. This was because the first part before the reduction of counts was primarily random noise which was undesirable to include in the data set.

Table 4.1 Values for the mean, μ, of the Gaussian fit to the ^{40}K peak at 1460 keV, along with the calculated gain coefficient that was applied to the PMTs in all of the data.

Half	Segment	PMT	μ (ch)	Gain
Bottom	1	1	982.0	1.0108
Bottom	1	2	1011.3	0.9816
Bottom	1	3	980.0	1.0130
Bottom	2	1	1001.0	0.9917
Bottom	2	2	977.0	1.0161
Bottom	2	3	989.6	1.0031
Bottom	3	1	969.4	1.0240
Bottom	3	2	992.7	1.0000
Bottom	3	3	1003.8	0.9890
Bottom	4	1	992.8	0.9998
Bottom	4	2	977.9	1.0152
Bottom	4	3	987.2	1.0055
Top	1	1	1016.8	0.9763
Top	1	2	998.5	0.9941
Top	1	3	991.0	1.0017
Top	2	1	955.9	1.0385
Top	2	2	997.0	0.9956
Top	2	3	975.5	1.0177
Top	3	1	981.2	1.0117
Top	3	2	992.3	1.0004
Top	3	3	974.4	1.0188
Top	4	1	994.9	0.9978
Top	4	2	962.9	1.0309
Top	4	3	979.6	1.0133

calculated the gain coefficient needed to match the fitted peak to this central reference PMT. The gain was calculated by:

$$\text{gain} = \frac{\text{peak}_{\text{ref}}}{\text{peak}}. \tag{4.1}$$

After the gain coefficients were applied, the runs could be sorted with summing all the gain-matched PMTs. The gain-matched PMTs for SuN are shown in Figure 4.7, where each subplot corresponds to one segment in the SuN detector. The gain-coefficients are presented in Table 4.1.

4.6 Energy calibration

For energy calibrations, we used four γ-emitting sources, ^{60}Co, ^{241}Am ^{207}Bi and ^{228}Th. This was done segment by segment, using the known γ-ray energies. A fit of each peak was done

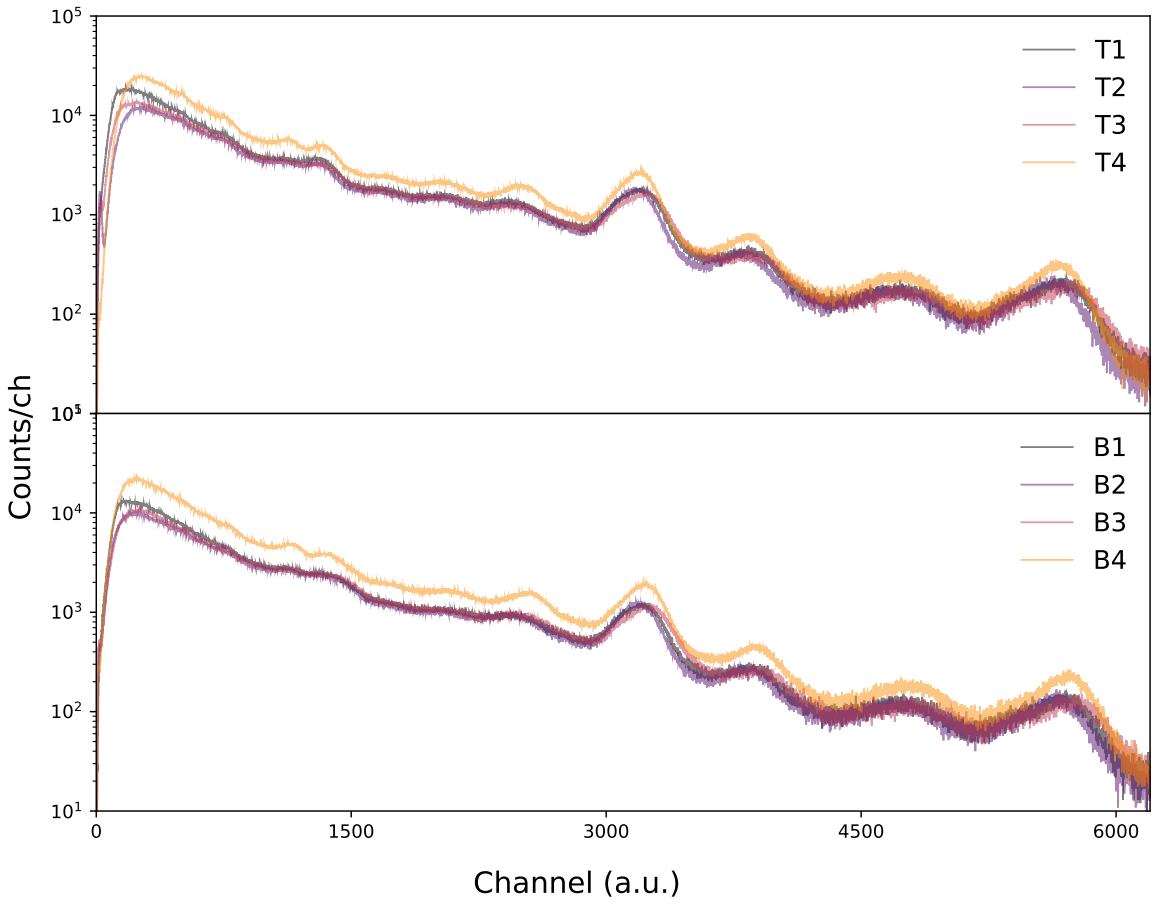

Figure 4.7 SuN's eight segments plotted together for the bottom and top halves of SuN, where the three corresponding PMTs summed after gain matching to the room background peak from ^{40}K right above channel 3000.

with a Gaussian function, and then the centroid of the Gaussian was extracted. After fitting all distinguishable and known peaks, we performed a linear regression to find the gain and offset for each segment. All segments were then calibrated with the extracted parameters, which means that each channel number was converted to energy in keV.

4.6.1 ^{60}Co

A standard calibration source used was ^{60}Co. The ^{60}Co source β^- decays to the child ^{60}Ni, in an excited state at 2505.7 keV. This excited state will then de-excite to the ground state of ^{60}Ni by emitting two distinct γ rays, 1173.2 keV and 1332.5 keV [50]. The corresponding peaks in each segment were fitted as two Gaussian functions, with a linear background. See Figures 4.8 and 4.9 for the fits of the individual segments in the top and bottom half of the SuN detector. The shoulder

that appears on the right-hand side of the 1332 keV peak in the outer segments (seg. 1 and 4) correspond to the ^{40}K background peak.

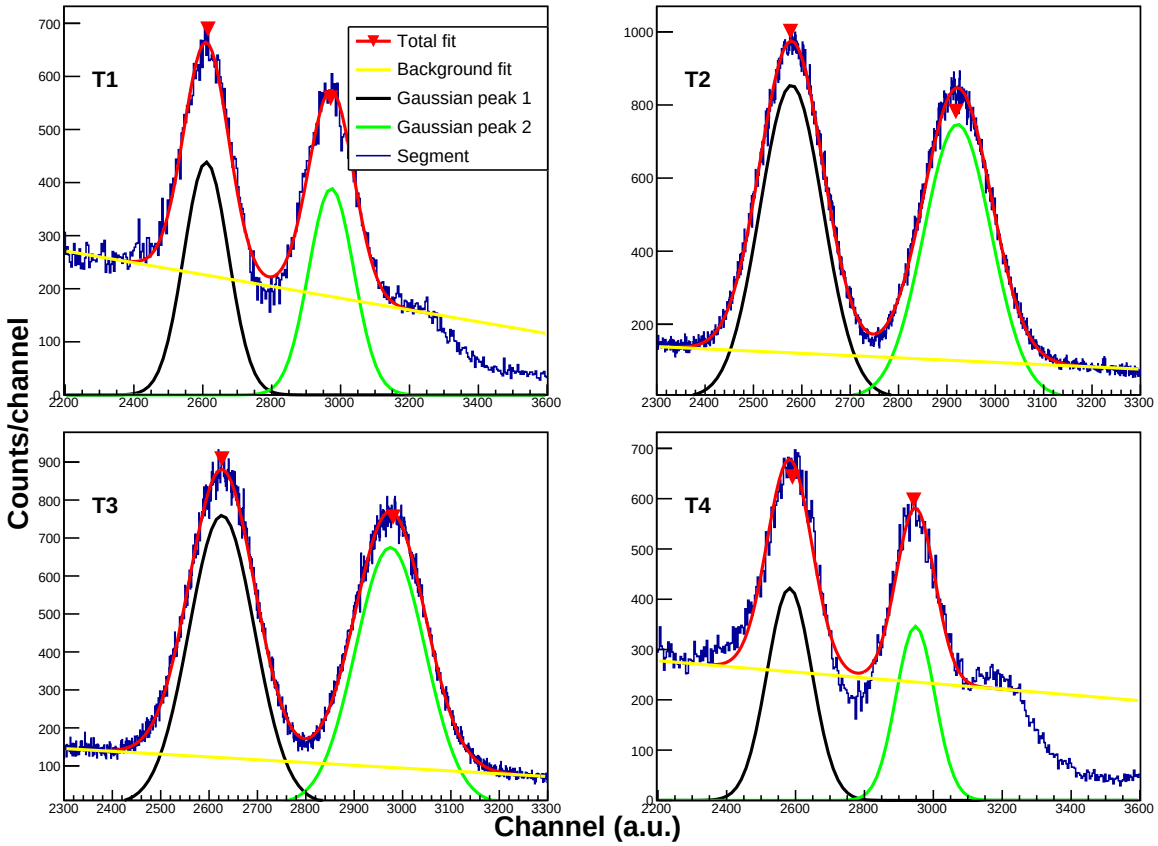

Figure 4.8 Fits for the 1173 keV and 1332 keV peaks from the ^{60}Co source, for the top segments in the SuN detector. The two peaks are fitted with a combination of two Gaussian peaks and a linear background.

4.6.2 ^{241}Am

A standard calibration source used was ^{241}Am. ^{241}Am α decays to ^{237}Np with a half-life of over 432 years [51]. From the α decay, a state at 59.5 keV in ^{237}Np is strongly preferred [52]. This source was also used to set the thresholds for the segments before the experiment to ensure that we can see the low-energy peaks, while still excluding noise. The peak was fitted as a Gaussian function with a linear background. See Figures 4.10 and 4.11 for the fits of the individual segments in the top and bottom half of the SuN detector, respectively.

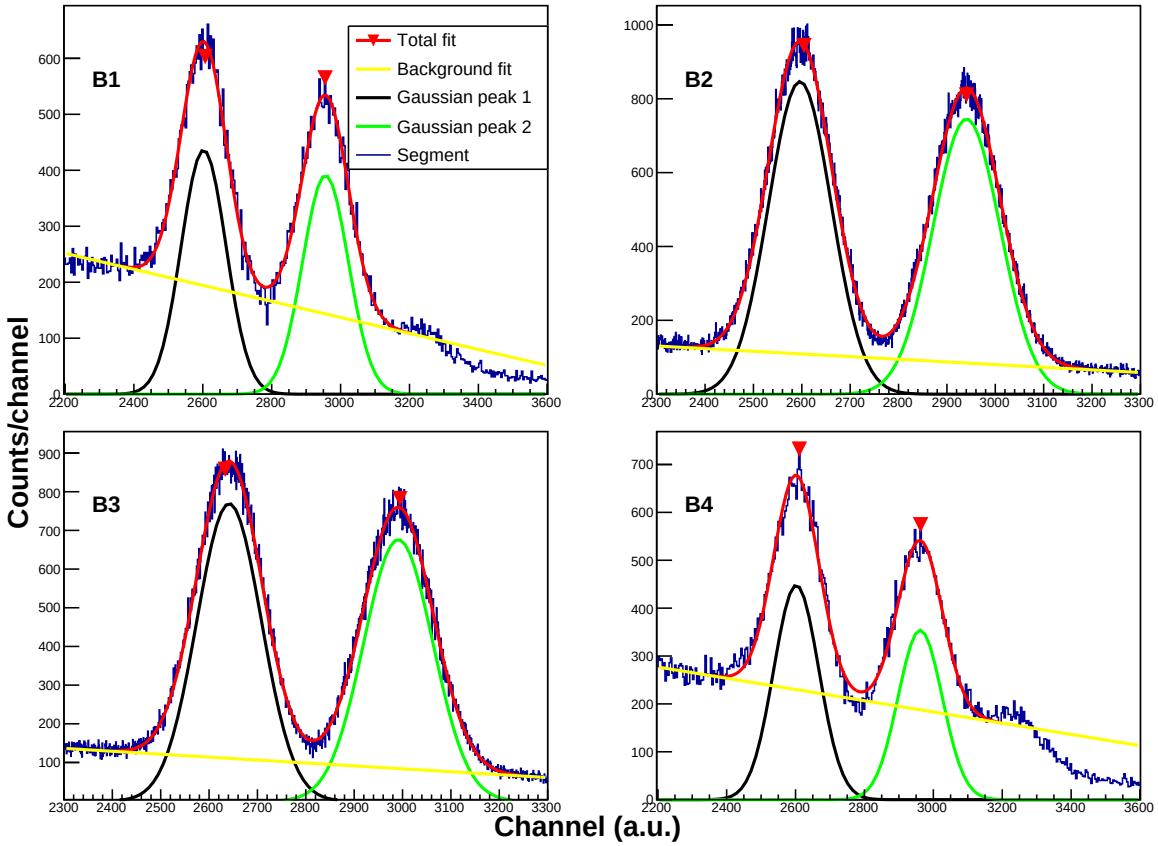

Figure 4.9 Fits for the 1173 keV and 1332 keV peaks from the ^{60}Co source, for the bottom segments in the SuN detector. The two peaks are fitted with a combination of two Gaussian peaks and a linear background.

4.6.3 ^{228}Th

A standard calibration source used was ^{228}Th, with several well characterized peaks. Since ^{228}Th is a source that also emits α-particles, with a half-life of approximately 2 years [53], the child is still far from stability, and there are several more decays in the chain before it ends at the stable ^{208}Pb, see Refs. [53]–[57]. From this decay chain, the γ-ray peak with $E_\gamma = 2614$ keV was used, which comes from the final de-excitation in the decay chain, from the β decay of ^{208}Tl into the 3^- state in ^{208}Pb [57]. The peak was fitted with a Gaussian function with a linear background. See Figures 4.12 and 4.13 for the fits of the individual segments for the top and bottom halves of the SuN detector for the $E_\gamma = 2614$ keV peak.

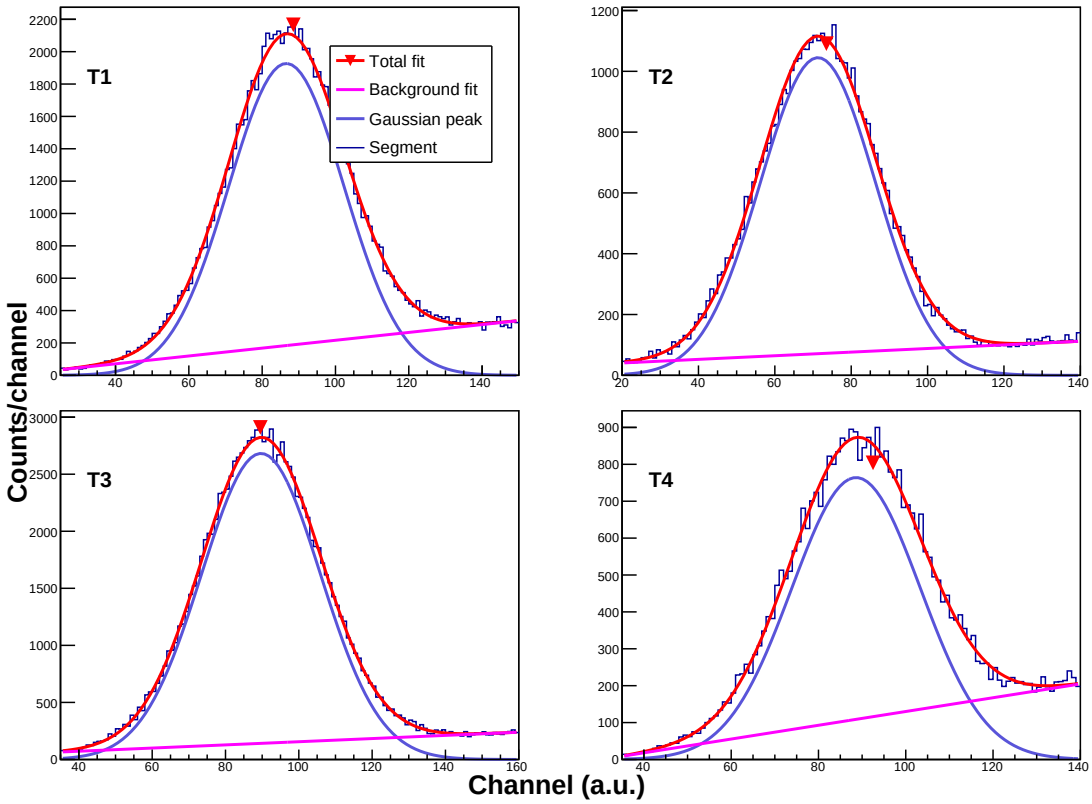

Figure 4.10 Fits for the 60 keV peak from the ^{241}Am source, for the top segments in the SuN detector. The peak was fitted with a Gaussian function, with a linear background.

4.6.4 ^{137}Cs

A standard calibration source used was ^{137}Cs, with a prominent peak at 661.7 keV from excited state populated from the β^- decay of ^{137}Cs to ^{137}Ba, with a half-life of 30 years [58]. The peak was fitted with a Gaussian function, with a linear background. See Figures 4.14 and 4.15 for the fits of the individual segments in the top and bottom halves in the detector.

4.6.5 Linear regression

After performing the gain matching for each of the PMTs, each segment was calibrated separately. To find the linear calibration coefficients, we performed a linear regression using the known peaks of our calibration sources and the measured channels for those corresponding peaks with:

$$E(ch) = slope \times ch + offset, \tag{4.2}$$

where *slope* is the multiplication factor needed, *ch* is the channel number, and *offset* is the constant added to find the corresponding energy $E(ch)$ in Equation (4.2).

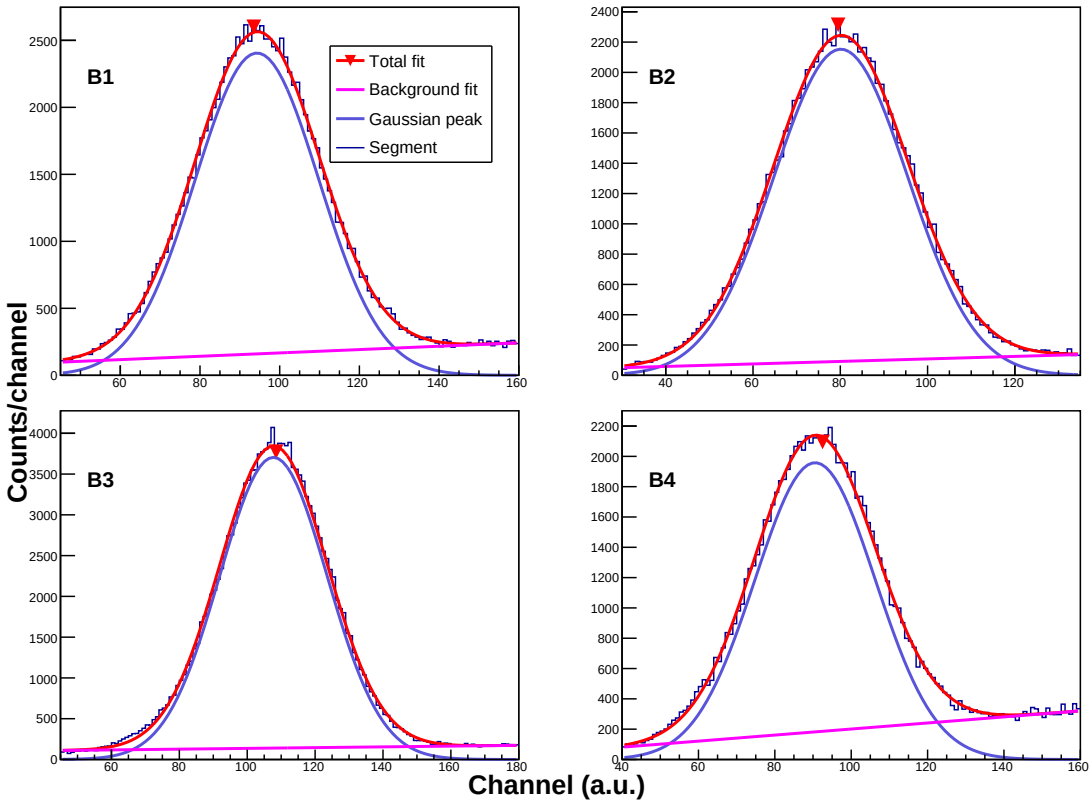

Figure 4.11 Fits for the 60 keV peak from the ^{241}Am source, for the bottom segments in the SuN detector. The peak was fitted with a Gaussian function, with a linear background.

Segment	Gain (keV/ch)	Offset (keV)
B1	0.4568	-7.866
B2	0.4576	-3.029
B3	0.4525	-11.527
B4	0.4557	-5.451
T1	0.4547	-6.547
T2	0.4590	1.008
T3	0.4530	-5.144
T4	0.4586	-5.967

Table 4.2 Linear calibration coefficients, gain, and offset, for all the segments in SuN for this experiment.

The calibration coefficients are presented in Table 4.2, where the $slope$ and $offset$ were extracted from linear regression, as shown in Figure 4.16. The data used in the linear regression are shown in Table A.1. In Figure 4.16, it can be seen that the linear regression intersects with all of the calibration peaks, which indicates a consistent calibration for the SuN segments.

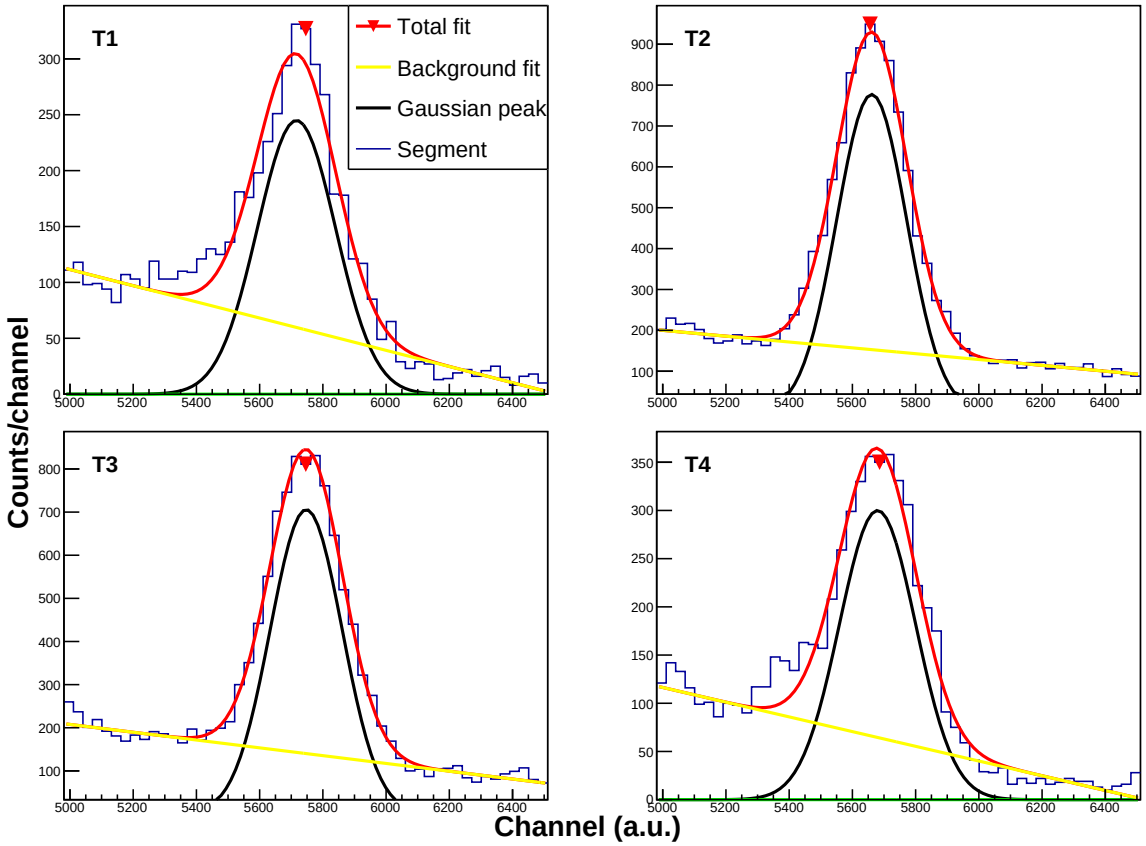

Figure 4.12 Fit for the $E_\gamma = 2614$ keV peak from the ^{228}Th source, for the top segments in the SuN detector. The peaks were fitted with a combination of a Gaussian function and a linear background for each instance.

4.7 Calibrated spectra

After applying calibrations to the ^{60}Co runs, we can see the sum of segments (SoS) and the total absorption spectra (TAS) in Figures 4.17 and 4.18 respectively. The SoS is the spectra from the central segments in SuN (T2, T3, B2, B3), which shows the individual γ-ray energies (E_γ). TAS is the event-by-event sum from all of the segments in SuN, which represents the total excitation energy (E_x).

In the SoS (Figure 4.17), the individual γ rays can be seen for the decay, with some summing happening of the two γs at 2505 keV. The TAS from the ^{60}Co decay (Figure 4.18), there is some incomplete summing with individual γs at 1173 keV and 1332 keV, and there is background contribution from ^{40}K.

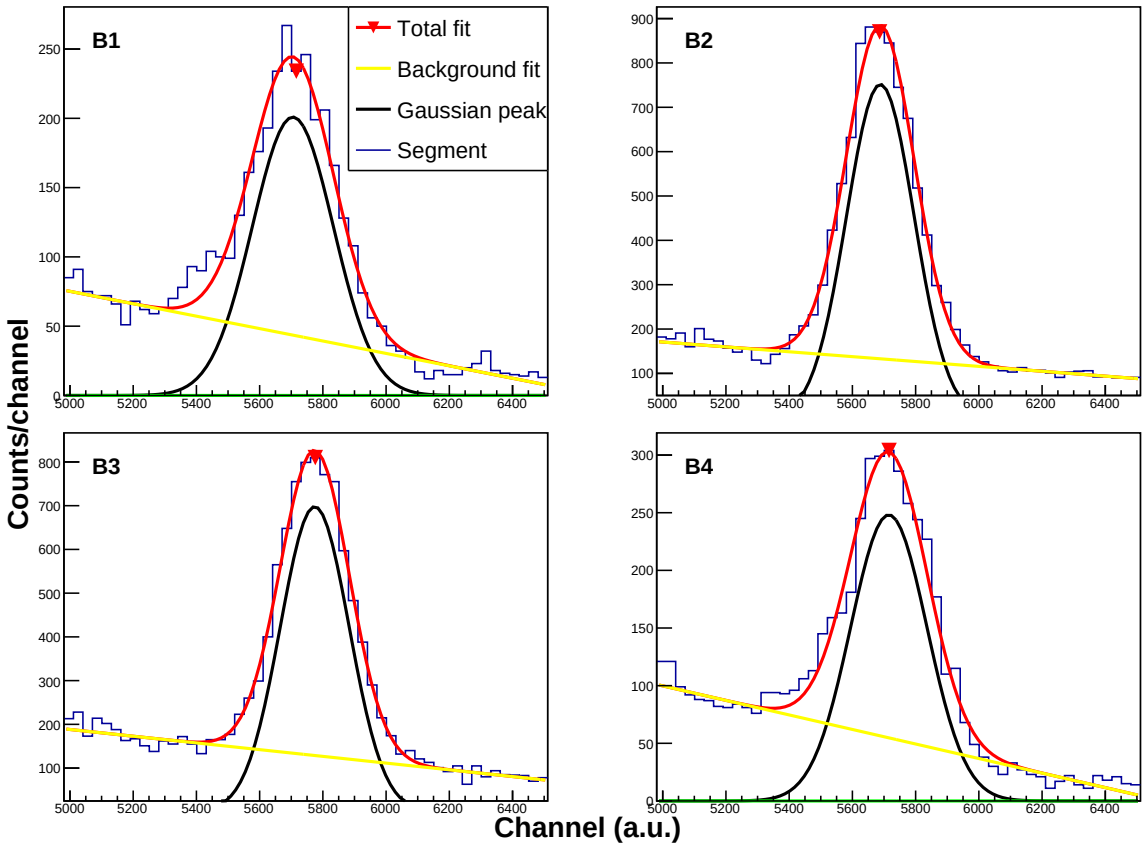

Figure 4.13 Fit for the $E_\gamma = 2614$ keV peak from the ^{228}Th source, for the top segments in the SuN detector. The peaks were fitted with a combination of a Gaussian function and a linear background for each instance.

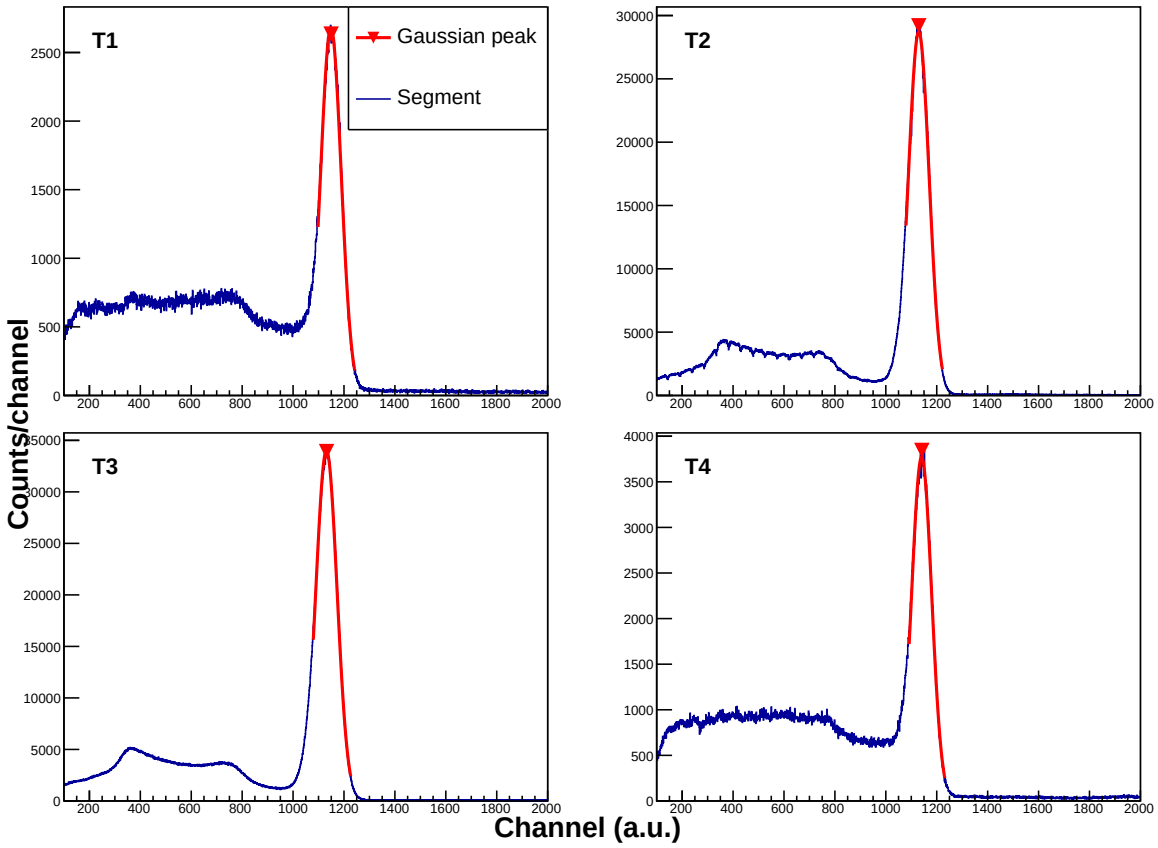

Figure 4.14 Fits for the 662 keV peak from the ^{137}Cs source, for the top segments in the SuN detector. The peak was fitted with a combination of a Gaussian function and a linear background for each instance.

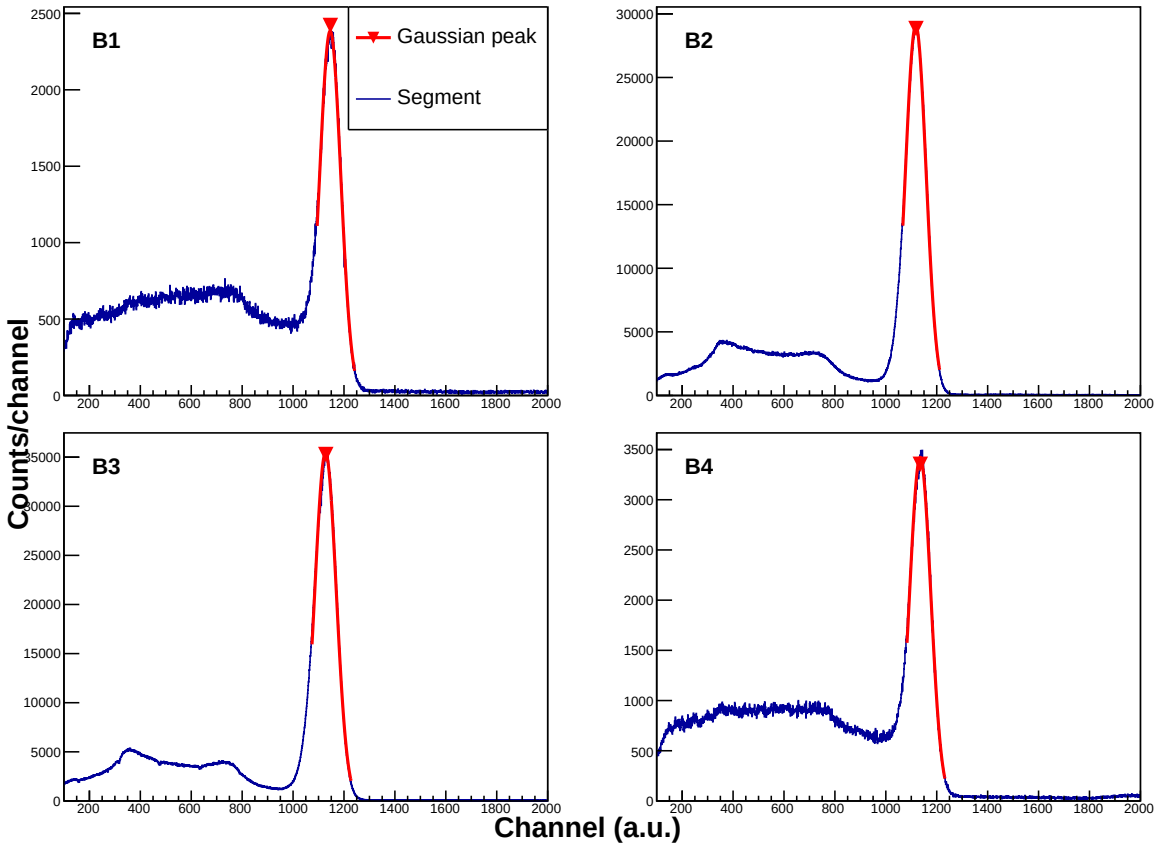

Figure 4.15 Fits for the 662 keV peak from the ^{137}Cs source, for the bottom segments in the SuN detector. The peak was fitted with a combination of a Gaussian function and a linear background for each instance.

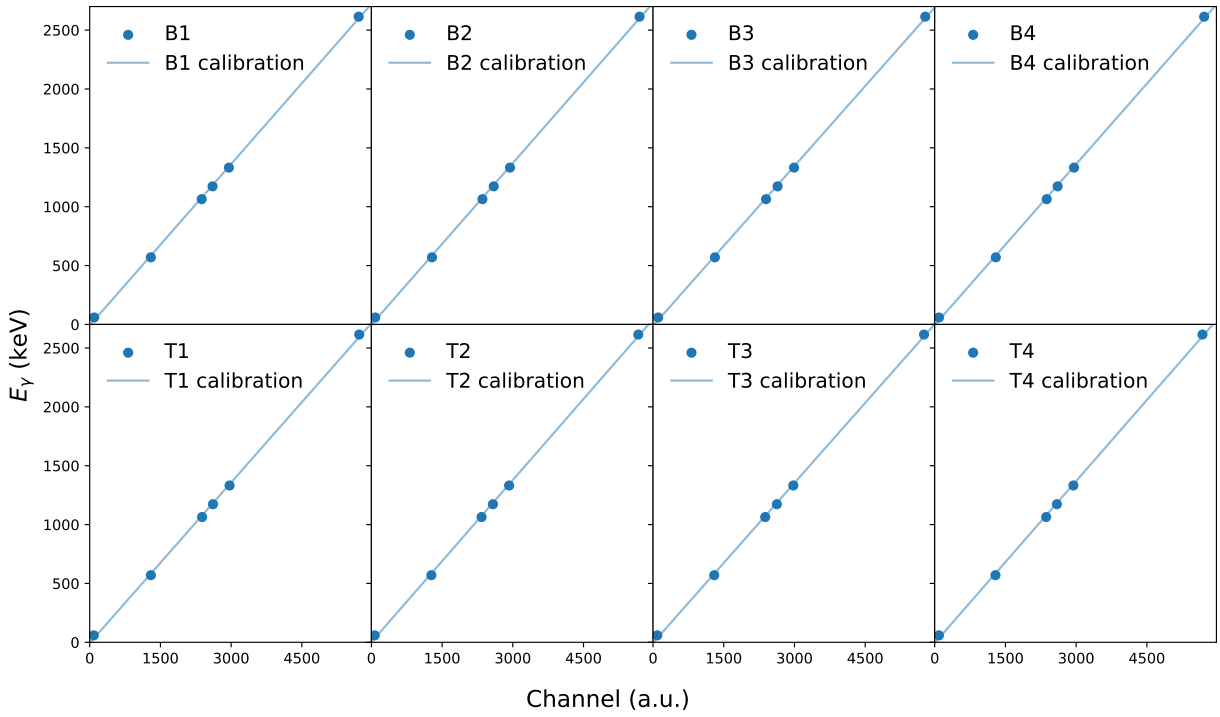

Figure 4.16 The known peaks at different γ energies, E_γ, from our calibration sources are on the y-axis, with the corresponding channel from our calibration runs, plotted as blue dots. The solid blue line shows the linear calibration for the segment.

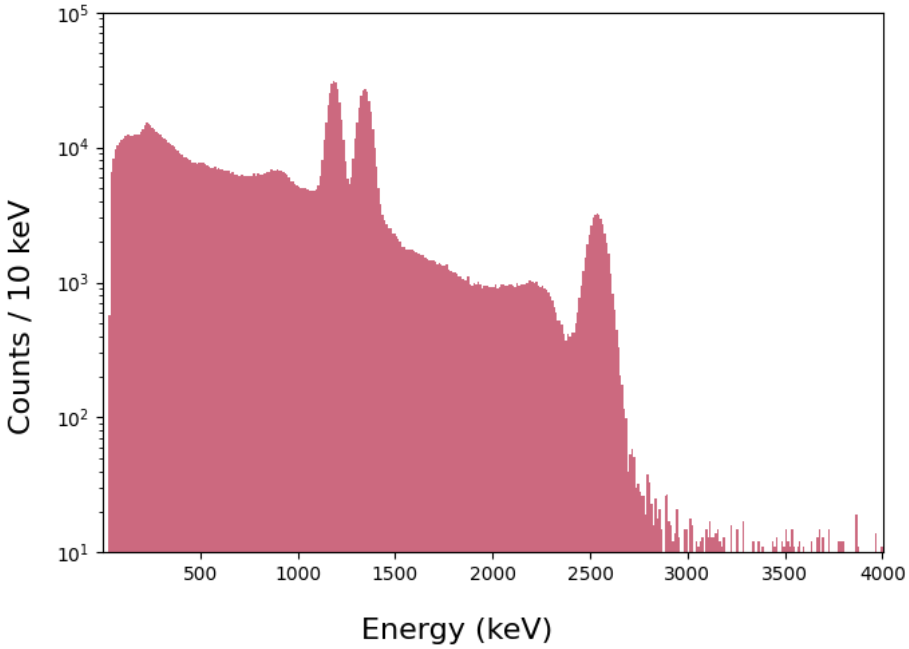

Figure 4.17 The calibrated sum of segments for ^{60}Co, where the two characteristic peaks are at 1173 keV and 1332 keV.

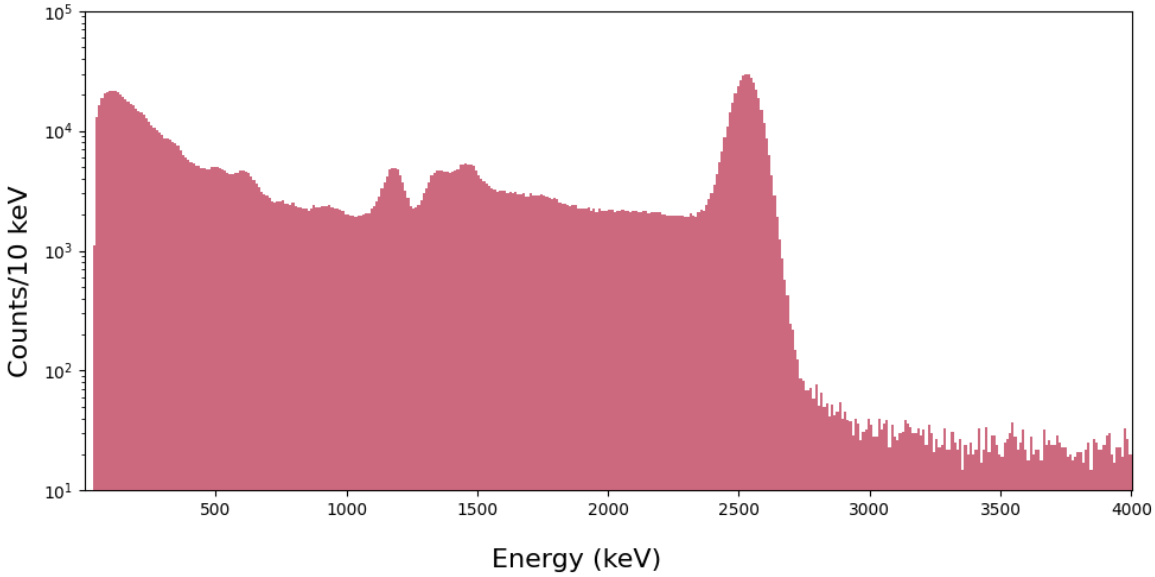

Figure 4.18 The calibrated TAS for ^{60}Co, with the sum of the two characteristic peaks at 2505 keV.

CHAPTER 5

BACKGROUND SUBTRACTION

When doing an experiment, we try to minimize any source of contamination in the data from decays of other isotopes in the beam, or room background. Room background can come from radioactive isotopes like ^{40}K, and cosmic ray radiation. A typical room background spectrum taken with the SuN detector over $\sim$ 30 minutes can be seen in Figure 5.1. While the background interactions with SuN are significant, requiring a coincidence with SuNSPOT reduced this background.

In this work, these background contributions were reduced during the analysis, as all events were gated on SuNSPOT. Higher energy background from cosmic rays typically show up at very large energies, which are above the energy range we study for the β decay. For our background subtraction, we used the same cuts as for the collection of data. This means that we require both SuNSPOT PMTs to have an energy reading (channel>70), the time window for the two PMTs to be short, and the time window for the SuNSPOT PMT and the first SuN PMT to be sufficiently close

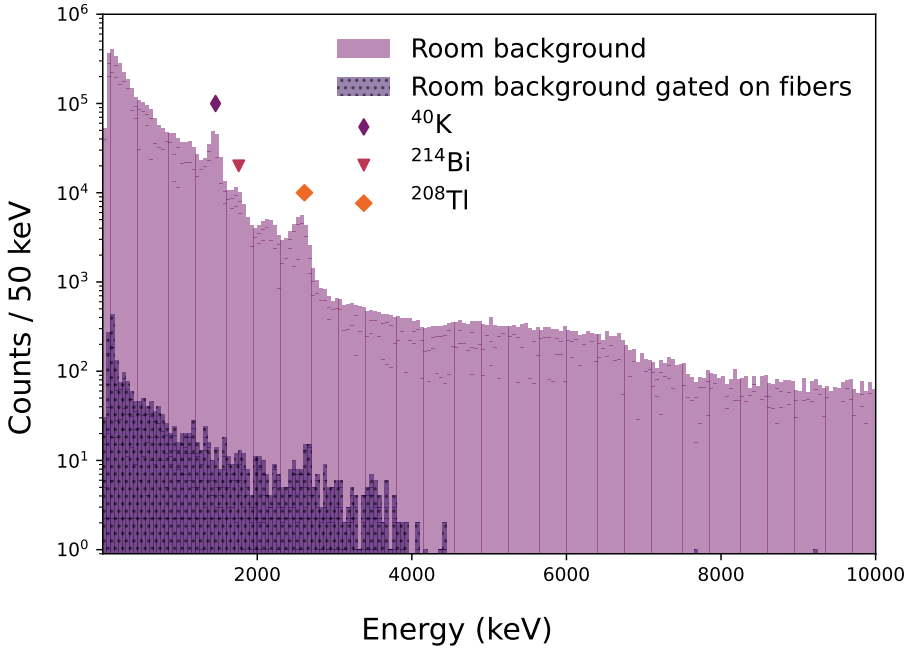

Figure 5.1 Room background, compared to room background gated on SuNSPOT, from the sum of segments (SoS).

as well. In this way we were able to significantly reduce high-energy room background, as gating on all of these time windows reduces the amount of random coincidences, which means that fewer of the PMTs see anything as well.

With the presence of possible beam contaminants in the spectra, proper background subtraction or time gates were essential to create the particle-γ matrix needed for the β-Oslo method. For the A=152 beam, the applied time gates were sufficient to create the particle-γ matrix, while more extensive background subtraction and scaling was needed for the A = 154 beam setting.

5.1 A = 152

For studying the neutron-capture cross section on ^{151}Nd, we need to populate excited states in the ^{152}Nd from the β decay from ^{152}Pr. The beam rates can be seen in Table 5.1. From Table 5.1, we see that the isotope of interest, ^{152}Pr, is the second most abundant in the beam, after ^{152}Nd, being the most abundant at 48%. With the much longer half-life of ^{152}Nd, the contamination in the γ spectra was much smaller. The grandchild contribution from ^{152}Pm and ^{152m}Pm is 7%, but it did not contribute to a significant portion of the background, due to the much longer half-life compared to the tape cycle.

Table 5.1 Beam rates for Argonne National Laboratory's CARIBU for isobars A = 152, from Ref. [46]. Half-lives are from Ref. [59]. The rates are proportional to the fission yields from ^{252}Ca.

Beam	Rate (pps)	% beam	Half-life	Q_{β^-} (keV)
^{152}Ce	$9.8{\cdot}10^2$	4.3	1.42 s	4780
^{152}Pr	$9.2{\cdot}10^3$	40.4	3.57 s	6390
^{152}Nd	$1.1{\cdot}10^4$	48.3	11.4 min	1105
^{152m}Pm	$8.0{\cdot}10^2$	3.5	7.5 min	3660
^{152}Pm	$8.0{\cdot}10^2$	3.5	4.1 min	3510

For A = 152, the decay chain stops at ^{152}Sm, as this is the first stable nucleus in the decay chain. The decay chain is detailed in Equation (5.1).

$$^{152}\text{Ce} \rightarrow {}^{152}\text{Pr} \rightarrow {}^{152}\text{Nd} \rightarrow {}^{152}\text{Pm} \rightarrow {}^{152}\text{Sm} \tag{5.1}$$

Since the half-lives are known, we were able to investigate the contributions of the grandparent, parent, child, grandchild, and great-grandchild over different intervals of the tape cycle, and optimize

the time period selected to minimize background contributions.

For the A = 152 isobars, we ran with three different tape settings:

1. 60 s beam on, 60 s beam off – for isotope of interest

2. 60 s beam on, 1 s beam off – for isotope of interest

3. 30 min beam on, 30 min beam off – for background subtraction

To maximize the data from the isotope of interest, we chose the time interval that gave the largest overall percentage contribution from ^{152}Pr activity while keeping any contaminants to a minimum. The calculated decay curves for this tape setting, is shown in Figure 5.2, it can be seen that the primary build up was of the parent, ^{152}Pr, which quickly decayed after the beam stopped at 60 s. For the 60 s on, 60 s off tape cycle, the activity curve from the experiment is shown in Figure 5.3. The calculated activity curves as percentage contribution are shown in Figure 5.4, where we can see that the parent activity dominated for the first $\sim$ 60 s, and then the child activity increased, and eventually surpassed the parent activity at 70 s. After the beam was turned off, the child continued feeding the grandchild, increasing the activity contribution for the grandchild. Past $\sim$ 100 s, the significant source of contamination is from the activity of the grandchild.

Looking at the TAS vs time or sum of segments vs time spectra, Figures 5.5 and 5.6, it is possible to identify states that are longer or shorter lived, and how some of them are very close in energy.

The summed decay curve for the 30 min on, 30 min off tape cycle is shown in Figure 5.7, with the spectra from the experiment in Figure 5.8, the activity percentage curves shown in Figure 5.9. In the longer tape cycle there is beam build-up, shown in Figure 5.7, where a plateau-like feature visible for the parent for the first 30 minutes, along with a sharp drop after beam off. As this build-up is decaying, it can be seen that there is an increase in both the child and grandchild in the decay curve, with the decay from the grandchild dominating after the beam was turned off. From the activity curve in Figure 5.9, as the beam builds up, it can be seen that the percentage of the parent significantly decreases, and is ultimately overtaken by the child and grandchild contributions.

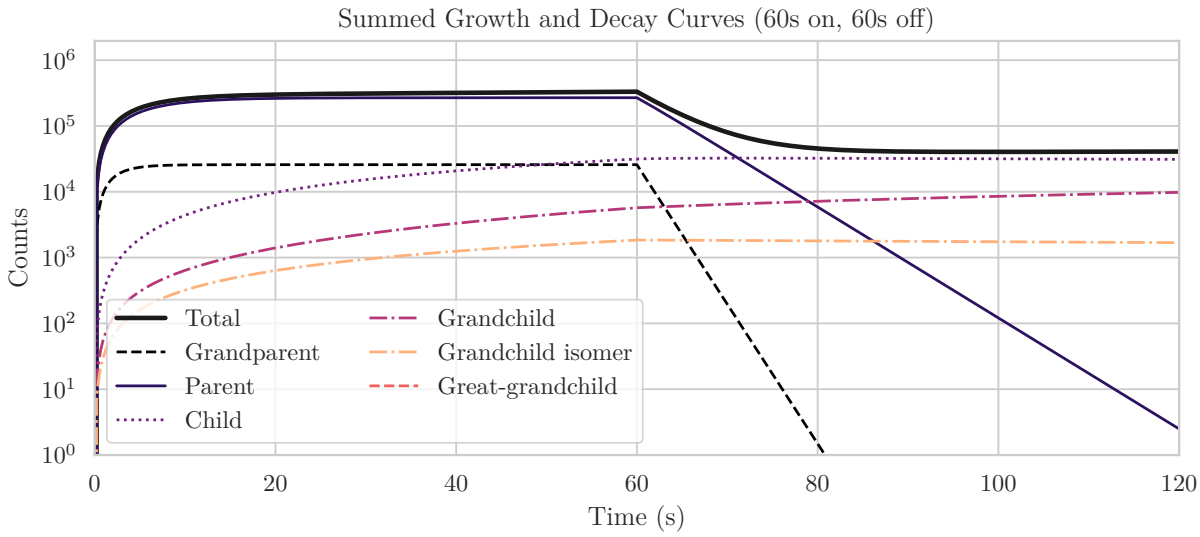

Figure 5.2 Assuming beam make-up as referenced in Table 5.1, the decay curves of the involved isotopes are plotted for the 60 s on, 60 s off tape cycle.

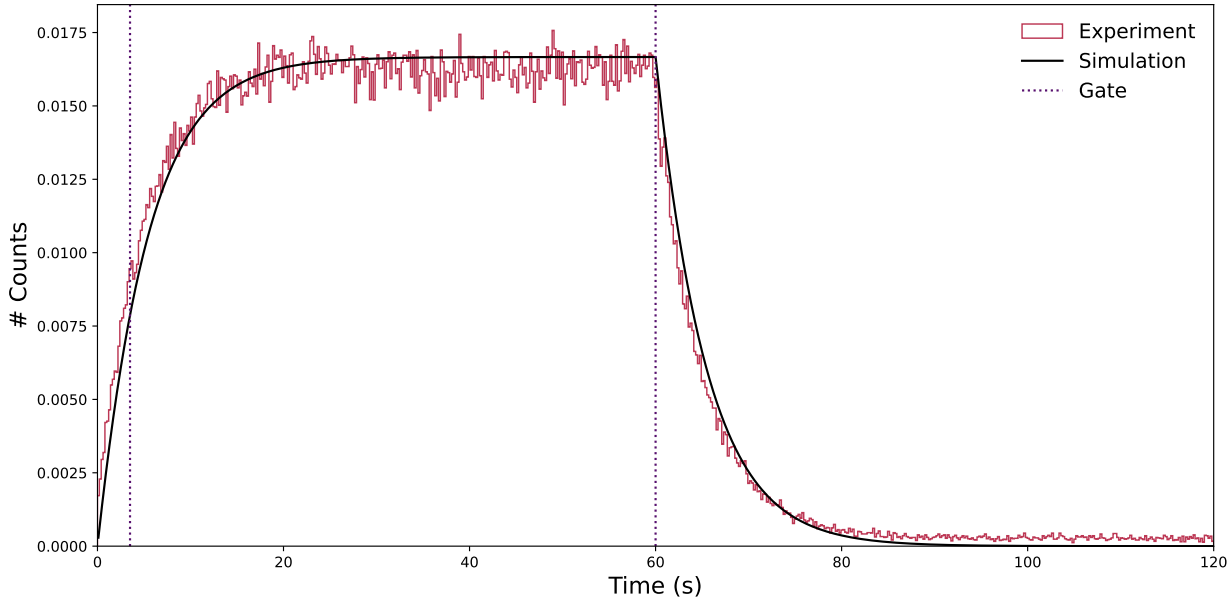

Figure 5.3 Decay curve for A=152 for 60 s on, 60 s off. The beam off coincided with the time gate we applied, which is marked with a dotted line. The simulation is plotted as solid black line.

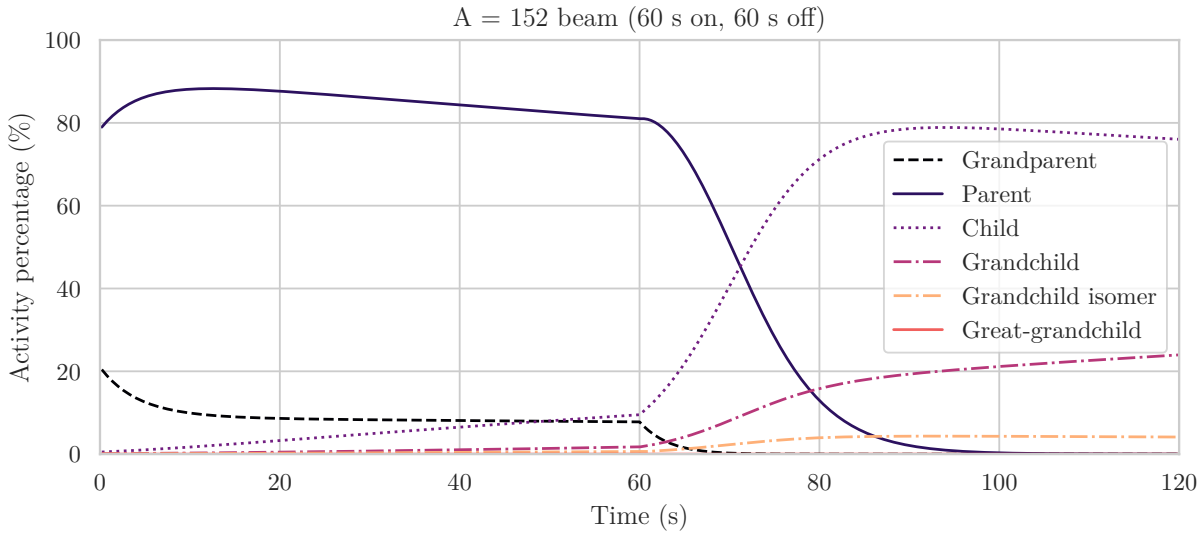

Figure 5.4 Assuming beam make-up is as referenced in Table 5.1, the activity percentage will be as plotted in the activity profile, for the 60 s on, 60 s off tape cycle.

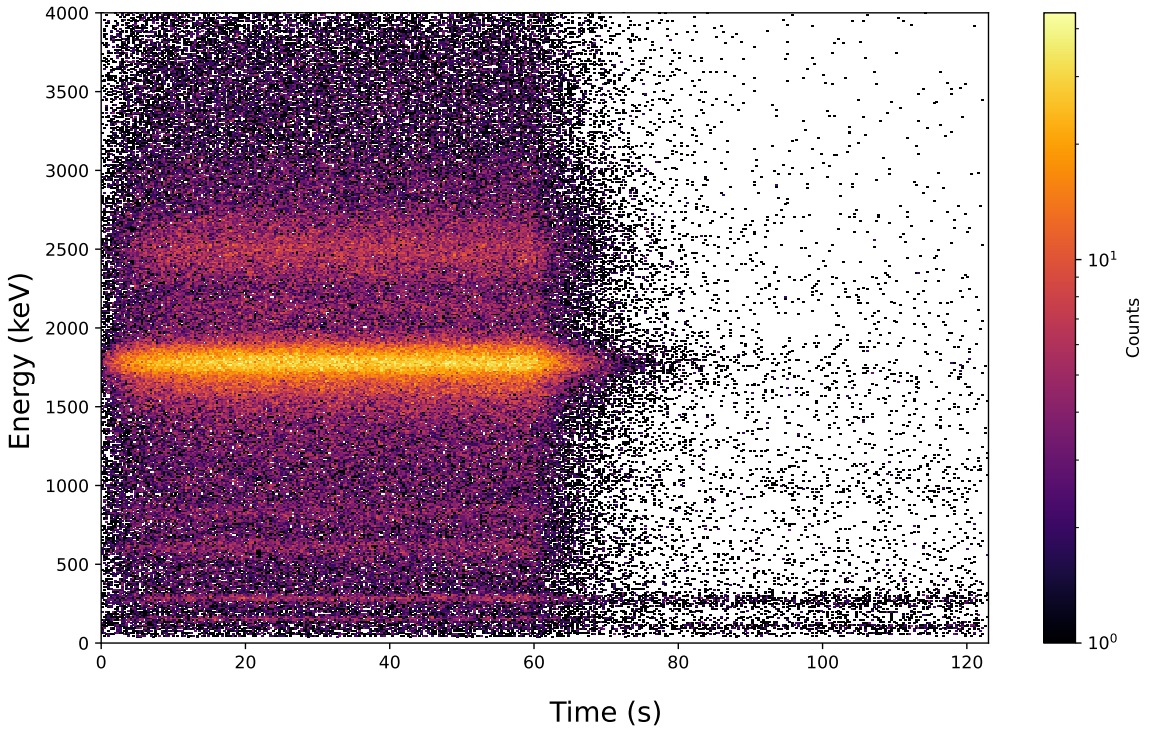

Figure 5.5 TAS vs decay for A=152 for 60 s on, 60 s off. It can be seen that there is a strong population at E_x = 1.8 MeV.

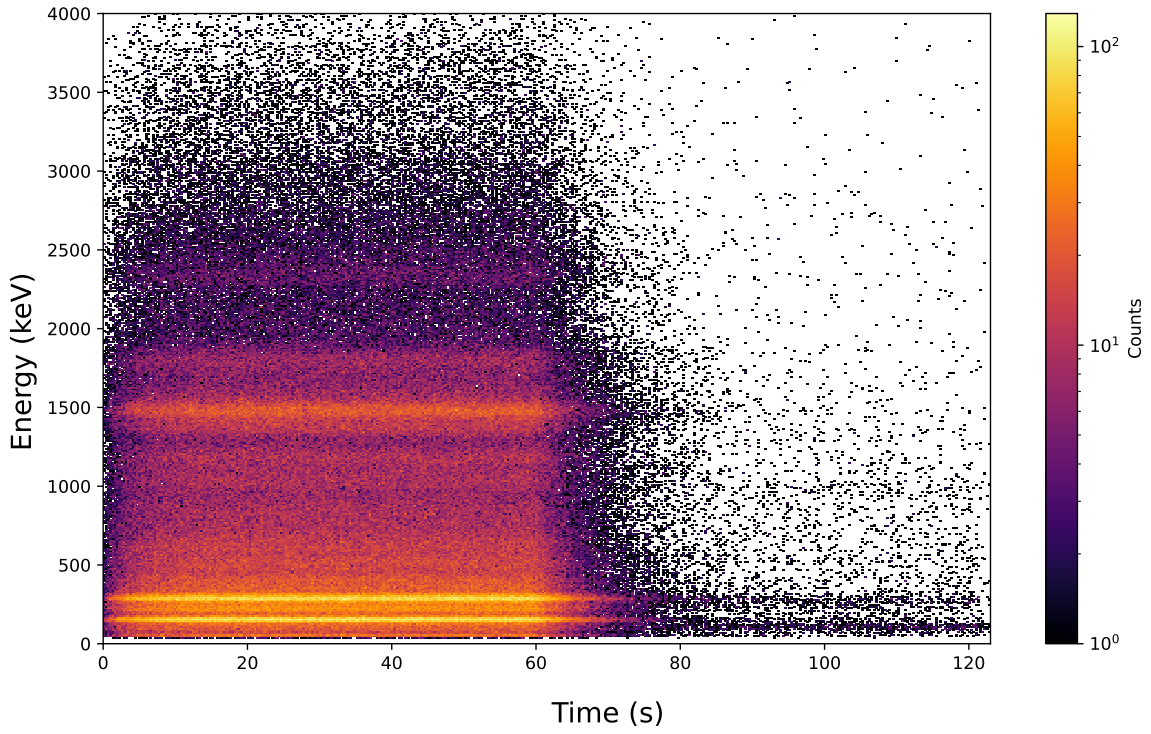

Figure 5.6 SoS vs decay for A=152 for 60 s on, 60 s off. It can be seen that there are several low energy γ-rays that are emitted, and not all of them are from decays from the excited states of ^{152}Nd, as they appear long after the beam-off time

After the beam stop at 30 minutes, the activity is dominated by the decay grandchild as there is not a significant contribution from the child.

For proper background subtraction, it is important to identify the peaks that are from the nuclei of interest compared to the ones that are from other isobars in the beam or decay chain. To investigate this, the TAS vs time and SoS vs time for the shorter tape cycle, Figures 5.5 and 5.6, show that there are no significant contributions from the child or great grandchild within the 60 s on, 60 s off tape cycle.

As a comparison, we can see all the peaks that come from the build-up for the longer tape cycle in the TAS vs decay and SoS vs decay in Figures 5.5 and 5.6. This is not needed for background subtraction, as the contribution from the child and grandchild decay is negligible in the gates shown in Figure 5.3.

From the β-feeding intensities available [59], it is apparent in Figure 5.5 that a large portion of the decays are due to the large population of the 1827 keV state with a tentative assignment of

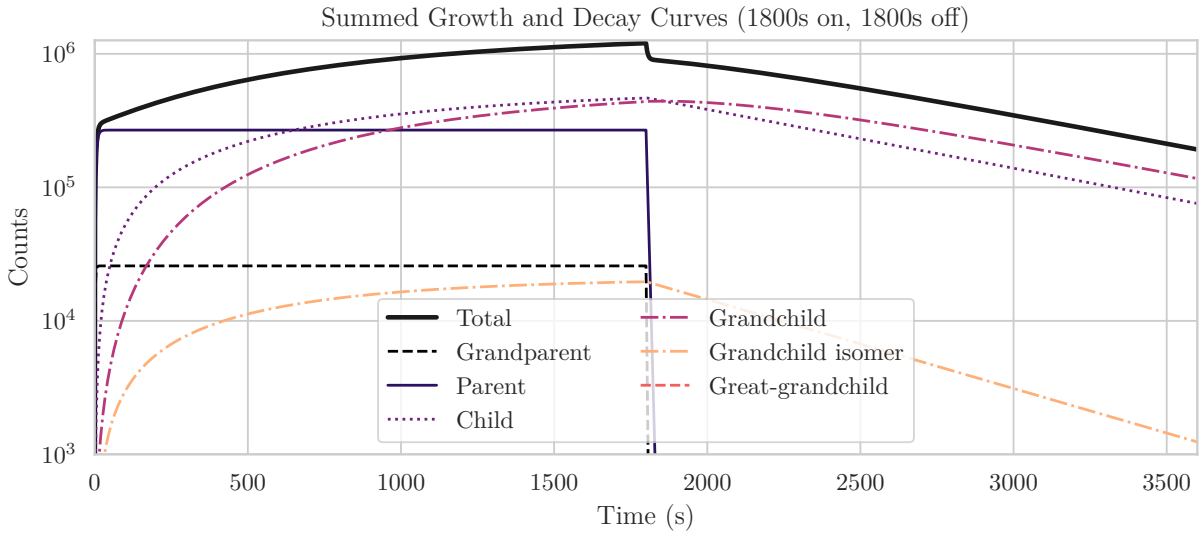

Figure 5.7 Assuming beam make-up is as referenced in Table 5.1, the summed decay will be as plotted for the 30 minutes on, 30 minutes off tape cycle.

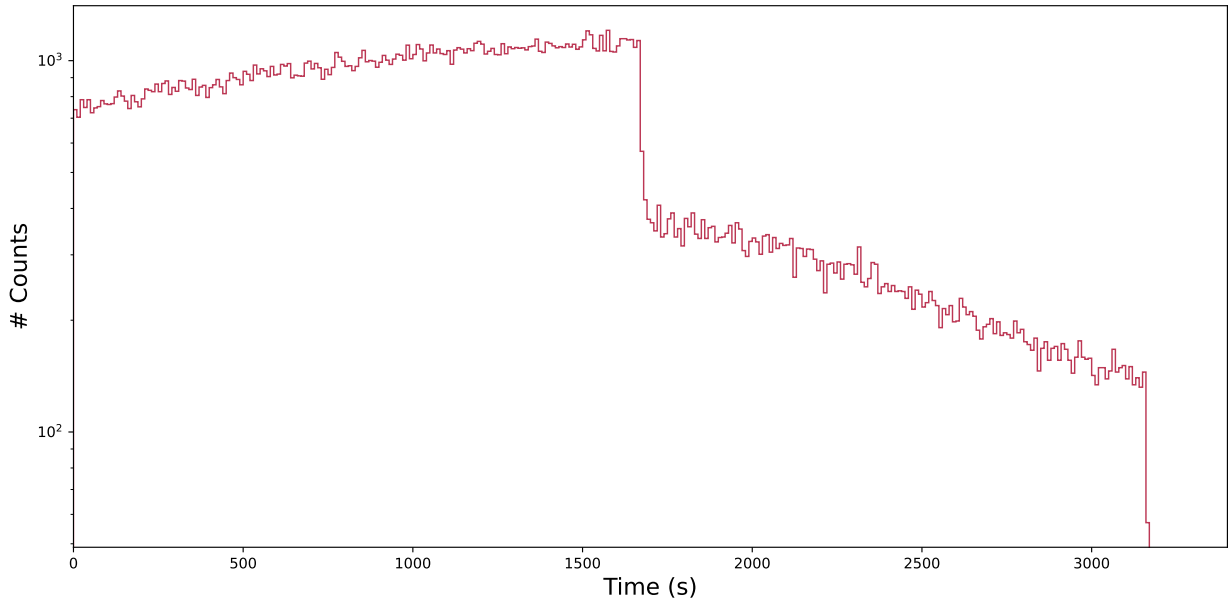

Figure 5.8 Decay curve for one run of the 30 minutes on, 30 minutes off. The build up flattens out with time as the beam is on. There are counts missing at the end because the tape cycle started before the start of the DAQ run.

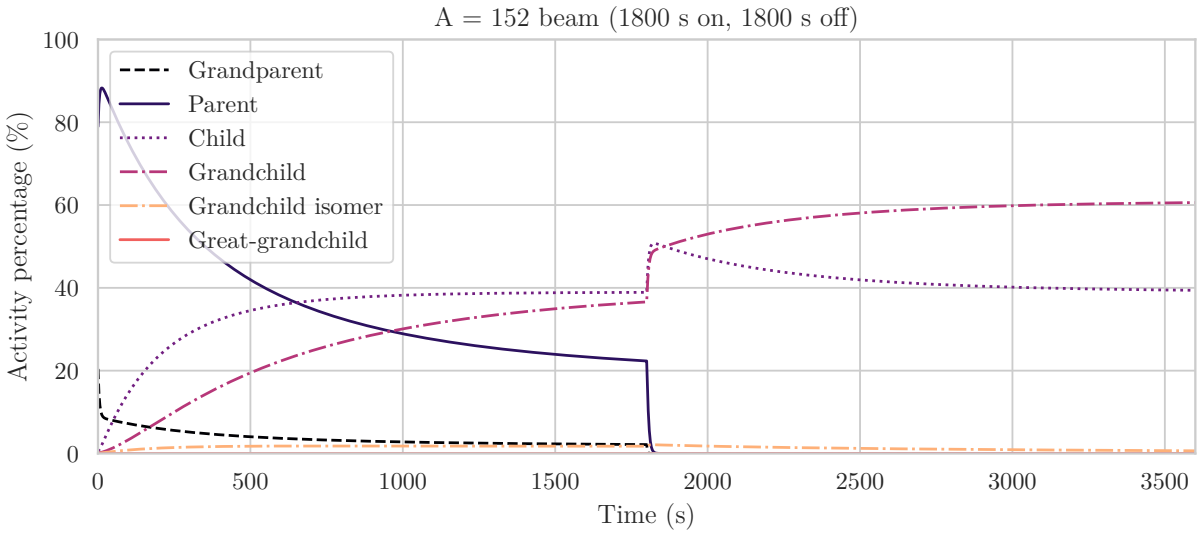

Figure 5.9 Assuming beam make-up is as referenced in Table 5.1, the activity percentage will be as plotted in the activity profile, for the 30 minutes on, 30 minutes off tape cycle.

$J = (3^+)$. Another state that was strongly fed by allowed β decay is the second excited state at 236.55 keV with a spin assignment of $J = 4^+$, which can be observed both in Figures 5.5 and 5.6.

The final spectra for TAS and SoS can be seen in Figures 5.10 and 5.11, and the resulting Oslo-matrix in Figure 5.12. As a reference, in Figures 5.10 and 5.11 a gate on the time being above 1900 s was applied, where the decay was dominated by the child and grandchild. There, we can see that the peaks are not contributing to the spectra in a significant way that impact the analysis. However, for TAS analysis, the longer tape cycles were needed to further reduce the background contribution.

In the SoS comparison in Figure 5.10, it is clear that the major peaks in the long tape cycle do not appear in the short tape cycle. However, some of the lower energy γ-rays are close in energy due to the similarities in the level schemes for the isobars [59]. For the TAS comparison, it can be seen that these same peaks have different intensities, which would be due to the difference in the β-decay intensities. Additionally, above 3 MeV in both the SoS, there are almost no events from the gated long tape cycle, which is due to the lower Q-values for the child and grandchild in the decay chain.

Based on the above analysis of our spectra we concluded that there was no significant background

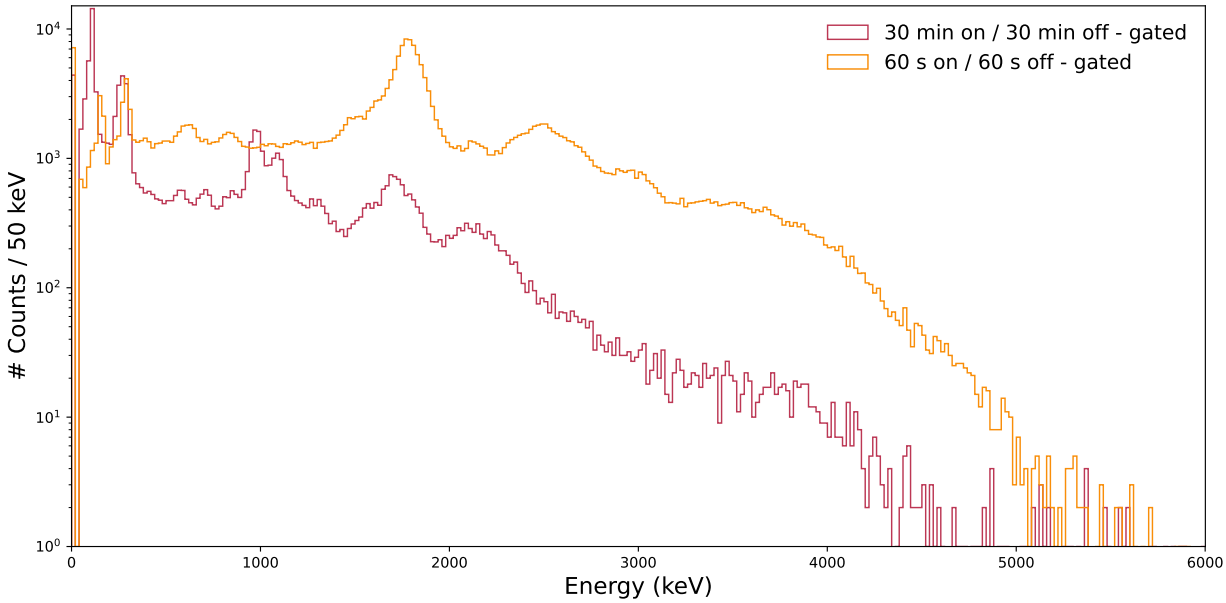

Figure 5.10 SoS comparison for the gated spectra from the two tape settings for A=152. The gated spectra for the short tape setting (60 s on/60 s) is shown as the orange line, while the gated long tape cycle (30 min on/30 min off) is shown in solid purple line. The common gate applied was for both fibers to have $E_{fiber} > 70$ [a.u]. The short tape was gated on 3.5s $< t <$ 60s, while the long tape cycle had the gate of $t >$ 1900s.

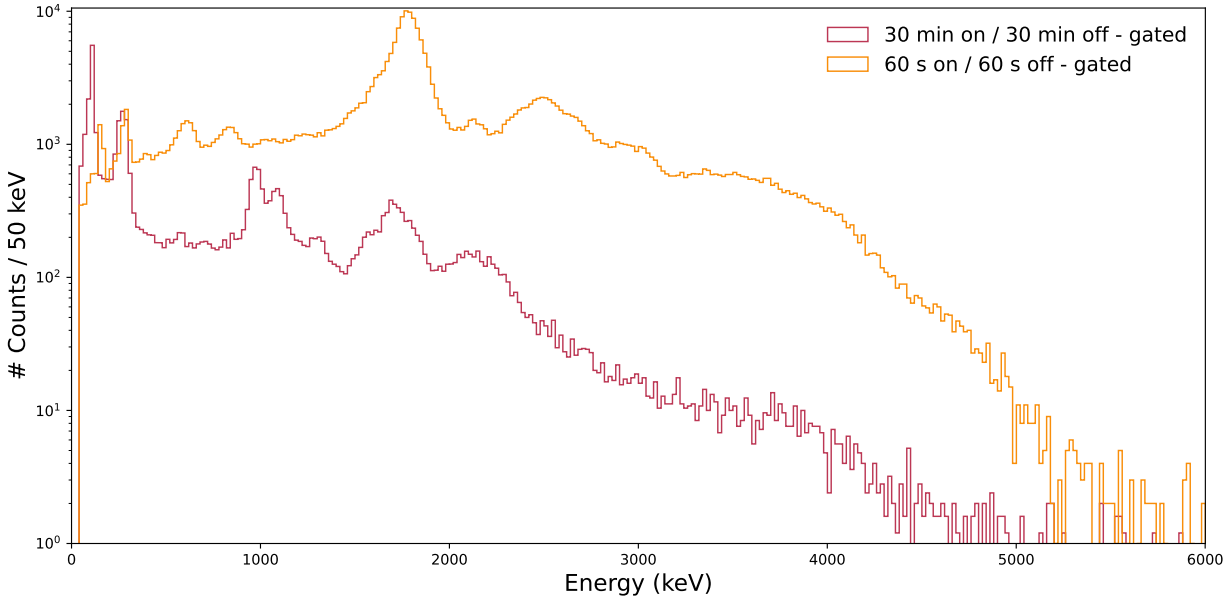

Figure 5.11 TAS comparison for the gated spectra from the two tape settings for A=152. The gated spectra for the short tape setting is shown as the orange line, while the gated long tape cycle is shown in solid purple line. The common gate applied was for both fibers to have $E_{fiber} > 70$ [a.u]. The short tape was gated on 3.5s $< t <$ 60s, while the long tape cycle had the gate of $t >$ 1900s.

contribution to the short tape cycle. The final raw matrix gated from the short tape setting was made with a gate on the beam-on setting with the events happening between 3.5 – 60 s, shown in Figure 5.12.

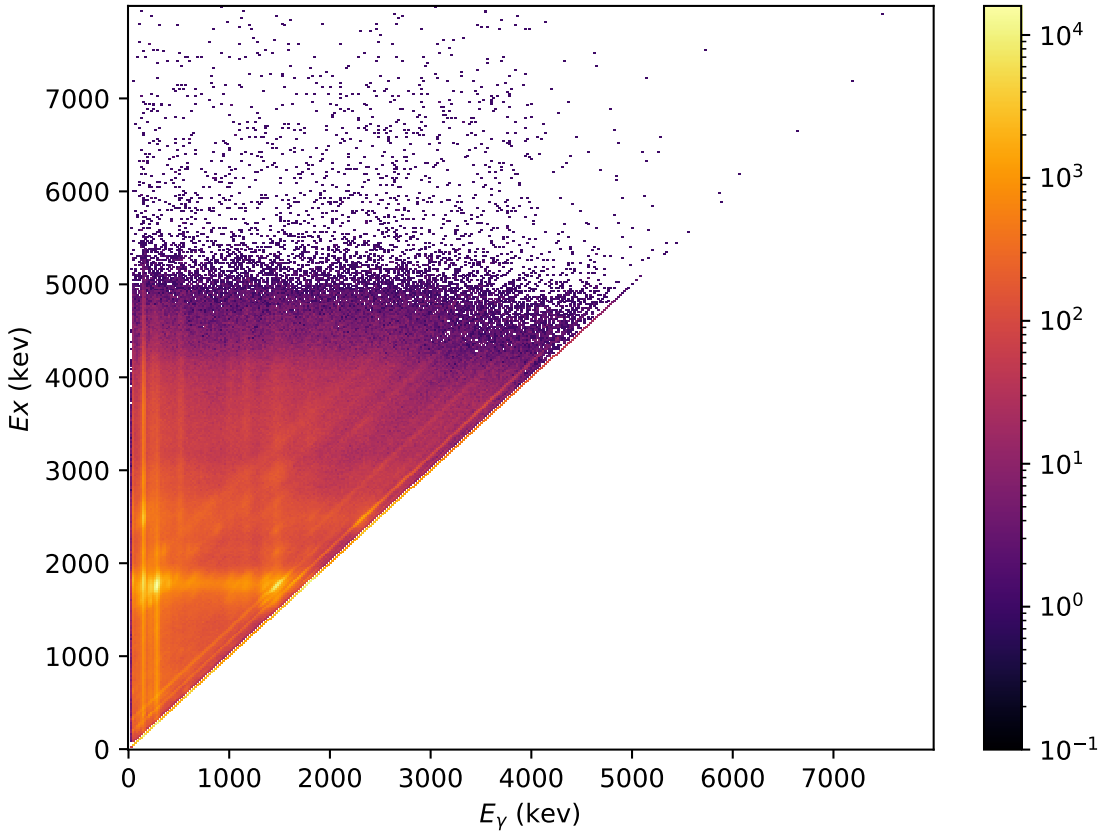

Figure 5.12 The raw matrix for the population of ^{152}Nd from the parent ^{152}Pr. This matrix has been gated on the time from the short tape cycle, as described in Chapter 5.

5.2 A = 154

For studying the neutron-capture cross section on ^{154}Nd, we need to populate the ^{154}Nd in an excited state from the β decay from ^{154}Pr. The beam rates can be seen in Table 5.2. From the rates we see that the isotope of interest, ^{154}Pr, is the least abundant in the beam, which makes proper background subtraction essential to create the particle-γ matrix needed for the β-Oslo method.

For the A = 154 case, the decay chain stops at ^{154}Sm, as this is the first stable nucleus in the decay chain. The decay chain is detailed in Equation (5.2), and we can see the beam properties

Table 5.2 Beam rates for Argonne National Laboratory's CARIBU for isobars A = 154, from Ref. [46]. Half-lives are from Ref. [60].The rates are proportional to the fission yields from ^{252}Ca.

Beam	Rate (pps)	% beam	Half-life	Q_{β^-} (keV)
^{154}Pr	$7.0{\cdot}10^2$	5.2	2.3 s	7720
^{154}Nd	$5.5{\cdot}10^3$	40.7	25.9 s	2680
^{154}Pm	$3.4{\cdot}10^3$	27.2	2.68 min	4180
^{154m}Pm	$3.9{\cdot}10^3$	28.9	1.7 min	4378

along with the half-lives of the A=154 isobars in Table 5.2.

$$^{154}\text{Ce} \rightarrow {}^{154}\text{Pr} \rightarrow {}^{154}\text{Nd} \rightarrow {}^{154}\text{Pm} \rightarrow {}^{154}\text{Sm} \tag{5.2}$$

For the A = 154 isobars, we ran with two different tape settings:

1. 5 s beam on, 1 s beam off – for isotope of interest

2. 300 s beam on, 300 s beam off – for background subtraction

The activity percentage of the A = 154 tape settings are shown for 5 s on, 1 s off in Figure 5.13, and for the 300 s on, 300 s off in Figure 5.16.

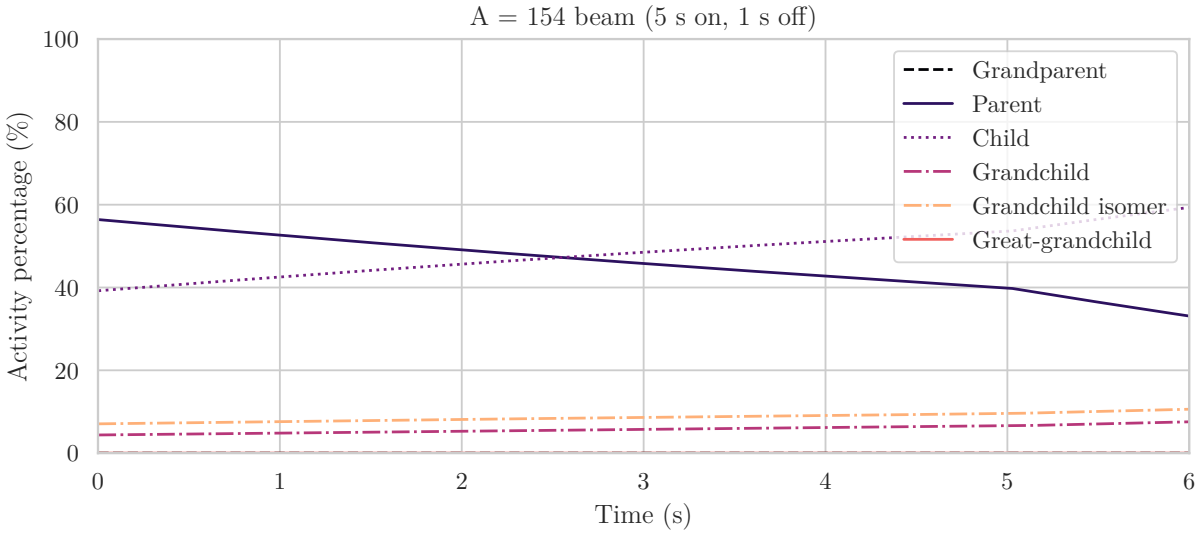

Figure 5.13 Assuming beam make-up is as referenced in Table 5.2, the calculated activity percentage is as plotted in the activity profile, for the 5 s on, 1 s off beam setting.

For the shorter tape setting, we can see in the activity and in the decay plots, Figures 5.13 and 5.14, that it is dominated by the parent, ^{154}Pr, and the child, ^{154}Nd, for the whole cycle. The

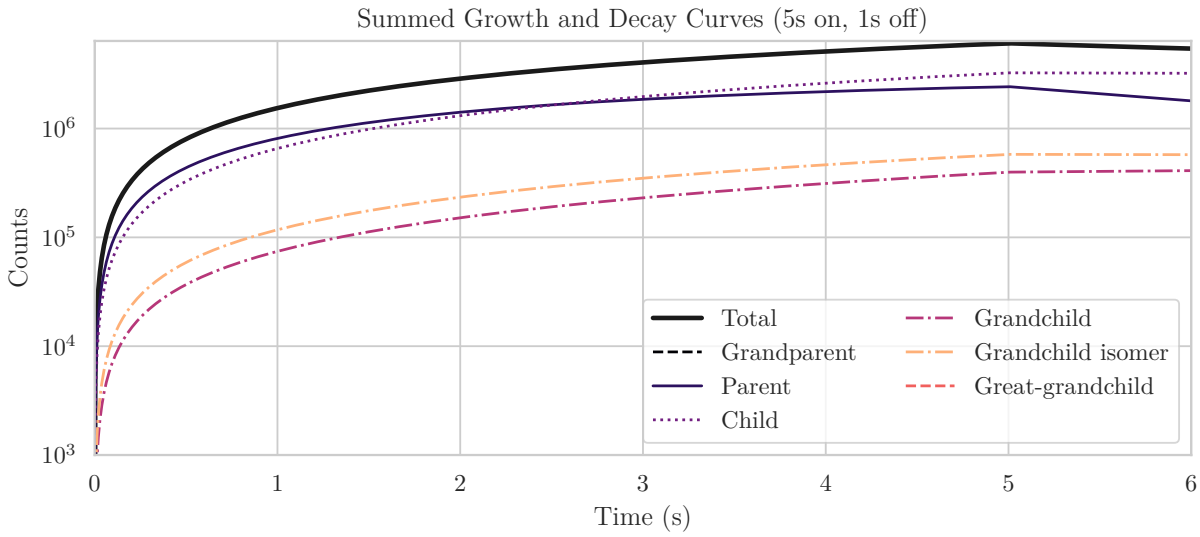

Figure 5.14 Assuming beam make-up is as referenced in Table 5.2, the summed decay curve will be as plotted in the activity profile, for the 5 s on, 1 s off beam setting.

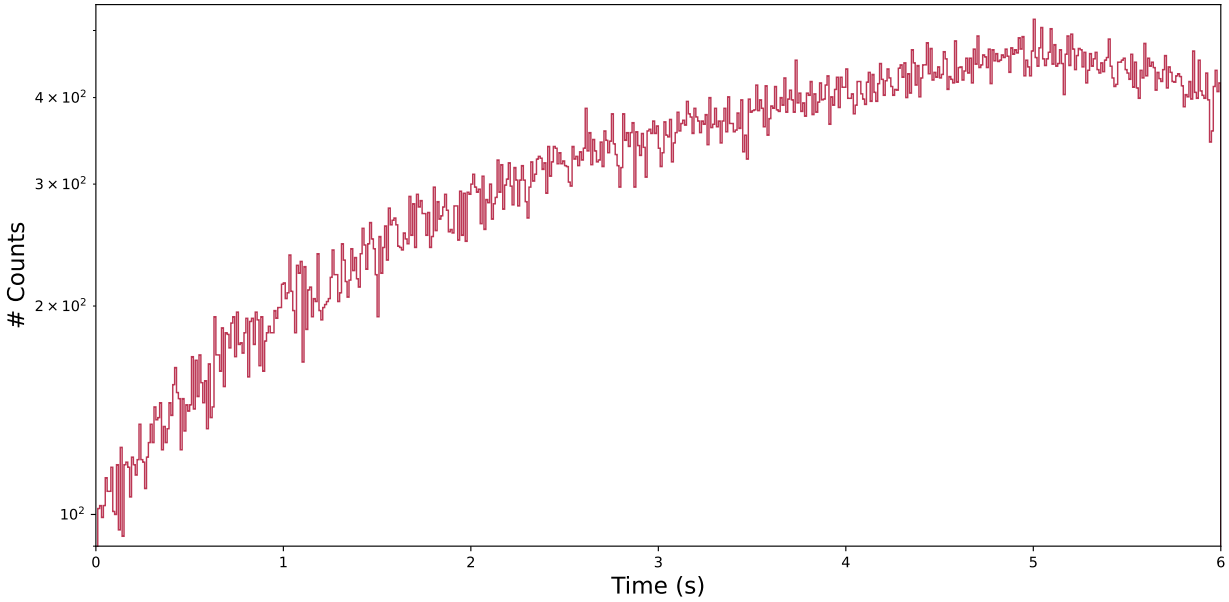

Figure 5.15 Decay curve for the A=154 5 s on, 1 s off, which was used to focus on the nucleus of interest, ^{154}Pr.

contamination from the grandchild and beyond is small, and was ignored in this case. This setting was used for ^{154}Pr, after the ^{154}Nd contamination is subtracted. The experimental decay curve from the 5 s on, 1 s off data is shown for comparison in Figure 5.15.

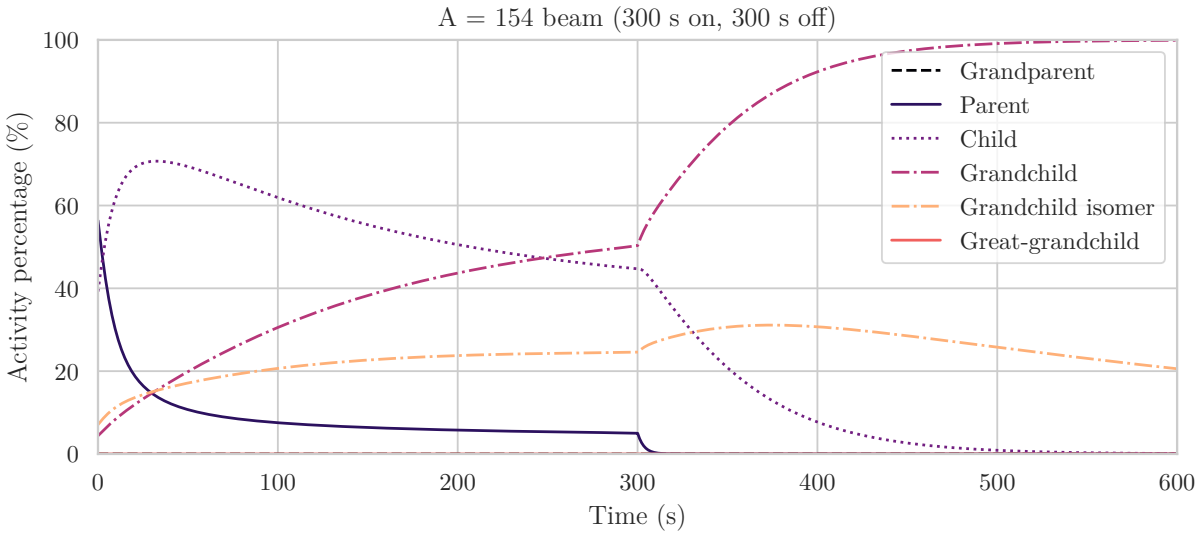

Figure 5.16 Assuming beam make-up is as referenced in Table 5.2, the activity percentage is plotted in the activity profile, for the 300 s on, 300 s off beam setting for background subtraction.

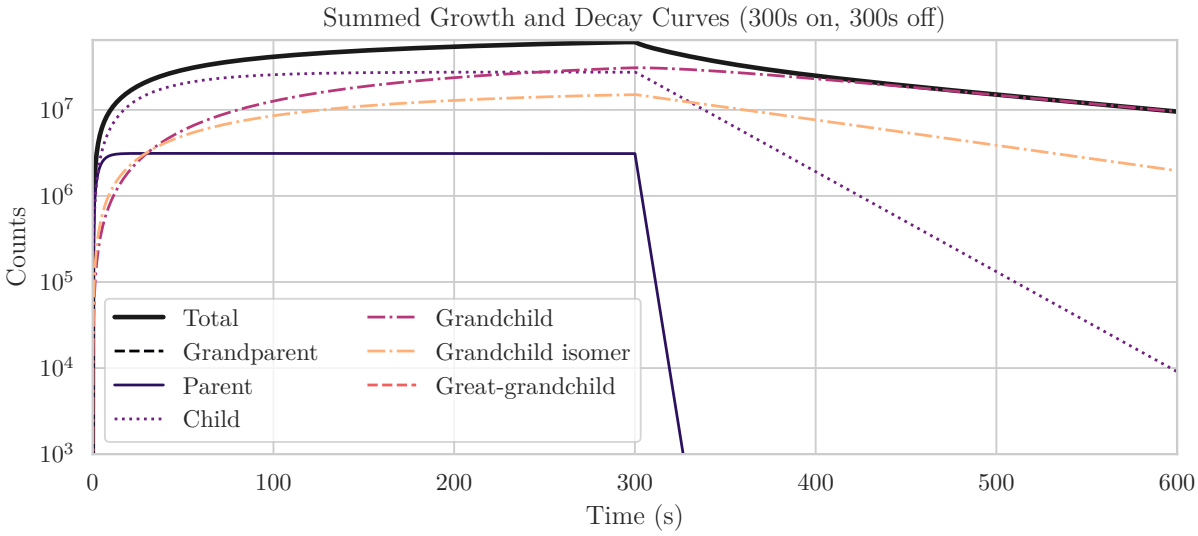

Figure 5.17 Assuming beam make-up is as referenced in Table 5.2, the summed decay curve will be as plotted in the activity profile, for the 300 s on, 300 s off beam setting.

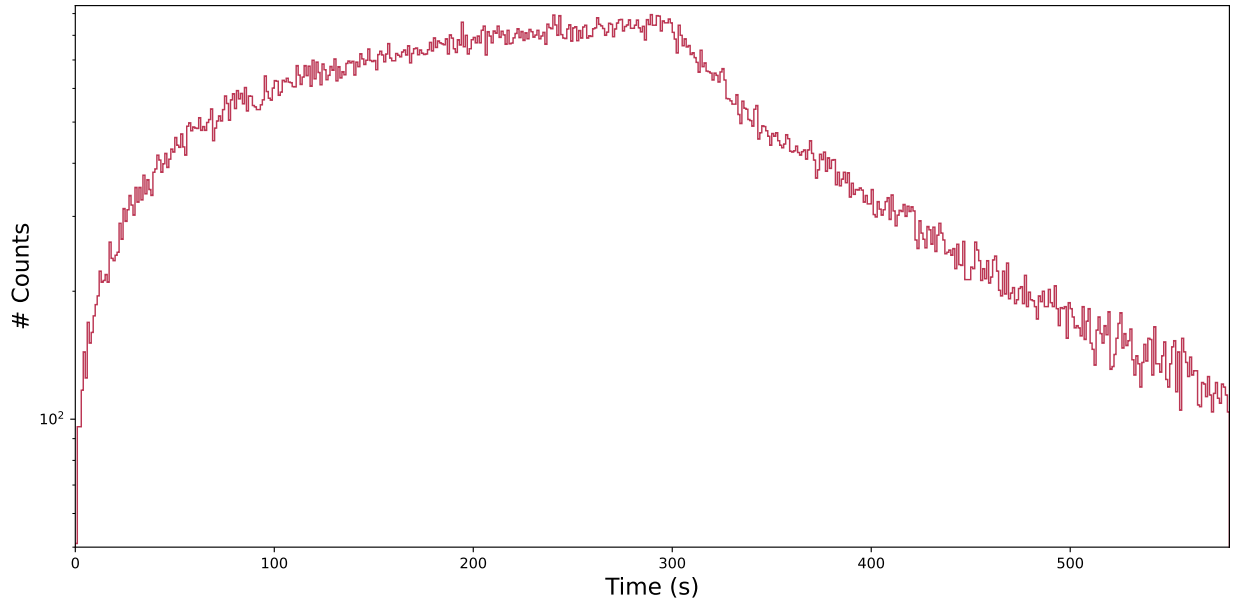

Figure 5.18 Experiment decay curve for the A=154 300 s on, 300 s off beam setting, which was used for background subtraction.

For the longer tape setting, we can see in the activity plot in Figure 5.16 that the first 100 s are largely dominated by ^{154}Nd. After the 400 s mark the grandchild and its isomer are dominating the decay, due to the buildup of the ^{154}Nd seen in the decay plot in Figure 5.17. The decay curve from one of the runs from the 30 minutes on, 30 minutes off beam setting is shown in Figure 5.18.

The TAS vs time is shown in Figure 5.19, with the SoS vs time in Figure 5.20. For the longer tape setting, we can see how some states continue to be populated and decay, even much later than the decay from our nucleus of interest, which disappears shortly after the beam is turned off.

5.2.1 A=154 Background Subtraction

To isolate the parent nucleus in the A=154 beam setting, we needed to be able to isolate the ^{154}Pr decay from the rest of the decays. From the shorter tape cycle, the contamination was from the child nucleus, ^{154}Nd. The first step was then to isolate spectra which included just the child decay. This lead to a similar issue of contamination from the grandchild being present. Thus, the spectra for the grandchild had to be isolated first from the 300 s on, 300 s off beam setting. The spectra we needed to use were the TAS, the SoS and TAS with multiplicity =1, denoted as $\text{TAS}_{\text{mult=1}}$. In these spectra there was a prominent peak from the decay of the β decay of ^{154}Nd to ^{154}Pm at 0.850 MeV

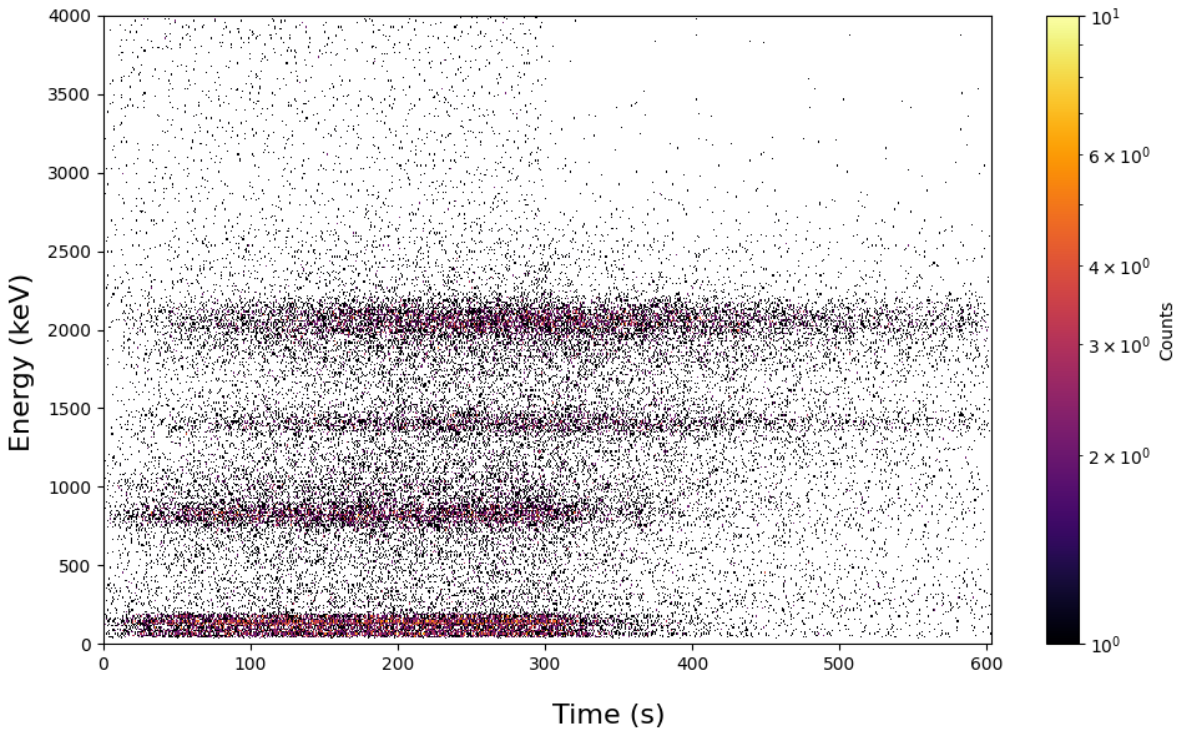

Figure 5.19 TAS v decay for A=154 for 300 s on, 300 s off beam setting. It can be seen that there is a strong population above $E_x \approx 2$ MeV which continues after the beam was turned off which is due to the ^{154}Pm β decay.

[60], as can be seen in Figure 5.19.

A time gate in the 450 s - 600 s interval was applied to isolate the grandchild contribution of ^{154}Pm decaying to ^{154}Sm. From this decay, we expected to see a characteristic peak from the strongly populated state at 1.986 MeV [60]. With this gate applied to the TAS, SoS and $\text{TAS}_{\text{mult=1}}$, the grandchild contribution is shown purple, with the fit to the in the dashed-dotted purple line in Figures 5.21 and 5.22. This gate is denoted as the "second" gate. Similarly, the contamination in what we isolated on as the child decay, a gate on 50 s - 100 s was applied the TAS, SoS and $\text{TAS}_{\text{mult=1}}$, shown the solid gray line. This was done with a gate from 50 s - 100 s on the 300 s on, 300 off cycle. With this gate, we performed a peak fit at the 2 MeV peak with a Gaussian function and a linear background, shown in the top part of Figures 5.21 and 5.22 for the TAS. The scaling factor was then determined from the integral of the peak minus the linear background. The total fits are shown in the dashed black line for the "first" gate, and dashed-dotted purple line for the "second" gate, with the linear background shown in the same color scheme in dotted lines. The

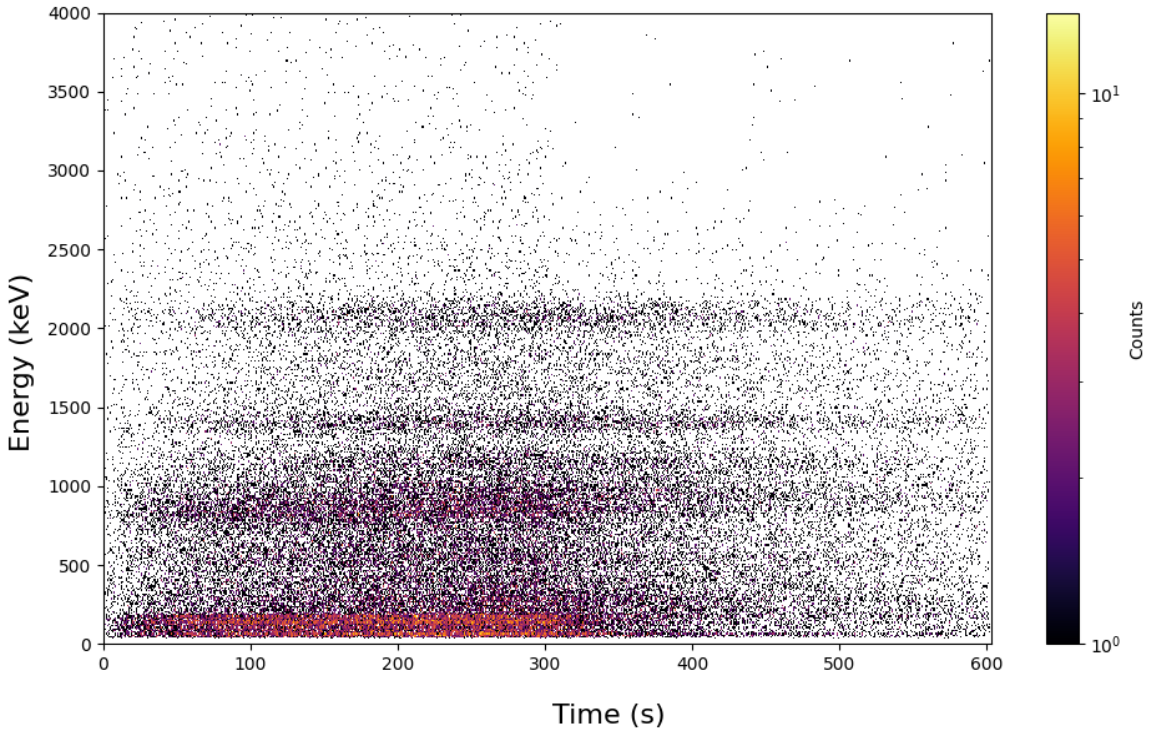

Figure 5.20 SoS vs decay for A=154 300 s on, 300 s off. Like the TAS spectra, there is a decay where $E_\gamma \approx 2$ MeV which continues after the beam was turned off due to the ^{154}Pm decay . The contribution at $E_x = 0.85$ MeV is from the β decay of ^{154}Nd.

second gate was from 450 s - 600 s.

The resulting subtracted spectra for the TAS, the TAS for multiplicity = 1 ($TAS_{mult=1}$) and the sum of segments (SoS) are shown in the dashed red line in Figure 5.21. Figure 5.22 shows the same spectra focusing around the 2-MeV peak used in the sub.

Afterwards, in the same manner, the peak at 0.85 MeV was used to find the scaling factor. After scaling the background subtraction, the final subtracted spectra for our nucleus of interest is shown in the dashed red line in Figure 5.23, which is from the β decay of ^{154}Pr to ^{154}Nd for the short tape setting, where the background component was isolated from the long tape setting.

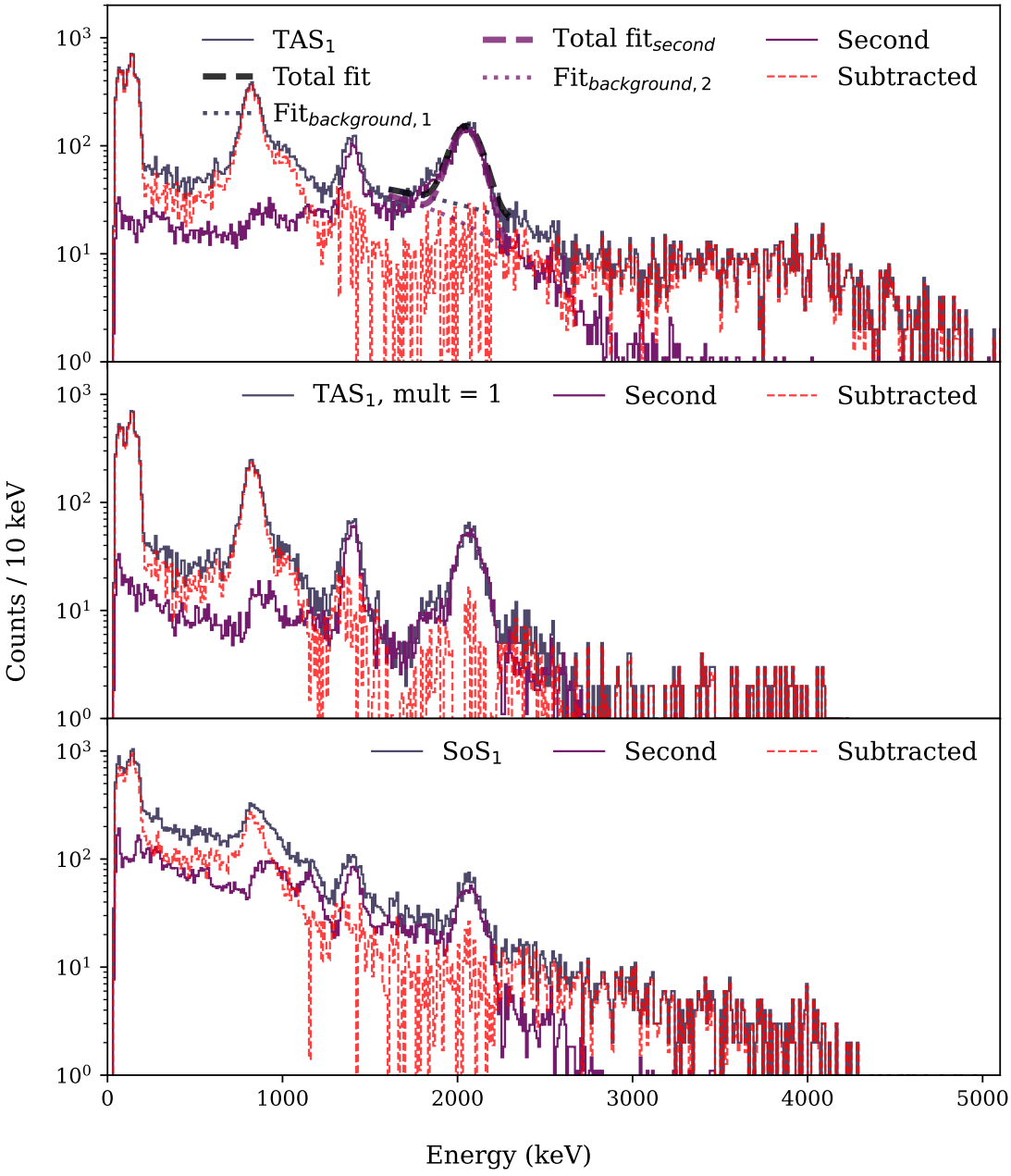

Figure 5.21 Background subtraction for ^{154}Nd, shown in the dashed red line. The gate is from 50-100 s for the one denoted with the subscript (like SoS$_1$) and 450-600 s for the second gate.

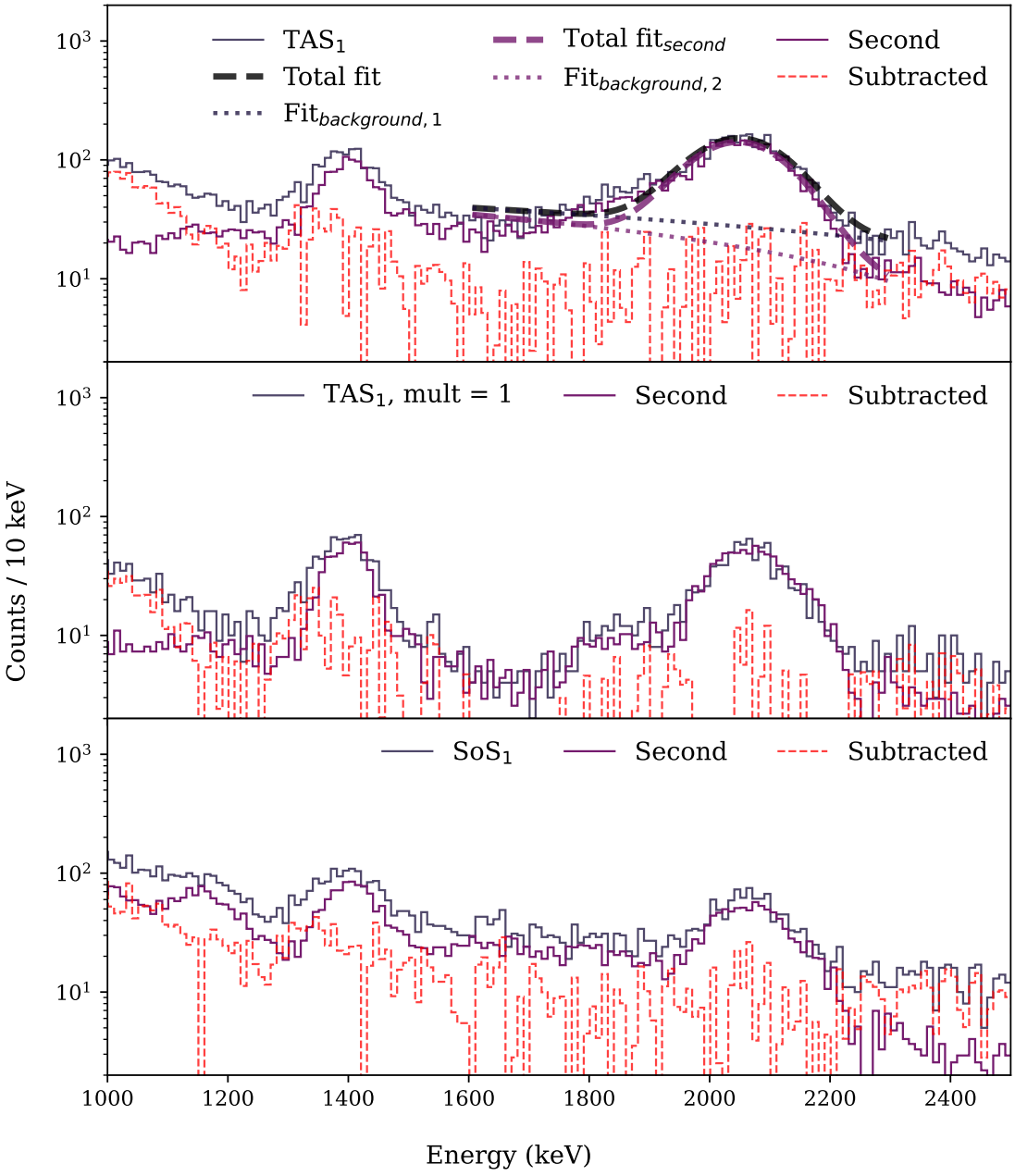

Figure 5.22 Zoomed in on the gated background subtraction for ^{154}Nd. The gate is from 50-100 s for the one one denoted with the subscript (like SoS$_1$) and 450-600 s for the second gate.

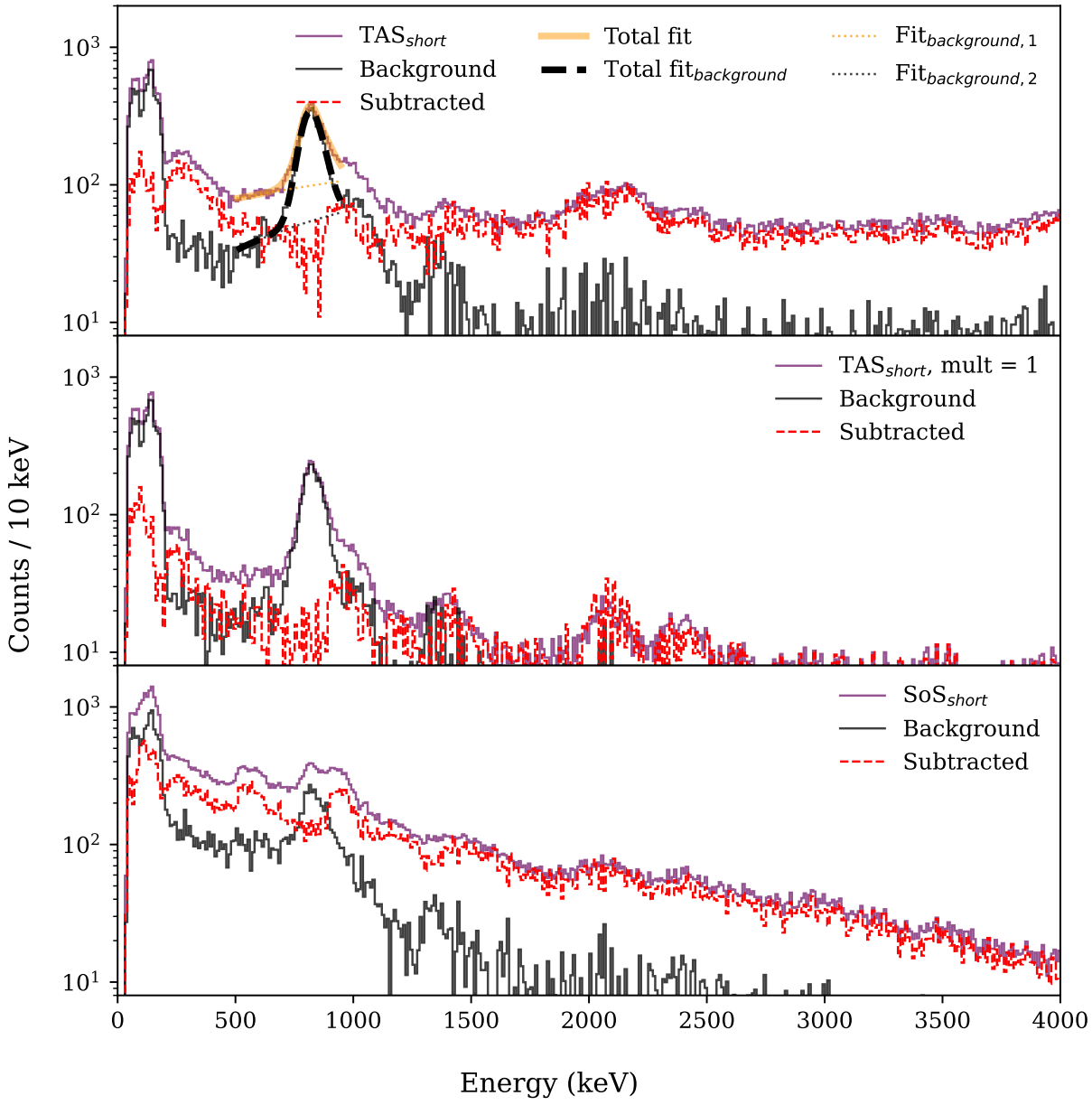

Figure 5.23 The final subtracted spectra for the A=154, shown in dashed red lines, with the scaled background in solid black line. In the top panel, the peak fits used for the background scaling is shown in dashed black lines for the background spectra, and in solid yellow line for the short gate used.

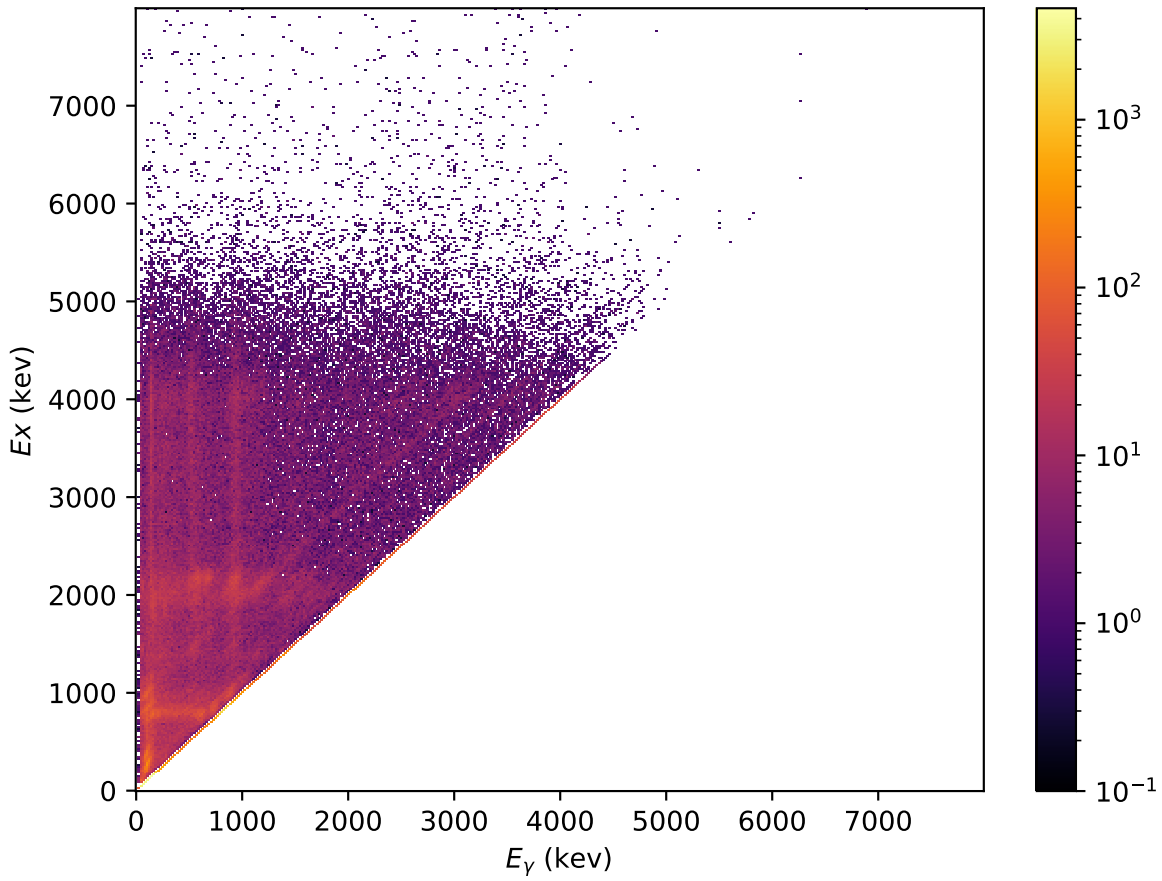

Figure 5.24 The raw matrix for the population of ^{154}Nd from the parent ^{154}Pr. This matrix has been background subtracted.

After subtracting the contributions of the contaminant decays, the isolated decay spectra pf the nuclei of ^{154}Pr were produced. To create the E_x vs E_γ matrix for the Oslo analysis, the same set of scaled background subtractions were performed, with the final raw matrix shown in Figure 5.24.

CHAPTER 6

THE β-OSLO METHOD

6.1 The Oslo method

The Oslo method is a well-established method for extracting statistical properties of nuclei [61]. These statistical properties can be used to constrain cross sections and reaction rates indirectly with Hauser-Feshbach calculations [62]. Neutron-capture cross sections are important for a vast variety of applications, everything from medicine, reactor physics, to understanding nucleosynthesis of heavy elements. For the purposes of this work, we are interested in the application of constraining the neutron-capture cross section relevant to the *i* process, as we wish to understand how the production of europium is affected.

Over the years, there have been many different variations of the Oslo method, which help explore nuclei not easily accessible for direct measurements of neutron capture reactions. These nuclei can be hard to work with either because they are short lived, gaseous, or hard to synthesize. Typical Oslo method experiments are based on producing the compound nucleus with a light beam, and hitting a solid target which produces the desired compound nucleus in an excited state and emitting a charged particle. This can be done via scattering experiments like (p,p'), direct reactions like (p,d) or (d,pγ), as used in [63].

In an attempt to reach unstable nuclei the Oslo method has been applied in inverse kinematics, i.e. the target is a light nucleus, and the beam is a heavy nucleus. This requires a powerful cyclotron or beam facility, as a heavy Z beam is usually desired for the reaction. So far this has been used with radioactive beam at ISOLDE and with noble gases that were previously inaccessible. This has been done for Kr and Xe for instance, [64]–[66]. Recently, the charge-exchange Oslo-method was introduced, which uses charge exchange reactions, where a neutron and a proton switch place during the reaction to create the desired compound nucleus. This method is described by Pathirana *et al.* in Ref. [67].

Last, but not least, there is the β-Oslo method, which was first introduced by Spyrou *et al.* in Ref. [68], which uses β decay to populate the compound of interest. This allows us to push the envelope

of constraining reaction rates, as we can go outside the valley of stability and reach short-lived and exotic nuclei like the ones included in this thesis.

With the Oslo method, one can measure both the nuclear level density and the γ-strength function of a nucleus. The starting point in the Oslo method is a matrix of E_x vs E_γ, which shows particle-γ coincidences. There, we have the individual γ-rays plotted against the excitation energy. To be able to extract the statistical properties, it is critical that enough events are in the statistical region and free of contamination. This statistical region is where we assume no direct population of discrete levels in the compound nucleus, i.e. the excitation energy, E_x is higher than the primary discrete states, and that we are looking at the so-called quasi-continuum, where the levels are close in energy such that we can treat them as statistical quantities. In addition, the γ-decay has to be between these levels, and no strong direct transitions. This statistical region is also referred to as the region-of-interest (ROI), Table 6.1 gives relevant nuclear properties with the limits used for the analysis. The background subtraction was thoroughly described in Chapter 5.

There are four main steps in the Oslo method procedure:

1) Unfold the raw data, taking into account the detector response [69], detailed in Section 6.2.

2) Use the First Generation Method to extract the primary γ-rays [70], as described in Section 6.3.

3) χ^2-minimization to find the functional form of the level density (ρ) and the transmission coefficient, ($\mathcal{T}$), from the primary matrix [61].

4) Normalization to external data to find absolute magnitude and slope of the NLD and γSF.

For ^{152}Nd, the raw matrix is shown in Figure 6.1, and ^{154}Nd, the raw matrix is shown in Figure 6.2. Both of the matrices are presented after background subtraction has been done, as described in Chapter 5.

The first three steps are detailed in the following subsections, while the last step is described in Chapter 7. These steps were applied to the nuclei of interest and we were able to extract the NLD and γSF, which we then used to calculate the neutron-capture cross section and the reaction rate for ^{151,153}Nd(n,γ)^{152,154}Nd.

For ^{152}Nd, in Figure 6.1 one can observe a strong feeding at E_x = 1.8 MeV due to a large β-decay intensity which populated the 1827 keV level with $J = (3^+)$. For both matrices, there are diagonal lines resulting either from the electrons interacting in the detector or from direct γ feeding into discrete levels.

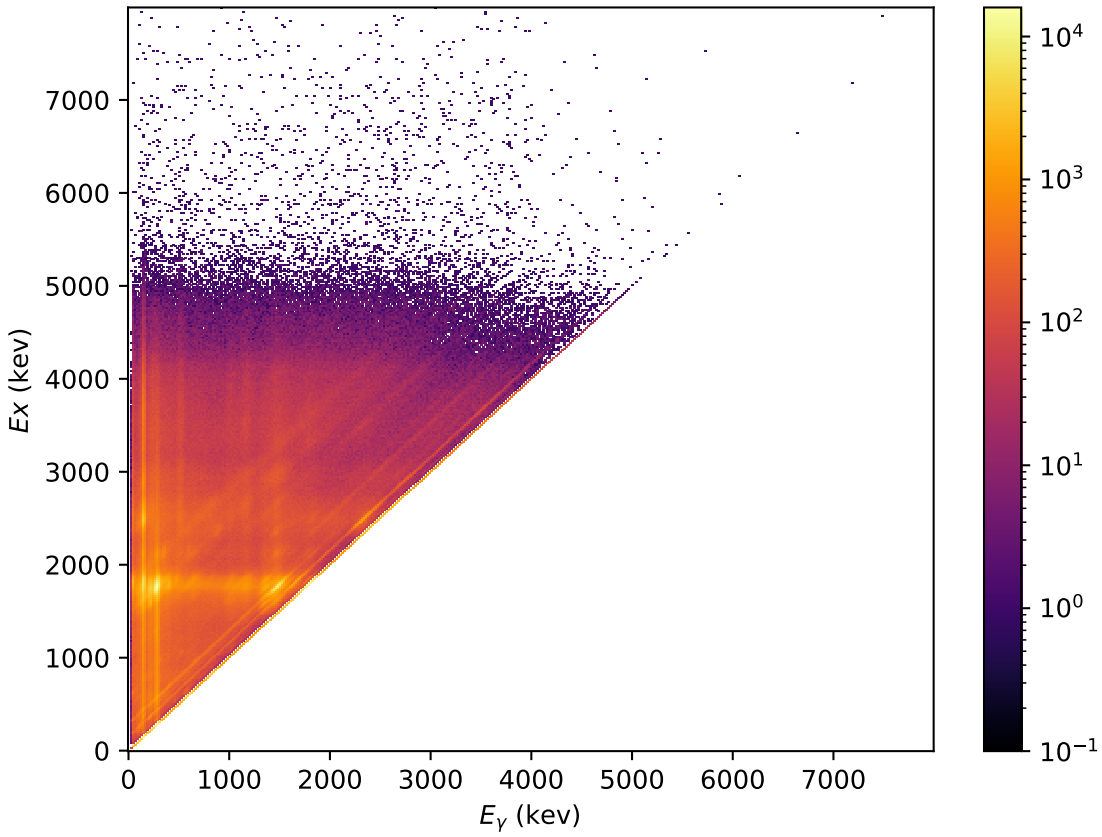

Figure 6.1 The raw matrix for the population of ^{152}Nd from the parent ^{152}Pr. This matrix has been background subtracted, as described in Chapter 5.

6.2 Unfolding

The first step of the Oslo method is the unfolding of the raw E_x−E_γ matrix to remove the detector response from the matrix. This method used to unfold the continuum of γ-ray spectra was first described in [69], and involves an iterative procedure. This is to account for any detector response that affect the spectra. In the case of β-Oslo experiments done with a total absorption spectrometer (TAS) like SuN, this is not only done for the detector response of the E_γ to individual γ rays, but also for the total excitation energy as well [68]. Due to the nature of the TAS, this is

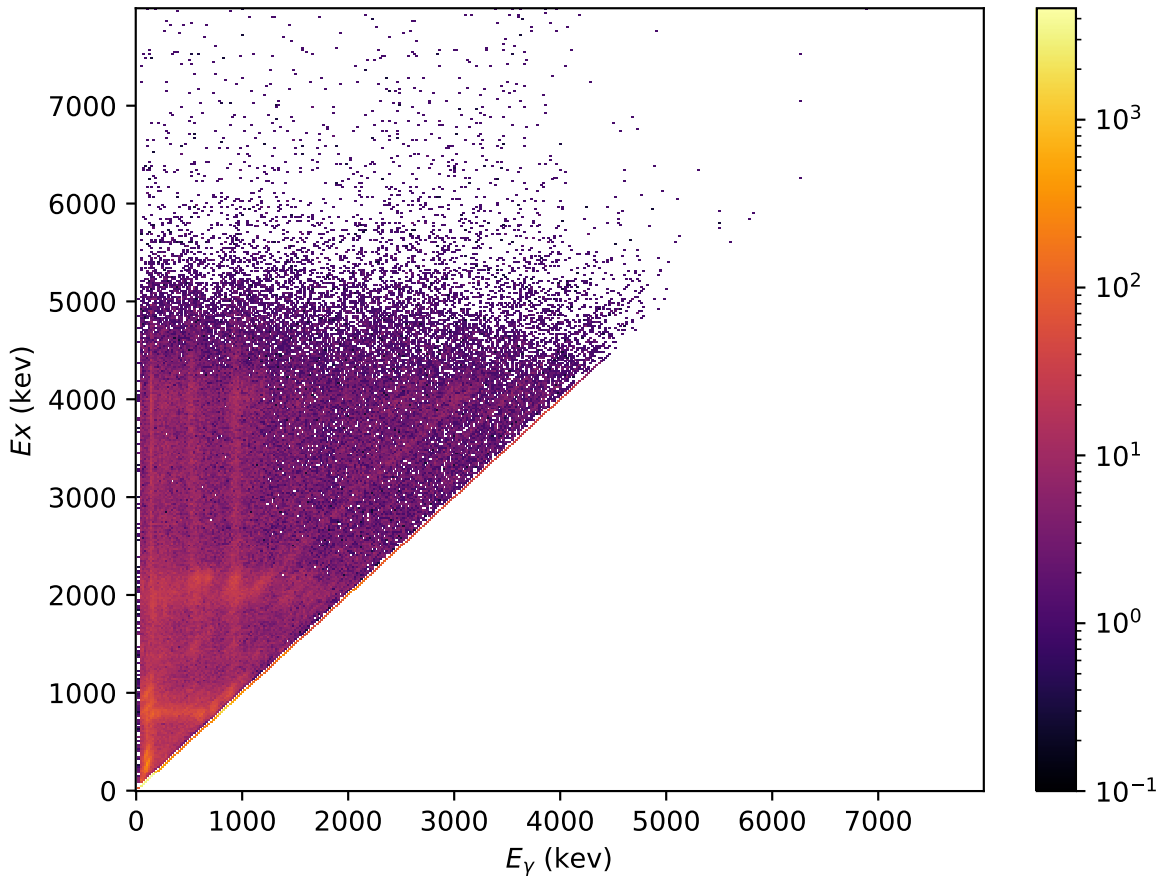

Figure 6.2 The raw matrix for the population of ^{154}Nd from the parent ^{154}Pr. This matrix has been background subtracted, as described in Chapter 5.

due to the fact that the excitation energy is the summation of the detected γ rays in the detector medium. To account for this, the unfolding procedure is done in two steps, first on the x-axis for the γ-ray energy, then on the y-axis for the excitation energy. If unfolded in the opposite order, the excitation energy unfolding can cause γs to change excitation energy, which will then in turn change the unfolding of the x-axis, as this is dependent on the excitation energy. With the former order, there should be minimal issues with the γ-ray unfolding affecting the excitation energy unfolding. Ideally, both axis should be unfolded simultaneously as they are correlated, however, this procedure is under development, and is beyond the scope of this thesis. On a general basis, compression of spectra from the raw matrix is used, with a much larger bin width on the y-axis than the x-axis, due to the relative sensitivity of the γ-ray unfold.

6.2.1 γ-ray unfolding

The response matrix was originally presented in Liddick *et al.* [71], and was used for the unfolding in the present work. This is based on Geant4 [72]–[74] simulations of the detector response of the SuN detector. We assumed multiplicity based unfolding, and that the captured γ-rays can be used to find the total excitation energy with the unfolding, on account of it being a TAS detector. Additionally, the detector efficiency was assumed to be 100% above the 40 keV threshold, since this was set with a ^{241}Am source before the experiment, which was described in Chapter 4. After the data collection was completed, it was sorted with a hard threshold of 40 keV.

The response matrix for the SuN detector can be seen in Figure 6.3. At 511 keV, there is a clear peak from the annihilation, and on the diagonal, clear lines are seen indicating the high energy electrons interacting with the detector.

6.2.2 Excitation energy unfolding

For TAS based experiments, where the excitation energy depends on the measured γ rays, the response of the excitation energy also needs to be adjusted, as first published in [75]. For the response function, we chose the one for β^- decay which is appropriate, which depends on the Q-value of the parent. An input for this unfolding is the γ-ray multiplicity of the populated cascade in the compound nucleus. A general guide is that higher Q-value can increase the number of γ rays needed to reach the ground state, along with the magnitude of the spin of the parent compared to the ground state of the child nucleus. Due to the preference of low multipole transitions in γ rays, large differences in J_i and J_f will require more γ rays on average. For the cases of child nuclei that are even-even, this is more prevalent, since the ground state is 0^+, while the parent in question will then be an odd-odd nucleus, with potentially a higher spin, which can give a high difference in the range of spins for J_i and J_f. Looking at known levels, the average segment hit in SuN, and taking into account the γ decay intensity can give researchers insight into the true γ-ray multiplicity.

A more practical way of doing this is to first do the x-axis unfolding of the γ rays to restore the full energy peaks. Through this process, the multiplicity is estimated for each the excitation energy that can then be used to unfold the y–axis, followed by the first-generation method. This

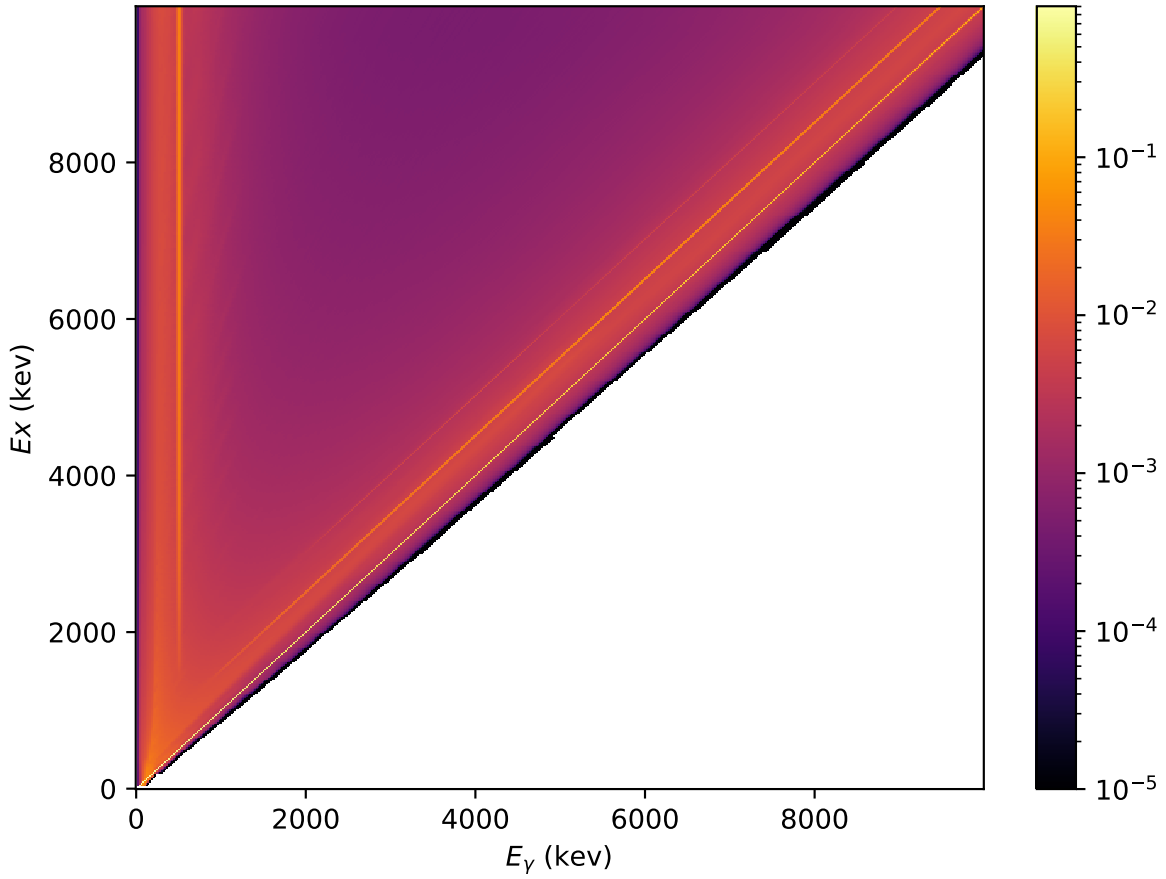

Figure 6.3 The response matrix for SuN for γ rays. This is simulated with Geant4 following the resolution of the SuN detector.

process introduces uncertainty into the unfolded spectra. In the case where the β-decay feeding intensity I_β was measured, this could be used to deduce the true γ-ray multiplicity in the cascade. This would only be possible if the I_β is measured using a TAS, as this would not cause issues such as the pandemonium effect, as described in Chapter 2. Fortunately, as any TAS measurement of the β-decay such as those needed for the β-Oslo method, can also be used for this β-feeding measurement if the background from other events in the decay chain can be subtracted or avoided. This could be interesting to investigate in the cases where J_i and J_f are quite different, as this would have a greater impact on the unfolding and the resulting primary γ-ray matrix, it is however beyond the scope of the present work.

A source of uncertainty in the excitation energy unfolding is the dependence on γ-ray multiplicity

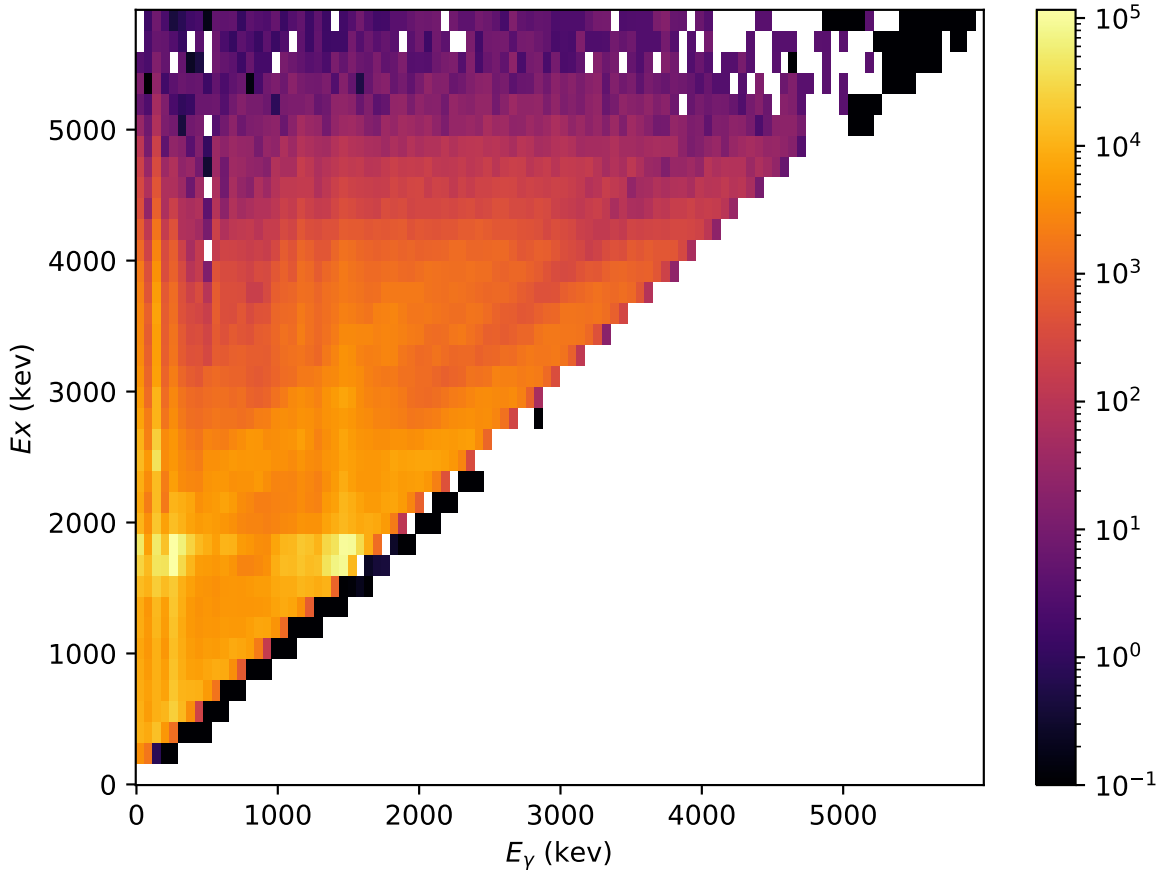

Figure 6.4 The unfolded matrix for ^{152}Nd on the x-axis, taking into account the γ-ray response of the SuN matrix.

in the process. Most of the time, we would not know the true γ-ray multiplicity, instead we rely on a circular information loop of changing the multiplicity from what the first-generation method predicts until it converges. Inherently, this multiplicity is dependent on the feeding into the compound nucleus, and the underlying states as well. If there is an internal conversion electron from a lower-lying level, there is an apparent reduction in the the observed multiplicity.

Since the excitation energy unfolding is dependent on the multiplicity of the γ decays of the compound nucleus and the Q-value of the β decay, each nucleus has a unique response function. The E_x unfolded matrices for ^{152,154}Nd are shown in Figures 6.6 and 6.7.

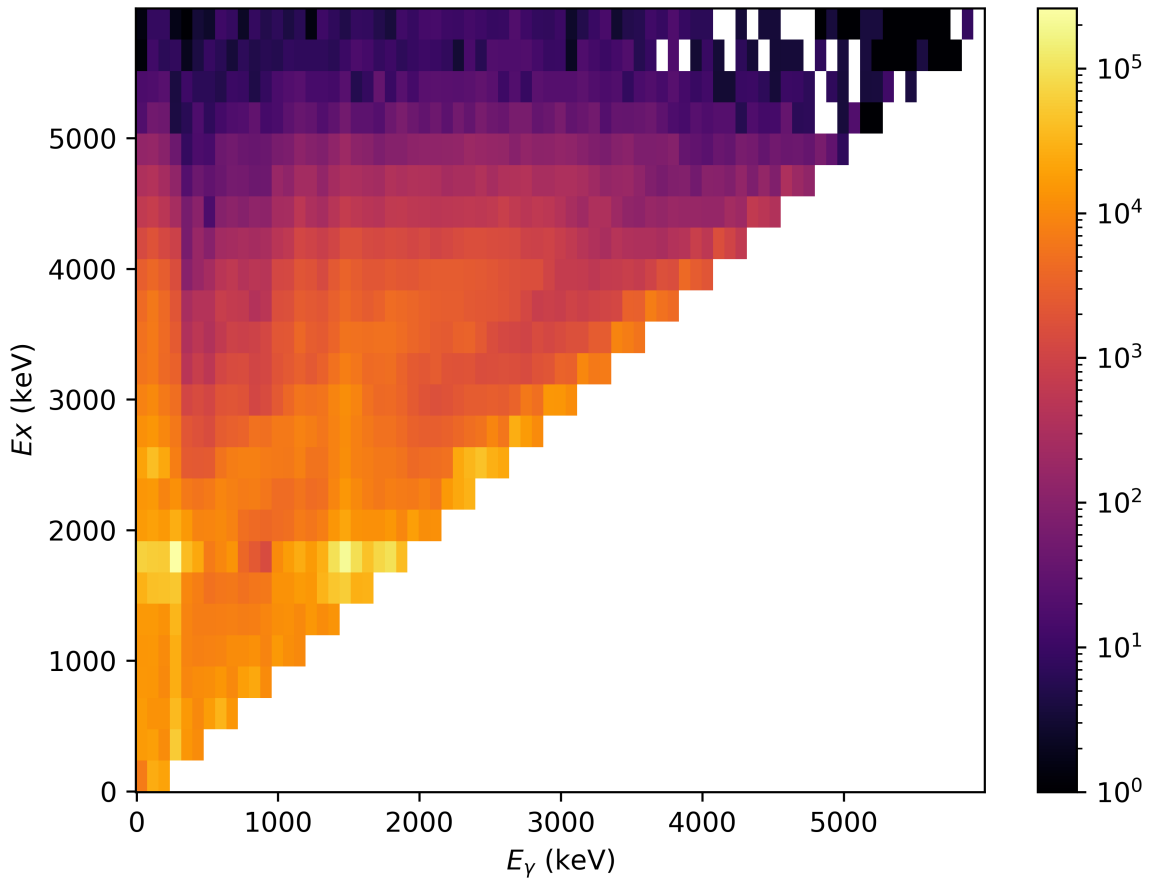

Figure 6.5 The unfolded spectra of ^{154}Nd from the parent ^{154}Pr, which corrects for the response of the detector.

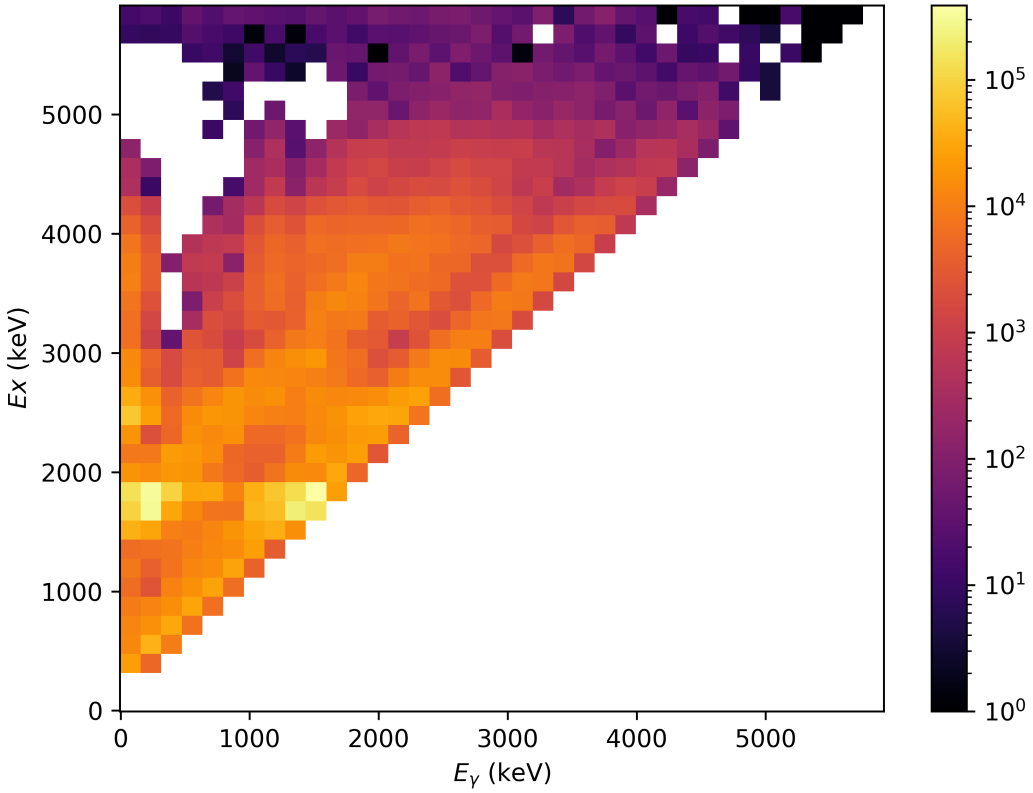

Figure 6.6 The unfolded matrix for ^{152}Nd on the y-axis, taking into account the excitation energy response of the SuN matrix. Here, any nonphysical counts below the diagonal were removed.

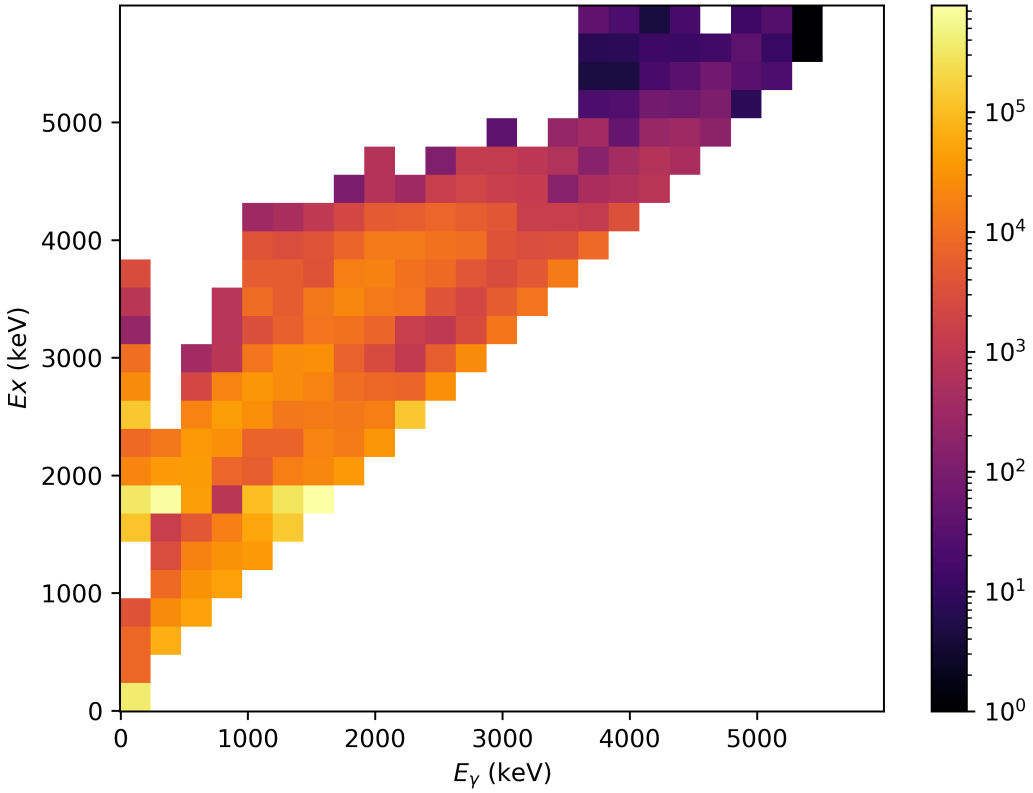

Figure 6.7 The unfolded spectra of ^{154}Nd from the parent ^{154}Pr, which corrects for the response of the detector in both x and y directions.

6.3 First Generation Method

The basic principle for the Oslo method is that the primary matrix P can be related to the nuclear level density, ρ and the transmission coefficient, $\mathcal{T}$, as described in Equation (6.1).

$$P(E_\gamma, E_i) \propto \rho(E_i - E_\gamma)\mathcal{T}(E_i \rightarrow E_f) \tag{6.1}$$

There is an assumption in this equation: it is based on the Brink-Axel hypothesis [76], [77], which assumes that the γSF of a nucleus is only dependent on the energy of the γ decay, E_γ, while it is independent of the spin, parity, and the energy of the initial or final state. The assumptions of this hypothesis have been investigated in relation to the Oslo method, most recently by Markova *et al.* in Ref. [78].

The probability of emitting a primary γ ray is proportional to product of level density, ρ, and transmission coefficient, $\mathcal{T}$, shown as

$$P(E_\gamma, J, \pi) \propto \rho(E_f = E_x - E_\gamma, J, \pi)\mathcal{T}(E_\gamma, J, \pi) \tag{6.2}$$

The first generation matrix, also called the primary matrix can be seen in Figure 6.8 for ^{152}Nd, and in Figure 6.9 for ^{154}Nd.

The first generation method is a way to extract the distribution of the primary γ in the cascade of the compound nucleus after it is populated. The reason this cannot be distinguished in usual circumstances is that if there is more than one γ present in a cascade, the time difference of the emission is on such a short timescale that it is much smaller than the event window. Furthermore, the time resolution of the detectors used is not good enough. If there is only one γ detected, it falls along the $E_x = E_\gamma$ line.

Due to the impossibility of measuring the first γ in the cascade explicitly for Oslo-method experiments, we instead use the first generation method. This is an interative subtraction procedure that subtract lower lying bins for each E_x to find the primary γ. This is described in detail by Guttormsen *et al.* in Ref. [70]. With this primary γ-ray matrix in hand, we have a matrix that is proportional to the nuclear level density and the transmission coefficient, as written in Equation (6.2).

An additional step needed in this analysis is the removal of the diagonal line, where $E_x = E_\gamma - 250$ keV, as this includes internal conversion from the first excited state to the ground state of ^{152}Nd and ^{154}Nd, which then affects the extraction of the functional form of the level density and transmission coefficient from the first generation matrix if it is included. This is only necessary in cases where either long-lived isomers are present or if a large amount of internal conversions present.

Table 6.1 Region of interest and nuclear properties for the Oslo analysis on ^{152}Nd and ^{154}Nd, and the reference is given in the nucleus column. S_n is the neutron separation energy of the compound nucleus, and Q_β is the $Q-$value of the β^- decay populating that compound nucleus from the parents, ^{152,154}Pr.

Nucleus	S_n (MeV)	Q_β (MeV)	E_i (MeV)	$E_\gamma(MeV)$
^{152}Nd [59]	7.278(24)	6.39(3)	2.4	1.8
^{154}Nd [60]	6.321(3)	7.72(10)	2.1	3.2

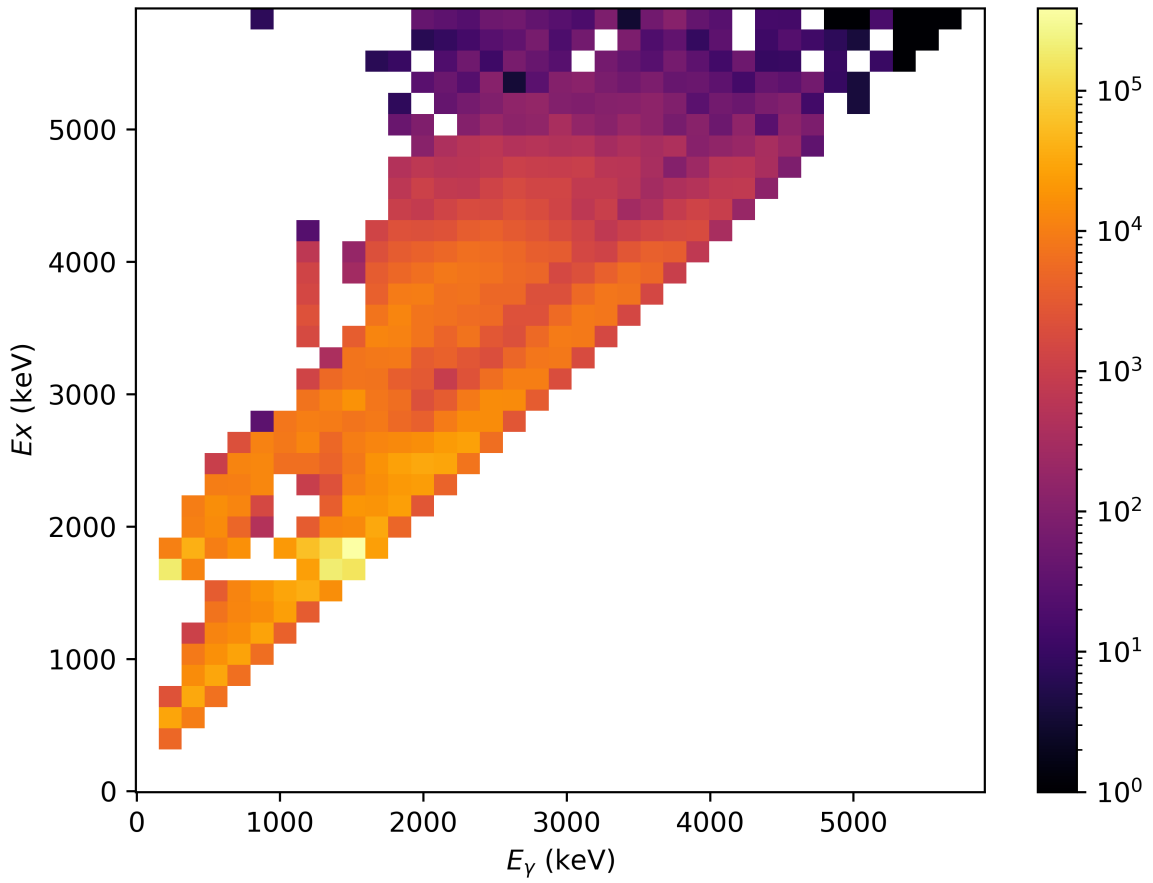

Figure 6.8 The primary matrix for ^{152}Nd, which shows the first γs emitted as a function of excitation energy of the compound nucleus.

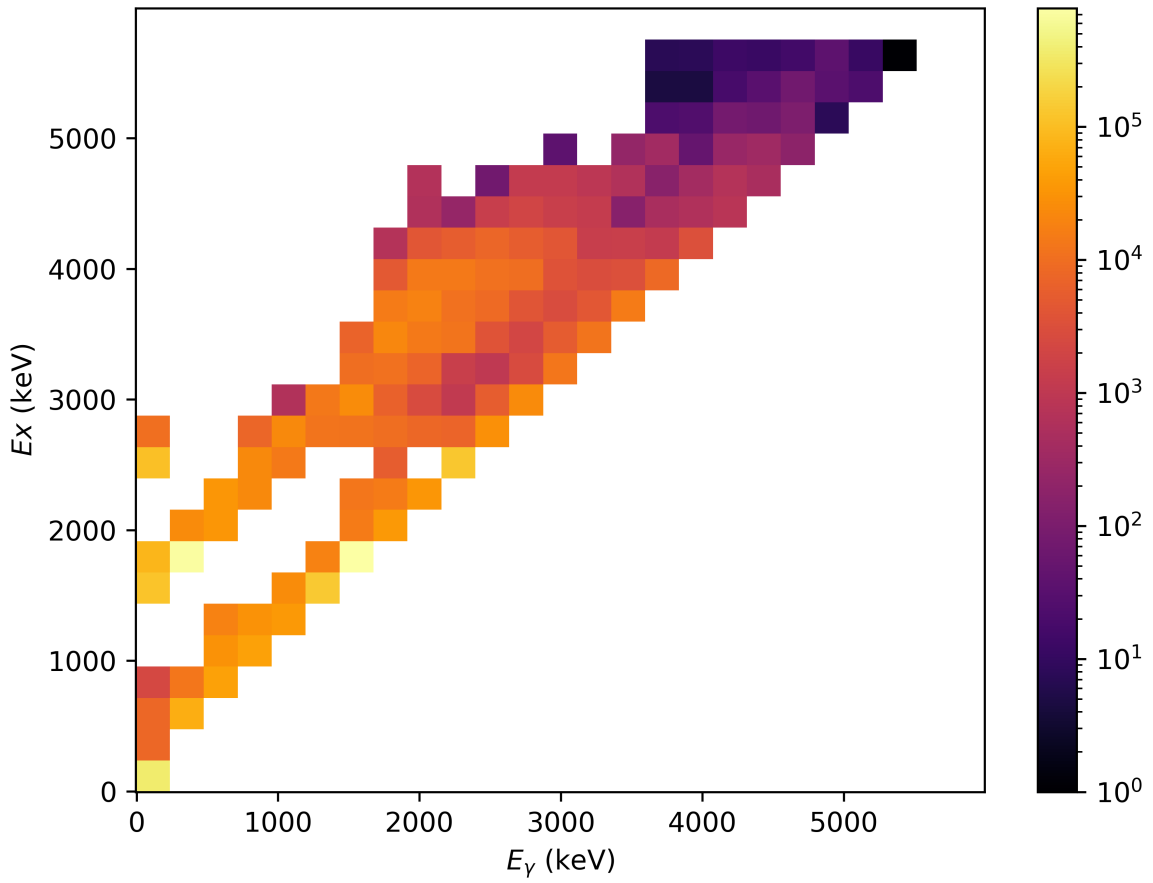

Figure 6.9 The primary matrix for ^{154}Nd, which shows the first γs emitted as a function of excitation energy of the compound nucleus.

6.4 Extracting functional forms of ρ and $\mathcal{T}$

In the Oslo method, the functional forms of the level density ρ and transmission coefficient $\mathcal{T}$ from Equation (6.2) is found by a χ^2-minimization of the primary matrix to fit to a theoretical primary matrix, P_{theory}, via:

$$P_{\text{theory}} = \frac{\mathcal{T}(E_\gamma)\rho(E_i - E_\gamma)}{\sum_{E_\gamma=E_\gamma^{min}}^{E_i} \mathcal{T}(E_\gamma)\rho(E_i - E_\gamma)}. \tag{6.3}$$

For each excitation energy, E_i, the matrix is normalized to unity which leads to Equation (6.4) for these functional forms of ρ and $\mathcal{T}$, which needs to be normalized to find a physical solution.

$$\tilde{\rho}(E_f, J, \pi) = Ae^{\alpha E_x}\rho(E_x, J, \pi) \tag{6.4}$$

$$\tilde{\mathcal{T}}(E_\gamma) = Be^{\alpha E_\gamma}\mathcal{T}(E_\gamma), \tag{6.5}$$

A is determined by normalization to known discrete levels, B is a coefficient determined from the radiative strength, and α is a common slope parameter typically determined from the average resonance width D_0 if available. However, if external normalization data is unavailable, other methods of normalization have to be used, which for this work is described in detail in Chapter 7.

CHAPTER 7

NORMALIZATION AND FITTING OF STATISTICAL PROPERTIES

7.1 Normalization

A problem that can introduce uncertainties into our results is the lack of external normalization data. This is a concern for exotic nuclei for the Oslo method, as the average resonance spacing (D_0) and the average radiative width $\left(\langle\Gamma_\gamma\rangle\right)$ have not been measured for most exotic nuclei.

When data is lacking, one of the techniques used is inferring the numbers from systematics on stable isotopes in the chain. For Nd isotopes, these normalization parameters are available for all stable isotopes. This allowed us to use the trend to predict a reasonable range for the relevant parameters. If no physical parameters are available, there is a largely model-independent way of constraining the nuclear level density (NLD), by fitting the γSF to another measured γSF from the same chain of isotopes.

This has previously been done for the β-Oslo method by Mücher *et al.* in [79]. The transmission coefficient $\mathcal{T}$ can be transformed via Equation (6.5), where as described earlier $\tilde{\alpha}$ is a common coefficient between the transmission coefficient $\mathcal{T}$ and the nuclear level density ρ. To be able to normalize the Oslo data, the transmission coefficient can be used to normalize the γSF as shown in Equation (2.14). The final B can be determined from theoretical predictions of the average radiative width $\langle\Gamma_\gamma\rangle$, or from calculating it using the D_0, as defined in Equation (7.2), inserted into Equation (7.3). The $\tilde{\alpha}$ is determined from a χ^2 minimization, after adjusting B to the absolute magnitude of the reference γSF. To minimize the difference between the sampled reference γSF and the transformed $\tilde{f}$, using

$$\chi^2 = \left(\frac{y_{ref} - y_{obs}}{\sigma_{obs}}\right)^2. \tag{7.1}$$

To find an appropriate $\tilde{\alpha}$, a fitting algorithm was developed that samples the reference γSF N times, then calculates the χ^2 from Equation (7.1), to the transformed $\tilde{f}$ via Equation (6.5).

Normally, when external data is available, D_0 is used to normalize the NLD at $\rho(S_n)$ due to the

Table 7.1 Target spins, J_t from Ref. [59], [80], [81] and spin ranges J_i from Equation (7.5) and final spins J_f available for ^{151,153}Nd used to calculate the average radiative width.

Nucleus	J_t	J_i	J_f
^{151}Nd	$\frac{3}{2}$	$1, 2$	$0, 1, 2, 3$
^{152}Nd	0	$\frac{1}{2}$	$\frac{1}{2}, \frac{3}{2}$
^{153}Nd	$\left(\frac{3}{2}\right)$	$(1, 2)$	$(0, 1, 2, 3)$

following relation:

$$D_0 = \frac{2\sigma^2}{\rho(S_n)} \left[(J_t + 1) \exp\left(-\frac{(J_t + 1)^2}{2\sigma^2} \right) + J_t \exp\left(-\frac{J_t^2}{2\sigma^2} \right) \right]^{-1}, \tag{7.2}$$

where σ is the spin cut-off parameter as described in Section 2.6.1.1, J_t is the spin of the target, given for ^{151,153}Nd in Table 7.1, and $\rho(S_n)$ is extracted from the experimental data in this case to find the average resonance spacing D_0 for an s-wave neutron capture.

An expression for the average radiative width $\langle \Gamma_{\gamma l}(S_n) \rangle$ is derived by Midtbø *et al.* in Ref. [82]:

$$\begin{aligned} \langle \Gamma_{\gamma l}(S_n) \rangle =& \frac{\sum_{J_i} \rho(S_n, J_i) \langle \Gamma_\gamma(S_n, J_i, \pi_i) \rangle}{\sum_{J_i} \rho(S_n, J_i)} \\ =& \frac{D_l}{2} \int_0^{S_n} dE_\gamma \left[f\left(E_\gamma\right) E_\gamma^3 \rho\left(S_n - E_\gamma\right) \sum_{J_i} \sum_{J_f = |J_i - 1|}^{J_i + 1} g\left(S_n - E_\gamma, J_f\right) \right] \end{aligned} \tag{7.3}$$

$$\left| J_t \pm \frac{1}{2} \pm l \right| \leq J_i \leq J_t + \frac{1}{2} + l, \tag{7.4}$$

In Equation (7.3), J_i are the spins of the residual nucleus and spans the range defined in Equation (7.4), and J_f are the spins accessible through dipole transition, that is $E1$ or $M1$. Since we assume $l = 0$ and that the excitation energy is $E_x \approx S_n$ [82], we can simplify Equation (7.4) to where J_i are the spins of the residual nucleus and spans the range from the target spin J_t:

$$\left| J_t \pm \frac{1}{2} \right| \leq J_i \leq J_t + \frac{1}{2} \tag{7.5}$$

The different J_t and J_i ranges for ^{151,153}Nd is given in Table 7.1. The magnitude of the γSF (B) can then be related to the average radiative width, and the average resonance spacing via:

$$B = \langle \Gamma_\gamma(S_n) \rangle \frac{4\pi}{D_0} \left(\int_0^{S_n} dE_\gamma \mathcal{T}(E_\gamma) \rho\left(S_n - E_\gamma\right) \sum_{J_i} \sum_{J_f = |J_i - 1|}^{J_i + 1} g\left(S_n - E_\gamma, J_f\right) \right)^{-1}. \tag{7.6}$$

7.2 Determining the slope parameter α and magnitude B

To adjust the γSF, $f(E_\gamma)$ to existing data we transform it via α, as written in Equation (7.7)

$$f'(E_\gamma) = B \exp(\alpha E_\gamma) f(E_\gamma), \tag{7.7}$$

which gives us the new $f'(E_\gamma)$. B is the magnitude, E_γ is the γ-ray energy. To find the magnitude B, we utilize fits to experimental data, like GDR ($f_{E1}(E_\gamma)$) or the γSF of the neighboring nucleus ^{151}Nd from M. Guttormsen *et al.* [83]. The extracted slope, α, along with the fitting region, the magnitudes, B of the γSF for the respective fits, are detailed in Table 7.2. Here we can see that the fitting regions are different due to the statistics available in this work and the fluctuations present in this data. For ^{152}Nd, the extracted α is 2.060 ± 0.071, while for ^{154}Nd the extracted $\alpha = 2.012 \pm 0.079$.

Table 7.2 The α slope for the γSF for ^{152}Nd and ^{154}Nd with the uncertainty of the fit, including the magnitude B_{GDR} and B_{Oslo} for the fit to the giant dipole resonance and the Oslo data from M. Guttormsen *et al.*[84] for ^{151}Nd.

Nucleus	α (MeV^{-1})	Fit range GDR (MeV)	B_{GDR} (10^{-9})	χ^2_{GDR}	Fit range Oslo (MeV)	B_{Oslo} (10^{-8})	χ^2_{Oslo}
^{152}Nd	2.060 ± 0.071	3.6 – 4.3	9.55 ± 0.12	0.11	3.4 – 4.3	1.25 ± 0.01	0.14
^{154}Nd	2.012 ± 0.079	2.0 – 4.5	8.29 ± 0.38	3.16	3.4 – 4.5	1.06 ± 0.07	3.44

The extracted γSF for ^{152}Nd and ^{154}Nd are shown Figures 7.1 and 7.2 respectively, with the values included in Tables 7.3 and 7.4. It can be seen that there is good agreement in the fitting region used with the ^{151}Nd data from Guttormsen *et al.* [14] for the ^{152}Nd γSF. In the ^{154}Nd data, there are more fluctuations present.

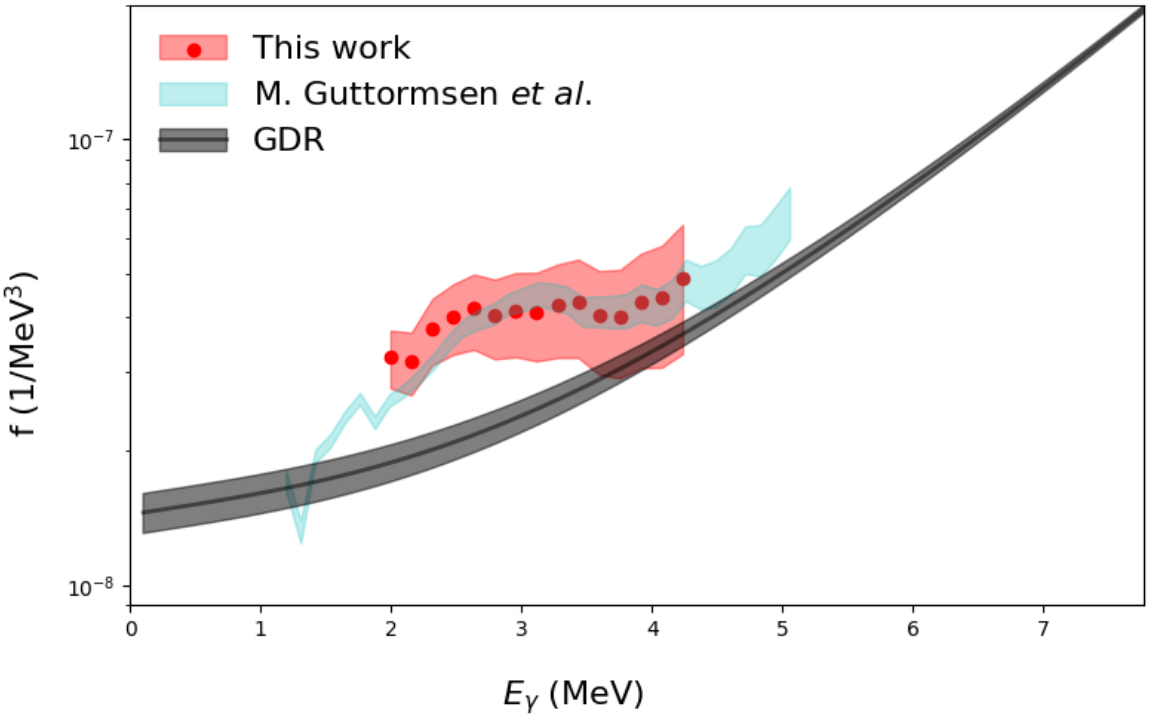

Figure 7.1 The γSF for ^{152}Nd plotted in red together with the ^{151}Nd data from Guttormsen *et al.* [14], and the GDR.

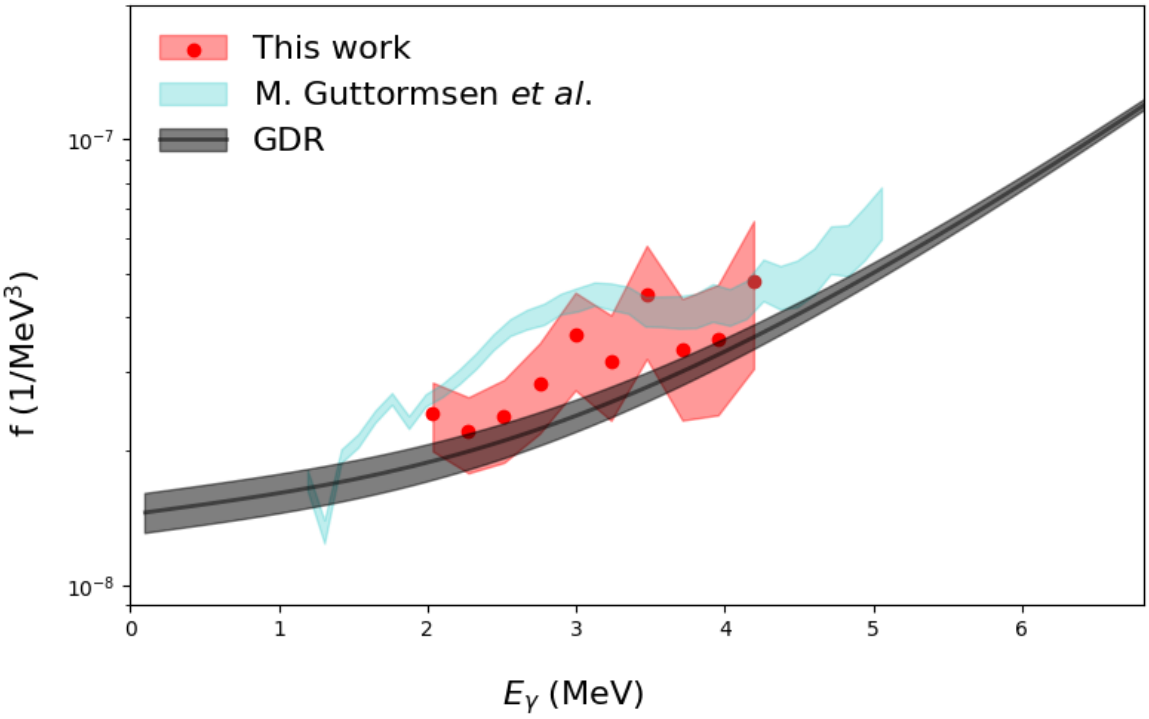

Figure 7.2 The γSF for ^{154}Nd plotted in red together with the ^{151}Nd data from Guttormsen *et al.* [14], and the GDR.

E_γ (MeV)	$f_1\left(E_\gamma\right)\left(10^{-8}\ \mathrm{MeV}^{-3}\right)$	$\sigma_{f_1}\left(10^{-8}\ \mathrm{MeV}^{-3}\right)$
1.995	3.246	4.804
2.155	3.177	0.509
2.315	3.752	0.637
2.475	4.011	0.723
2.635	4.177	0.802
2.795	4.031	0.817
2.955	4.133	0.884
3.115	4.102	0.922
3.275	4.239	1.002
3.435	4.308	1.071
3.595	4.016	1.051
3.755	4.007	1.094
3.915	4.306	1.238
4.075	4.426	1.348
4.235	4.872	1.569

Table 7.3 The values for the ^{152}Nd γSF $\left(f_1\left(E_\gamma\right)\right)$ with the uncertainty (σ_{f_1}).

E_γ (MeV)	$f_1\left(E_\gamma\right)\left(10^{-8}\ \mathrm{MeV}^{-3}\right)$	$\sigma_{f_1}\left(10^{-8}\ \mathrm{MeV}^{-3}\right)$
2.035	2.423	0.425
2.275	2.212	0.428
2.515	2.387	0.503
2.755	2.840	0.651
2.995	3.635	0.898
3.235	3.186	0.846
3.475	4.498	1.278
3.715	3.366	1.022
3.955	3.564	1.157
4.195	4.809	1.751

Table 7.4 The values for the ^{154}Nd γSF $\left(f_1\left(E_\gamma\right)\right)$ with the uncertainty (σ_{f_1}).

7.2.1 Uncertainty propagation

The propagating the uncertainty, $\sigma_{f'}$ is then given as:

$$\sigma_{f'}^2 = \left(\left(\frac{\partial f'}{\partial B}\right)^2 \sigma_B^2 + \left(\frac{\partial f'}{\partial \alpha}\right)^2 \sigma_\alpha^2 + \left(\frac{\partial f'}{\partial f}\right)^2 \sigma_f^2\right) \tag{7.8}$$

$$= \left(\left(\frac{f'}{B}\right)^2 \sigma_B^2 + \left(f' E_\gamma\right)^2 \sigma_\alpha^2 + \left(\frac{f'}{f}\right)^2 \sigma_f^2\right), \tag{7.9}$$

$$\Rightarrow \sigma_{f'} = f' \sqrt{\frac{\sigma_B^2}{B^2} + E_\gamma^2 \sigma_\alpha^2 + \frac{\sigma_f^2}{f^2}}. \tag{7.10}$$

For this extracted α, the uncertainty σ_α takes different fitting regions into account, and variations in the region of interest used from the first-generation matrix. The σ_α was calculated as the weighted standard deviation of all of the aforementioned fits, with the weight, w, being the inverse reduced χ^2, that is $w = 1/\chi^2$. The uncertainty of the slope and the magnitude from the fitting region, along with the extraction region from the `rhosigchi` [85], was then incorporated into the uncertainty bands and propagated throughout the analysis into the γSF and NLD bands, along with the final cross sections.

7.3 Extracting A

In cases of extracting statistical properties using the β-Oslo method, we end up extracting the absolute partial level density, not the total level density. With the partial level density extractions, only some spins are populated, as we are only assuming allowed decays will be populating the compound nucleus. The slope of the partial level density was found by the model-independent method as described in Section 7.1. The magnitude A comes from normalizing to known discrete levels that could be populated via allowed β-decay transitions plus a dipole transition. The magnitude A was found by sampling the level density within the uncertainty that includes the uncertainty of the applied slope α. This is presented in Table 7.5, including the fitting region of the discrete levels used.

The absolute partial LD for ^{152}Nd and ^{154}Nd are shown in Figures 7.3 and 7.4 where the the slope α and the magnitude A have been applied. The values for the NLD for ^{152}Nd and ^{154}Nd are given in Tables 7.6 and 7.7 respectively. Uncertainty was introduced in the analysis by the range of

Table 7.5 The fitting parameters for the magnitude, A, of the partial level density with the fitting range used for the discrete levels.

Child nucleus	Parent nucleus	J^{π}_{Parent}	A	Fitting range (MeV)
^{152}Nd	^{152}Pr	(4^+)	0.94 ± 0.11	$0.4 - 1.5$
^{154}Nd	^{154}Pr	(3^+)	1.45 ± 0.19	$0.3 - 1.0$

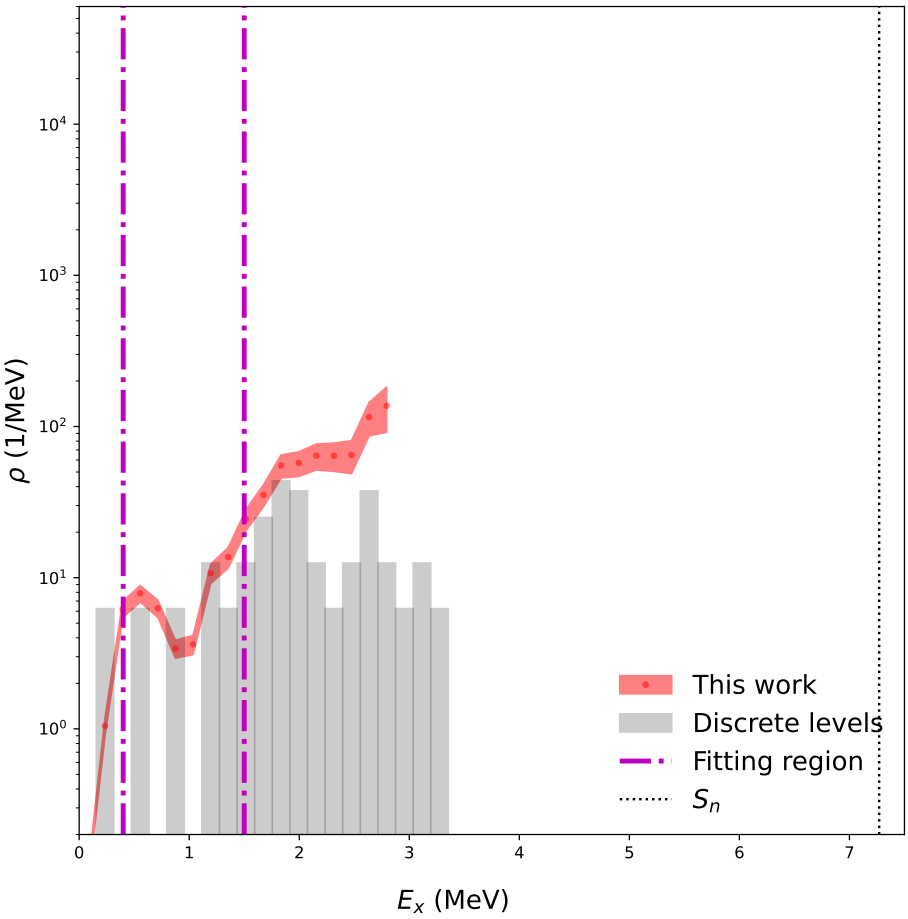

Figure 7.3 The absolute partial level density for ^{152}Nd, plotted together with discrete levels [59] could be populated from the β decay from ^{152}Pr and a dipole transmission. The dash-dotted magenta lines show the region used for finding A.

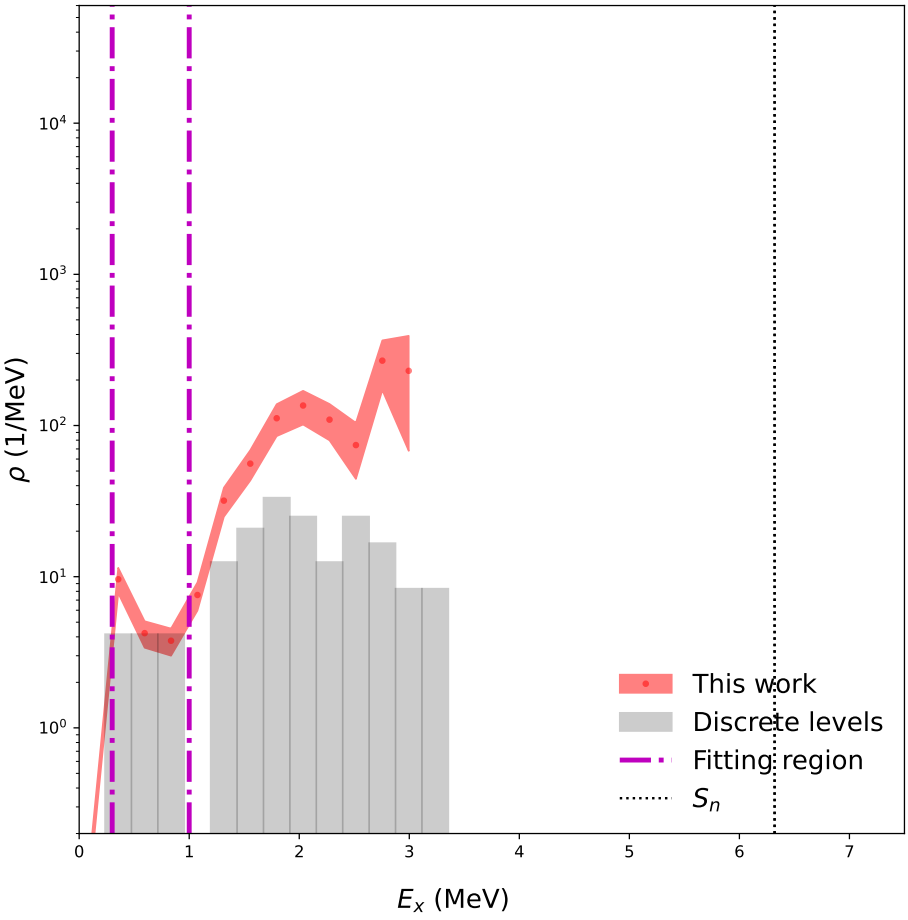

Figure 7.4 The absolute partial level density for ^{154}Nd, plotted together with discrete levels [60] could be populated from the β decay from ^{154}Pr and a dipole transmission. The dash-dotted magenta lines show the region used for finding A.

discrete levels used in the normalization to account for the magnitude of the nuclear level density. To account for this, if a normalization range for the magnitude surpassed three bins, the choice of the range was taken into account and propagated into the nuclear level density. For each energy range of extraction in the first generation matrix, this was done to make sure it was systematically propagated into the experimental result.

For this work, this was done with a minimizer that would find the A by sampling the extracted ρ' within the uncertainty band and performed a χ^2-minimization to the known levels within a given fitting region. To reduce uncertainty, this was done in subsets of the fitting region to decrease instability and take into account variations in the fitting window chosen as well. From this Monte Carlo fitting procedure of the magnitude A of the level density, we also extracted the uncertainty,

σ_A, of the magnitude with the fluctuations due to the statistical limits and the fitting window chosen.

E_x (MeV)	$\rho\,(E_x)\,\left(\text{MeV}^{-1}\right)$	$\sigma_\rho\,\left(\text{MeV}^{-1}\right)$
-0.085	6.88×10^{-2}	8.75×10^{-3}
0.075	9.57×10^{-2}	1.10×10^{-2}
0.235	1.04	1.50×10^{-1}
0.395	6.20	7.65×10^{-1}
0.555	7.88	9.88×10^{-1}
0.715	6.28	8.13×10^{-1}
0.875	3.39	4.61×10^{-1}
1.035	3.62	5.29×10^{-1}
1.195	1.07×10	1.57
1.355	1.37×10	2.12
1.515	2.43×10	3.89
1.675	3.53×10	5.88
1.835	5.52×10	9.63
1.995	5.73×10	1.06×10
2.155	6.41×10	1.25×10
2.315	6.40×10	1.36×10
2.475	6.47×10	1.60×10
2.635	1.15×10^{2}	2.89×10
2.795	1.37×10^{2}	4.54×10

Table 7.6 The values for the ^{152}Nd NLD ($\rho\,(E_x)$) with the uncertainty (σ_ρ).

7.4 Fitting nuclear level density

The experimental NLD was fit using the semi-microscopic models of Goriely *et al.* [12] and *et al.* [86]. These microscopic models were adjusted to experimental data by two parameters when running, "ctable" and "ptable". This model includes two adjustment parameters as shown in the equation:

$$\rho(E_x-\delta,J,\pi)=\exp\left(c\sqrt{E_x-\delta}\right)\rho_m\,(E_x-\delta,J,\pi), \tag{7.11}$$

where E_x is the excitation energy, J the spin, π the parity, c scales the slope, δ is a shift that is used to change the E_x of the microscopic level density ρ_m. For astrophysical calculations of nucleosynthesis, in terms of models in TALYS, the preferred model is the level density model 5.

E_x (MeV)	$\rho\,(E_x)\,\left(\text{MeV}^{-1}\right)$	$\sigma_\rho\,\left(\text{MeV}^{-1}\right)$
-0.125	9.87×10^{-2}	1.85×10^{-2}
0.115	1.60×10^{-1}	3.00×10^{-2}
0.355	9.60	1.85
0.595	4.23	8.51×10^{-1}
0.835	3.76	7.76×10^{-1}
1.075	7.56	1.62
1.315	3.18×10	7.00
1.555	5.59×10	1.28×10
1.795	1.12×10^{2}	2.68×10
2.035	1.35×10^{2}	3.43×10
2.275	1.09×10^{2}	2.97×10
2.515	7.41×10	3.00×10
2.755	2.68×10^{2}	9.74×10
2.995	2.30×10^{2}	1.62×10^{2}

Table 7.7 The values for the ^{154}Nd NLD ($\rho\,(E_x)$) with the uncertainty (σ_ρ).

In the TALYS framework, a transformation can be done for LD model 4, 5, and 6. For the TALYS input, c is the "ctable" parameter, and δ is the "ptable" parameter.

In literature, when fitting to available data from stable isotopes, both c and δ are usually in the range of ±1, but there are significant outliers present in the previously published data [12]. An assumption in this analysis is that the model is equally valid for partial level densities, as shown in [79], where the partial level density fitted to experimental data is assumed to be within the allowed β decay and then an $L = 1$ transition. This can cause discrepancies at lower energies, as the partial level density can be inaccurate and thus limit the application. The less data available for the level density, the harder it is to fit the theoretical description of level densities.

The fitting parameters of the TALYS level density models fitted to the partial level densities of ^{152}Nd and ^{154}Nd are presented in Table 7.8. In the same table, the fitting range used for the magnitude and the level density at the neutron separation energy are also presented, along with the covariance matrix from the fit of the adjusted partial level densities from the TALYS models.

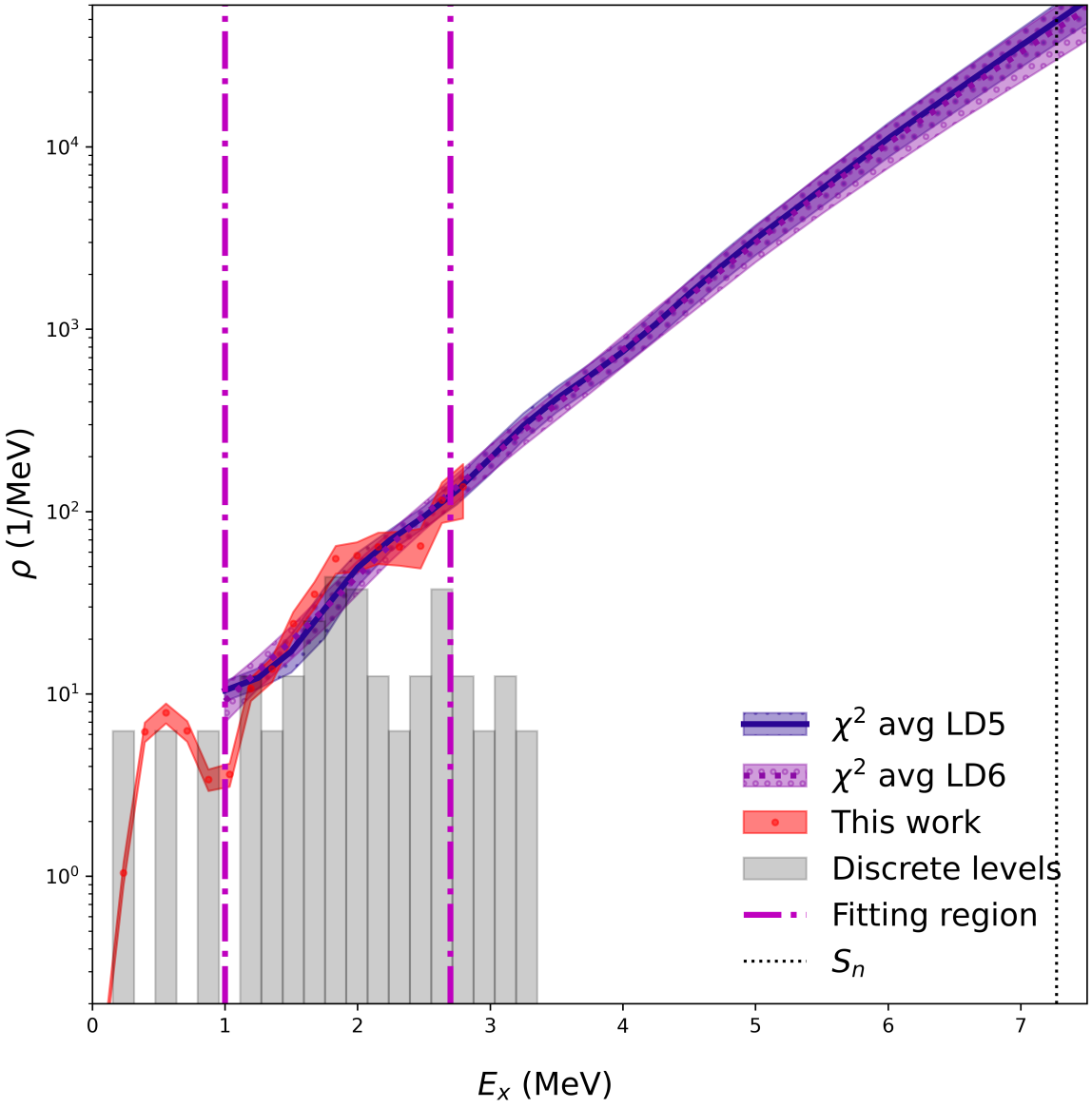

Figure 7.5 This plot shows the extracted partial level density of ^{152}Nd in red. The fitting of level density models 4 – 6 in TALYS to the constrained partial level density. For the fits, the fitting region is marked with the magenta lines. Discrete levels that can be populated via β decay are shown in gray. The neutron separation energy is marked with the black dotted line.

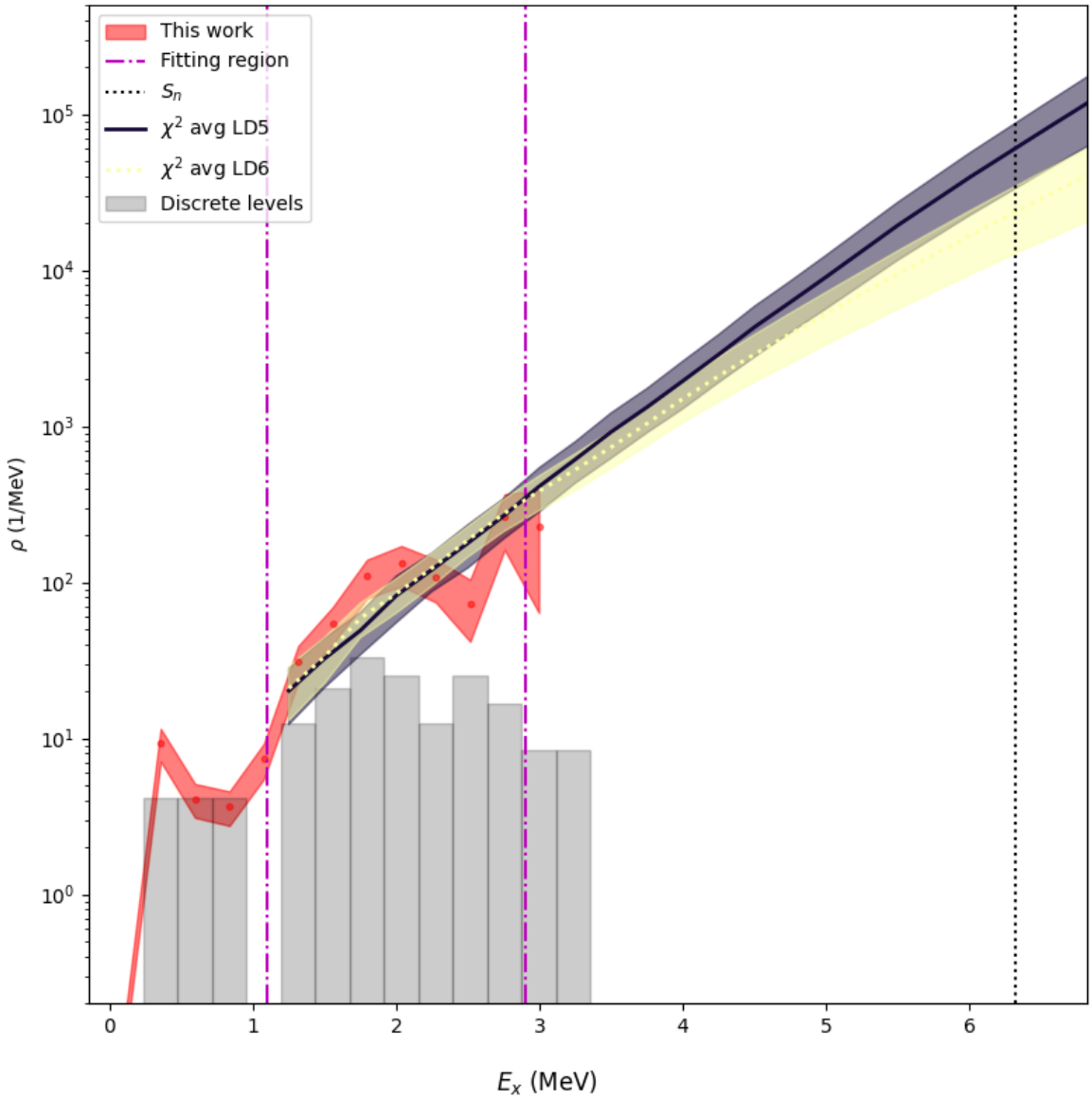

Figure 7.6 This plot shows the extracted partial level density of ^{154}Nd in red. The fitting of level density models 4 – 6 in TALYS to the constrained partial level density. For the fits, the fitting region is marked with the magenta lines. Discrete levels that can be populated via β decay are shown in gray. The neutron separation energy is marked with the black dotted line.

Table 7.8 Fitting of the c and δ parameters of the TALYS models for ^{152,154}Nd, including the uncertainty, the partial level density at the neutron separation energy S_n, and the covariance matrix $\mathrm{Cov}[c, \delta]$ as well.

Nucleus	Fit range (MeV)	LD model	c	δ (MeV)	$\rho(S_n)$ $\left(10^4\,\mathrm{MeV}^{-1}\right)$	$\mathrm{Cov}[c, \delta]$
^{152}Nd	1 – 2.7	5	-1.07 ± 0.14	0.04 ± 0.18	12.3 ± 3.17	$\begin{pmatrix} 0.03 & 0.03 \\ 0.03 & 0.05 \end{pmatrix}$
		6	-1.07 ± 0.19	0.04 ± 0.24	9.43 ± 3.29	$\begin{pmatrix} 0.05 & 0.06 \\ 0.06 & 0.08 \end{pmatrix}$
^{154}Nd	1.1 – 2.9	5	-0.49 ± 0.25	0.0053 ± 0.28	13.2 ± 6.6	$\begin{pmatrix} 0.06 & 0.03 \\ 0.03 & 0.05 \end{pmatrix}$
		6	-0.89 ± 0.24	-0.13 ± 0.26	4.82 ± 2.30	$\begin{pmatrix} 0.06 & 0.03 \\ 0.03 & 0.05 \end{pmatrix}$

7.5 Fitting the γSF

To calculate the neutron-capture cross sections, the γSF needs to be parametrized with a functions and the uncertainty of the constrained γSF. To be able to constrain the γSF of ^{152,154}Nd, and apply it in a Hauser-Feshbach calculation of the neutron capture cross-section on our nuclei of interest, ^{151,153}Nd, a functional form can be used. This includes some assumptions of the general form and any resonances in the γSF. For this case, the assumption is that the f_{E1} is dominated by the giant dipole resonance, and by the presence of a scissors mode resonance. In addition, the lower end of the γSF is assumed to either be the sum of these two resonances, or an addition of a constant. The upper and lower limits of these fits are included in the TALYS calculations, as there is no good discrimination criteria for the validity of a constant to the γSF. This is especially valid for the fit of the γSF and of ^{154}Nd as the parameters for the GDR resonance is not known, rather assuming it is similar to the GDR of the closest measured GDR, that of ^{151}Nd. For ^{152}Nd, the extracted fits of the γSF are shown in Figure 7.7, and ^{154}Nd is shown in Figure 7.8.

For ^{152}Nd in Figure 7.7, the plot shows the fit assuming that the magnitude is the same as

that of ^{151}Nd from M. Guttormsen *et al.* [84], with a scissors mode resonance. The blue band fit parameters are shown in Table B.1. The pink band assumes that a constant is also added, and the fit parameters are given in Table B.2.

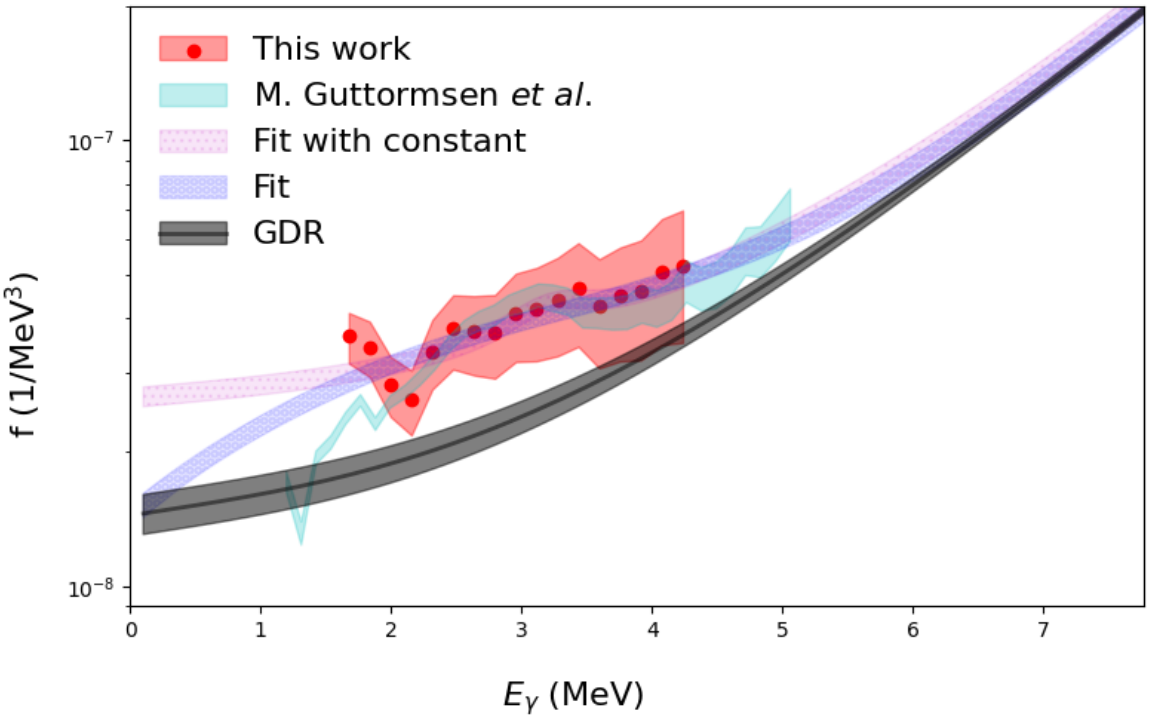

Figure 7.7 The fit of the extracted γSF of ^{152}Nd shown in red. The plot shows the fit assuming that the magnitude is the same as that of ^{151}Nd from M. Guttormsen *et al.* [84], shown in cyan. The blue band is a combination of the GDR and a scissors mode resonance, while the pink band also has a constant added.

For ^{154}Nd in Figure 7.8, the top plot shows the fit assuming that the magnitude is the same as that of ^{151}Nd from M. Guttormsen *et al.* [84], with a scissors mode resonance. The blue band fit parameters are shown in Table B.5. The pink band assumes that a constant is also added, and the fit parameters are given in Table B.6. In the bottom plot of Figure 7.8, the fit is done assuming the same magnitude as the GDR from ^{151}Nd, shown in the black band, with no scissors mode resonance, in the blue band, and pink with a constant added. The respective fit parameters are in Tables B.3 and B.4.

Describing γ-strength function of the GDR can be done by summing up two generalized

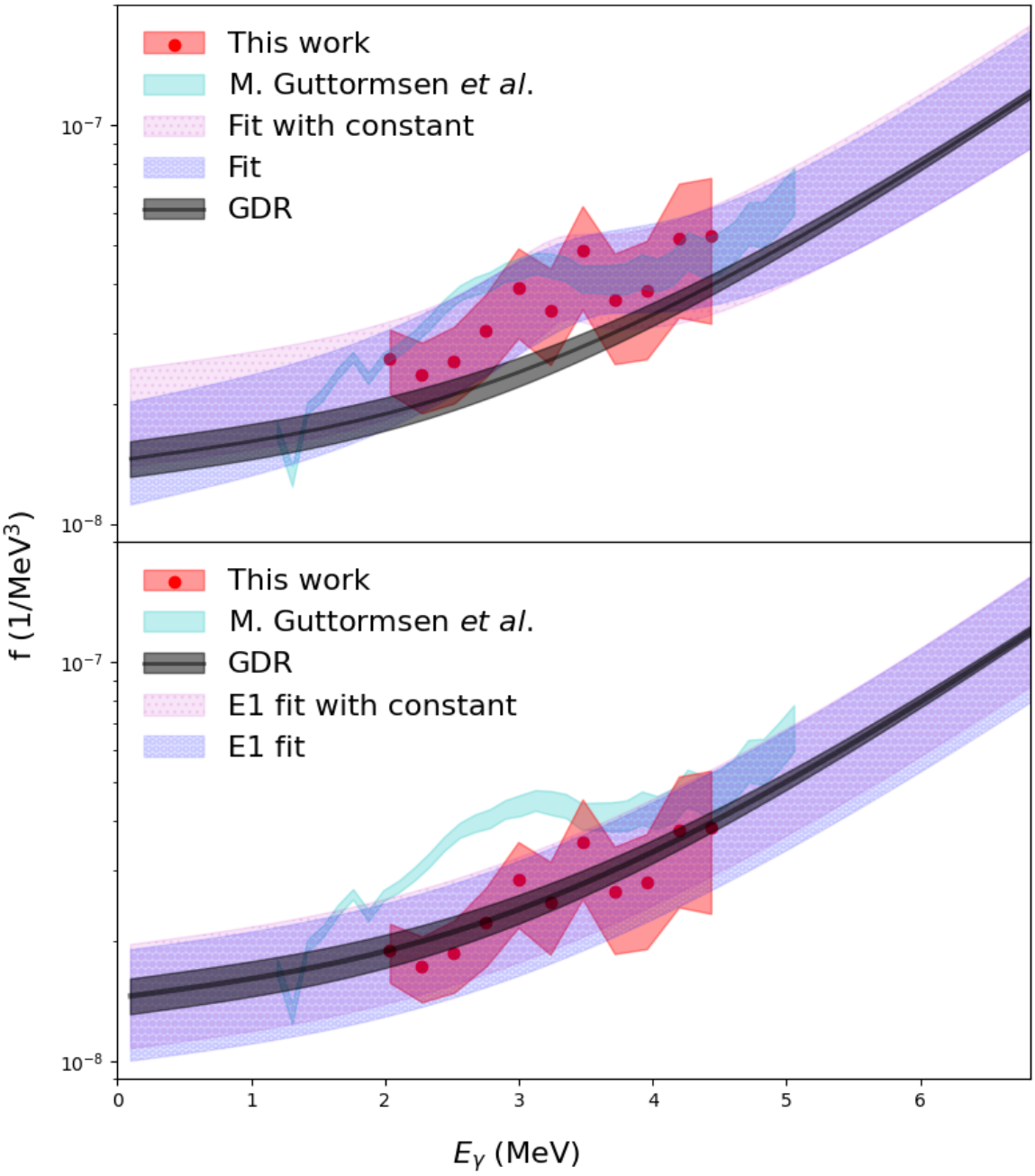

Figure 7.8 The fit of the extracted γSF of ^{154}Nd shown in red. The top plot shows the fit assuming that the magnitude is the same as that of ^{151}Nd from M. Guttormsen *et al.* [84], shown in cyan. The bottom shows the fit assuming that it is the same magnitude as the GDR from ^{151}Nd, shown in the black band, with no scissors mode resonance.

Lorentzians (GLO), where they take the form as given in Equation (7.12),

$$f_{\mathrm{E1}}(E_\gamma) = \frac{1}{3\pi^2\hbar^2c^2}\sigma_{\mathrm{E1}}\Gamma_{\mathrm{E1}} \times \left(\frac{E_\gamma \Gamma(E_\gamma, T_f)}{\left(E_\gamma^2 - E_{\mathrm{E1}}^2\right) + E_\gamma^2\Gamma^2\left(E_\gamma, T_f\right)} + 0.7\frac{\Gamma\left(E_\gamma = 0, T_f\right)}{E_{\mathrm{E1}}^3} \right), \tag{7.12}$$

where $f_{\mathrm{E1}}(E_\gamma)$ is the E1 strength as a function of the γ-ray energy, E_γ. Each part of the resonance is defined by the energy E_{E1}, width Γ_{E1}, and the strength σ_{E1}. T_f defines the tail end at low energies, and is set to $T_f = 0.50(5)$ MeV for consistence in defining the transformation of the slope, based on the work done by M. Guttormsen *et al.* on $^{142,144,145-151}$Nd, [84]. Additionally, the term $\Gamma(E_\gamma, T_f)$ is defined in Equation (7.13)

$$\Gamma(E_\gamma, T_f) = \frac{\Gamma_{\mathrm{E1}}}{E_{\mathrm{E1}}^2}\left(E_\gamma^2 + 4\pi^2T_f^2\right), \tag{7.13}$$

and the constant is defined in Equation (7.14) as

$$\frac{1}{3\pi^2\hbar^2c^2} = 8.674 \times 10^{-8}\,\mathrm{mb}^{-1}\mathrm{MeV}^{-2}. \tag{7.14}$$

For the other part of the fit, we use the Standard Lorentzian (SLO) model to describe the scissors mode dipole resonance in Equation (7.15); this can be used for well deformed nuclei.

$$f(E_\gamma) = \frac{1}{3\pi^2\hbar^2c^2}\frac{E_\gamma\Gamma(E_\gamma, T_f)}{\left(E_\gamma^2 - E_{\mathrm{E1}}^2\right) + E_\gamma^2\Gamma^2}, \tag{7.15}$$

again the parameters of the resonance are energy, E, width Γ, and the strength σ.

CHAPTER 8

RESULTS AND DISCUSSION

8.1 Neutron capture cross-section

From the extracted statistical properties presented in Chapter 7, we can calculate an experimentally constrained the neutron capture cross-section and reaction rate to create ^{152}Nd and ^{154}Nd with the Hauser-Feshbach code TALYS version 1.96. Here, the constrained neutron capture cross-section on ^{152}Nd and ^{154}Nd are shown together with the corresponding uncertainty bands, along with NON-SMOKER [87] cross sections for comparison.

^{151}Nd(n,γ)^{152}Nd

The constrained ^{151}Nd(n,γ)^{152}Nd cross section is shown in Figure 8.1. In this, we see this work in the shaded gray band, which is all within the total band from all TALYS combinations in the pink band. On the same figure, the NON-SMOKER calculation is shown in the black dash-dotted line.

For the ^{151}Nd(n,γ)^{152}Nd , the impact of the level density model choice is shown in Figure 8.2. For both models, it can be seen that they correspond to the lower end of the TALYS uncertainty band, and they are below the TALYS mean and the NON-SMOKER cross section for both cases. Additionally, in the bottom panel of Figure 8.2, it can be seen that the cross sections from the two different level densities have major overlap for all energies.

^{153}Nd(n,γ)^{154}Nd

The final results for the newly constrained neutron capture cross-section of ^{153}Nd(n,γ)^{154}Nd from this work is shown in Figure 8.3. For the ^{153}Nd(n,γ)^{154}Nd reactions, the impact of the level density model choice is shown in Figure 8.4, where the new results are more constrained than the prospective level density model in TALYS, yet still within the uncertainty band.

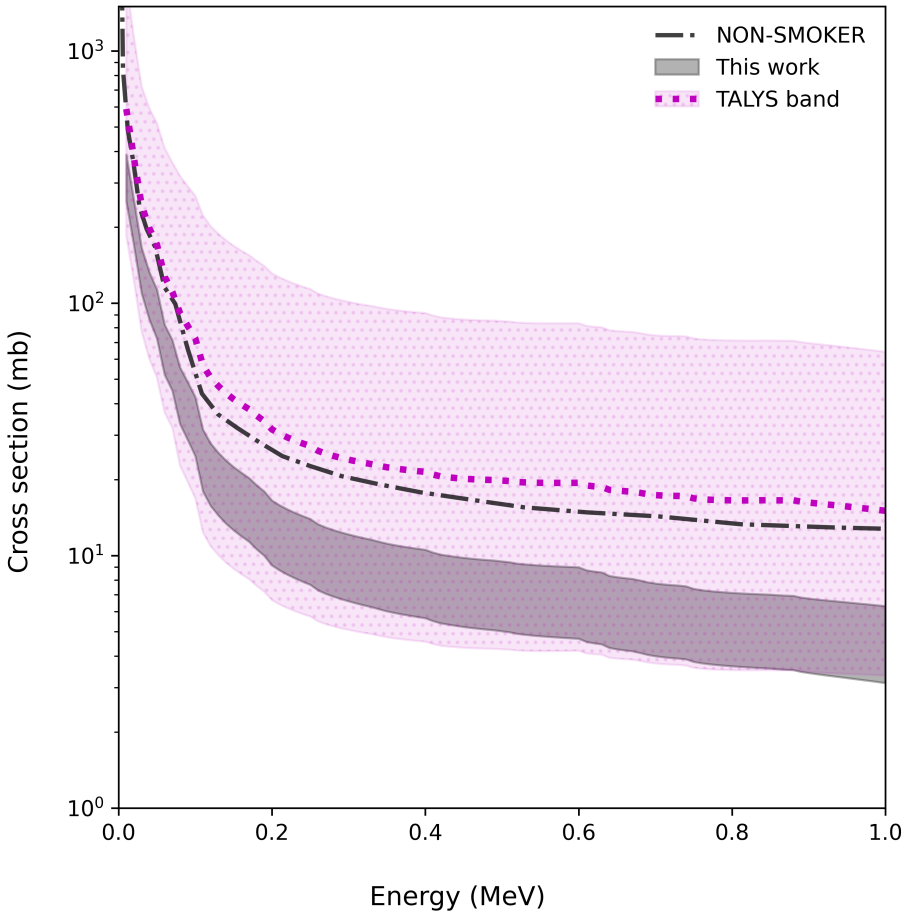

Figure 8.1 The constrained neutron capture cross-section of ^{151}Nd(n,γ)^{152}Nd, shown in gray, with the TALYS uncertainty band shown in light pink, with the mean shown as the dotted magenta line. The NON-SMOKER [87] cross section is shown as the black dash-dotted line.

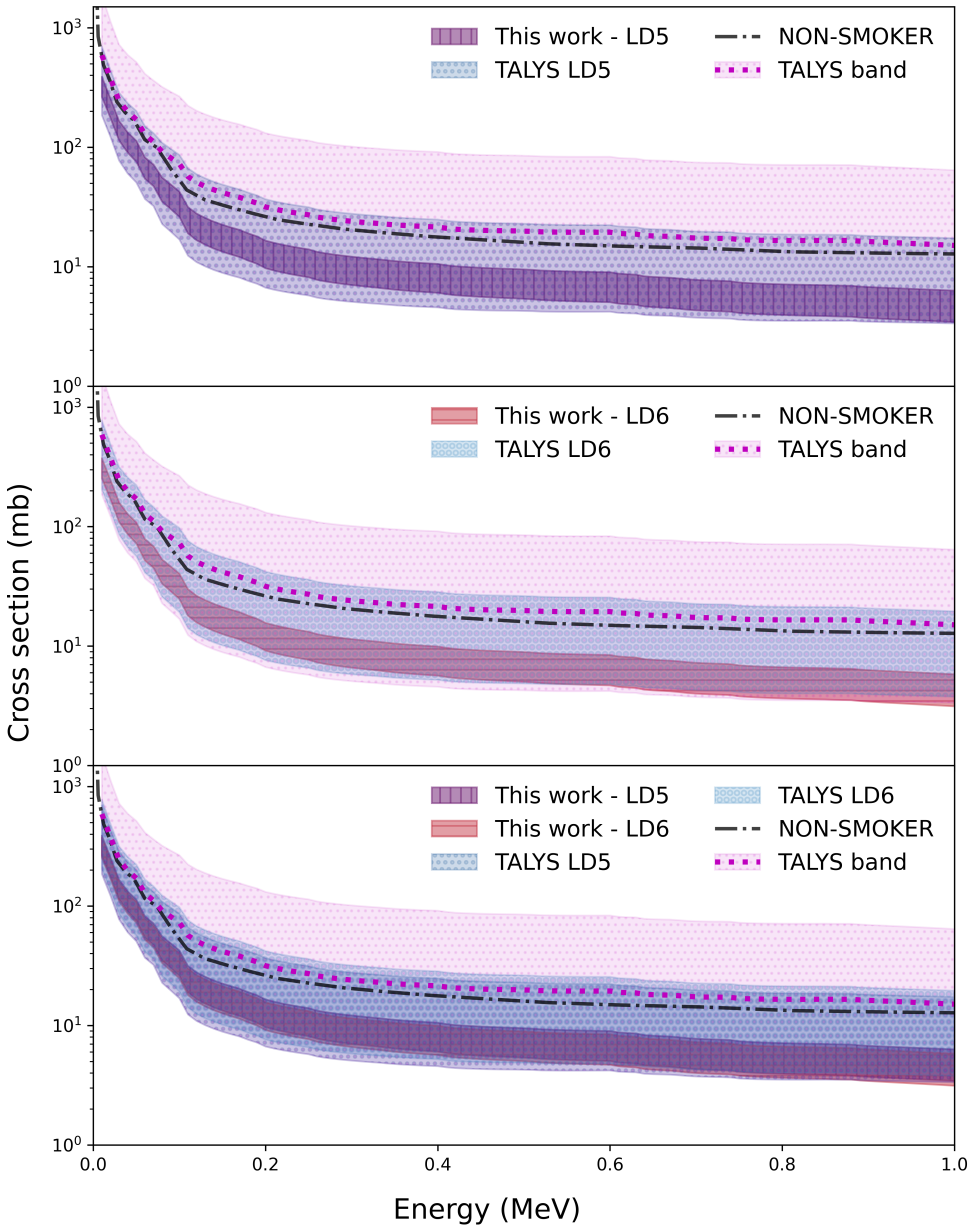

Figure 8.2 The constrained neutron capture cross-section of the ^{151}Nd(n,γ)^{152}Nd with the corresponding cross section from the default TALYS level density models 5 and 6.

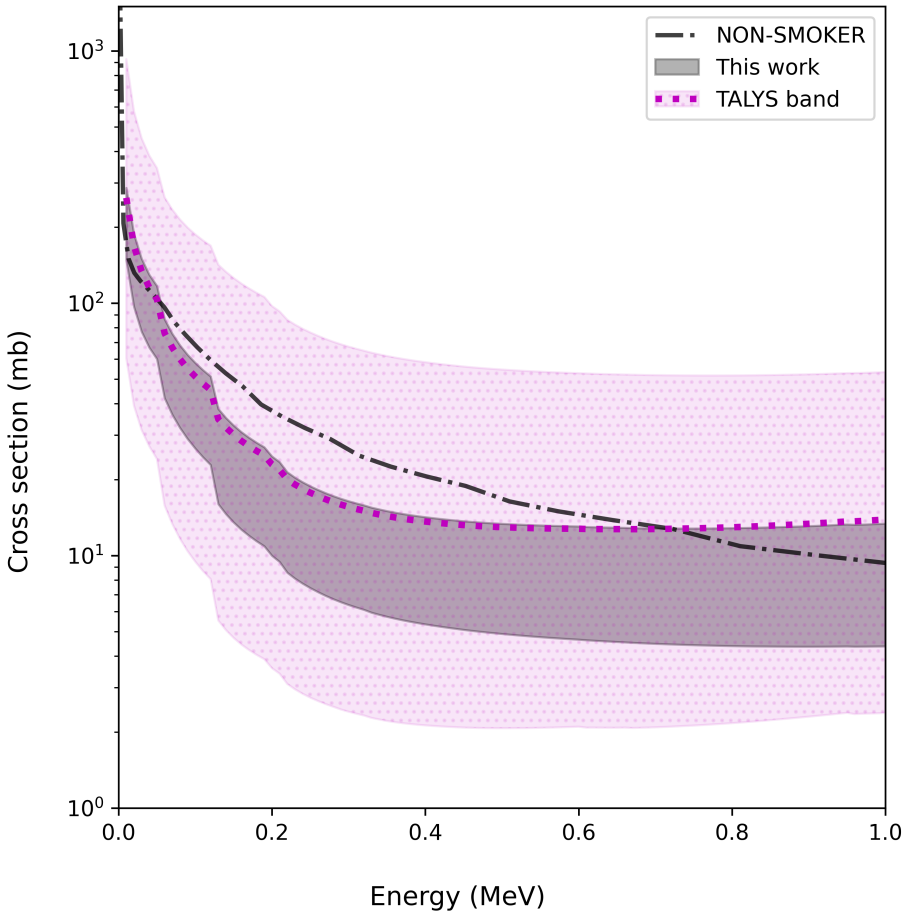

Figure 8.3 The constrained neutron capture cross-section of ^{153}Nd(n,γ)^{154}Nd is labeled, shown in gray, with the TALYS uncertainty band shown in light pink, with the mean shown as the dotted magenta line. The NON-SMOKER cross section is shown as the black dash-dotted line.

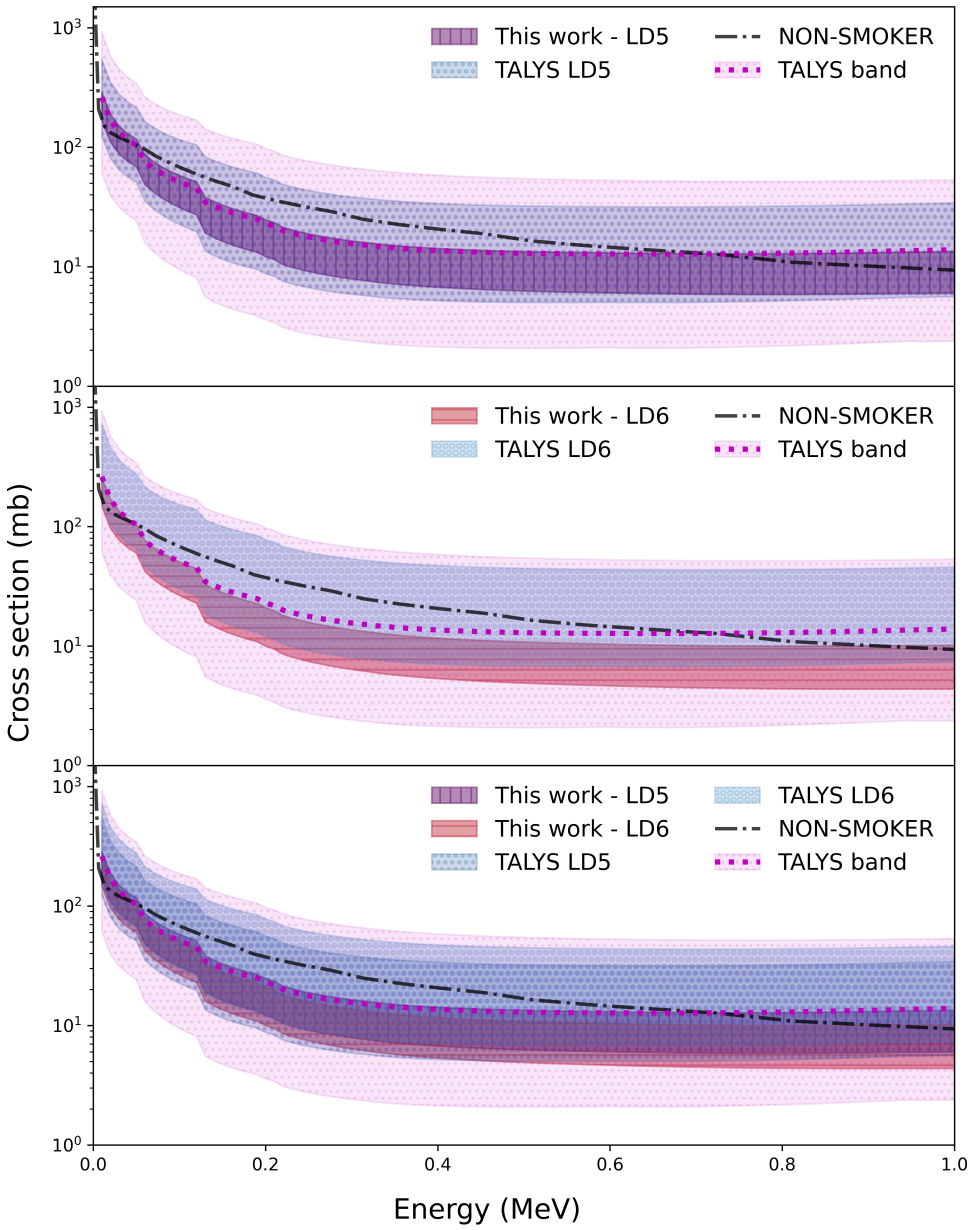

Figure 8.4 The constrained neutron capture cross-section of the ^{153}Nd(n,γ)^{154}Nd with the corresponding cross section from the default TALYS level density models 5 and 6.

8.2 Neutron capture reaction rate

To look at the reaction rates for ^{151,153}Nd(n,γ)^{152,154}Nd, we ran TALYS at a larger temperature range. For the sensitivity studies by Denissenkov *et al.* [32], the temperature of interest is at ≈ 0.2 GK. Next, we examined how the constrained reaction rate impacts the production of europium in *i*-process sites. This reduces the impact from the nuclear uncertainties in the [Eu/La] abundances for possible *i*-process sites, and more accurately simulate *i*-process pathways for nucleosynthesis in the A = 150 range.

^{151}Nd(n,γ)^{152}Nd

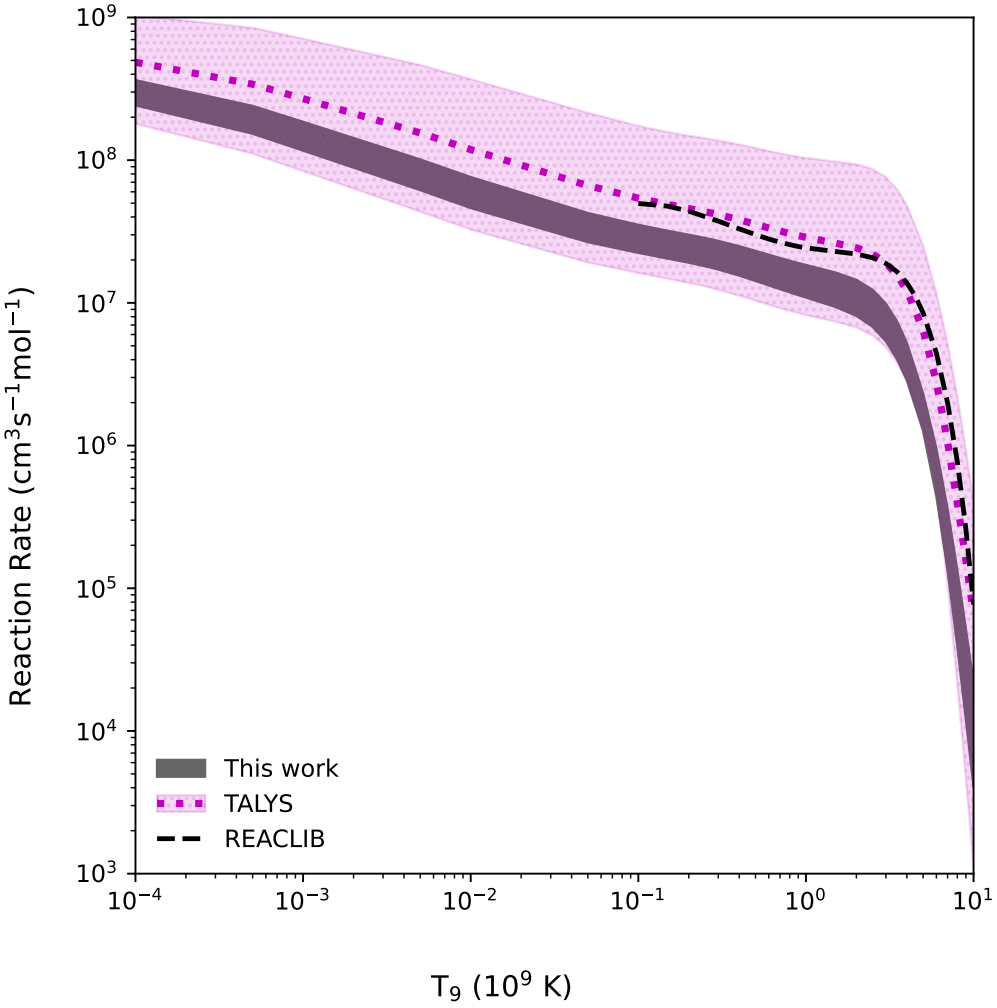

Figure 8.5 The constrained reaction rate for the ^{151}Nd(n,γ)^{152}Nd, with the uncertainty band from TALYS shown in pink, with the TALYS default as a pink dashed line.

The constrained neutron capture reaction rate on ^{151}Nd can be seen in Figure 8.5, in the shaded purple band. In the same figure, we have the overall TALYS band shown as the pink band, with the TALYS default shown as the dashed pink line. For all temperatures, this constrained reaction rate is below the TALYS default, but the TALYS band still overlaps with the experimentally constrained reaction rate.

Breaking down the constrained reaction rate based on the level density models, we can see a comparison of the (n,γ) capture on ^{151}Nd based on the fitted TALYS level density models 5 and 6 in Figure 8.6. Here, we can see the LD5 and LD6 options which have the experimentally constrained γSF included. This is lower than any of the combinations of these level density models combined with all possible models of the γSF available in TALYS. Additionally, with level density models 5 and 6, we see that these are on the lower range of the reaction rate uncertainty band for all TALYS combinations, which is reflected well in Figure 8.5. The REACLIB [39] rate is in agreement with this work.

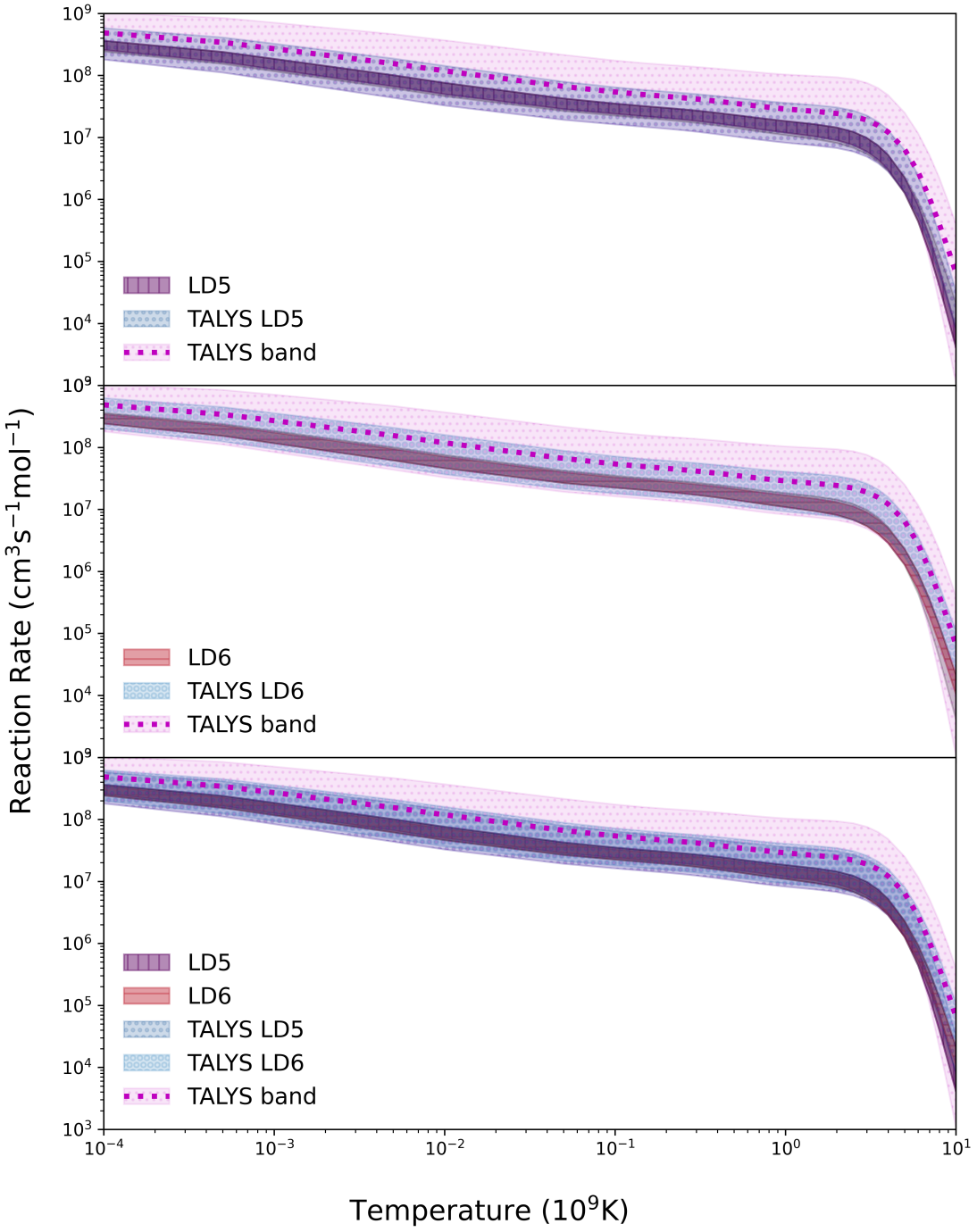

Figure 8.6 Comparison of the reaction rates with the applied fit from the partial level density to the level density model 5 and 6 on the reaction rate, compared to the general uncertainty of the level density in TALYS with all possible γSF in TALYS.

^{153}Nd(n,γ)^{154}Nd

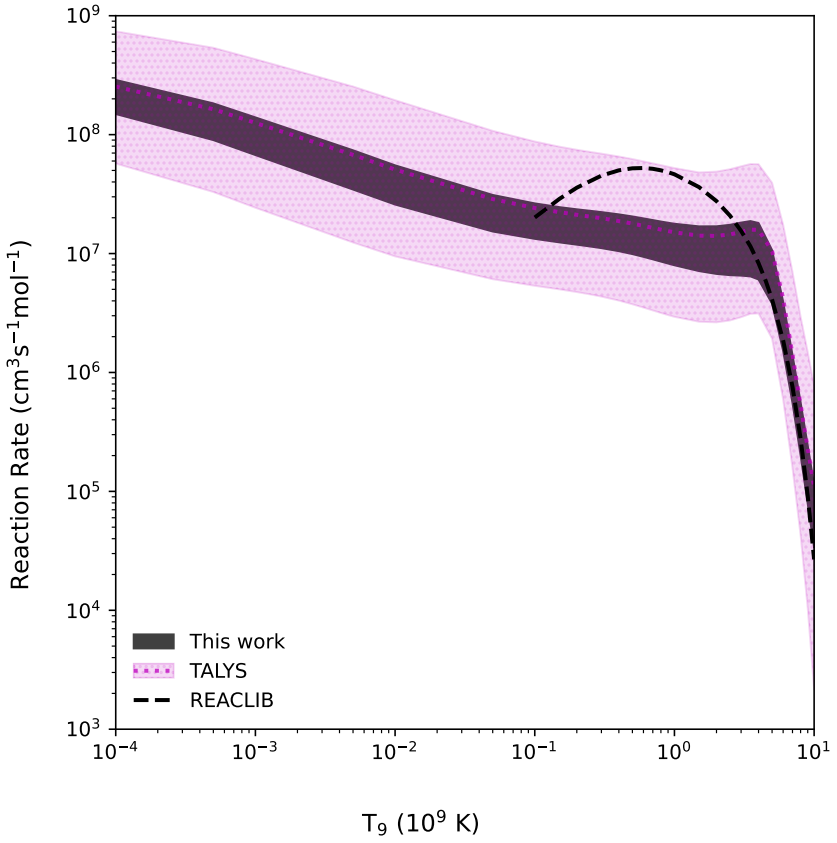

Figure 8.7 The constrained reaction rate for the ^{153}Nd(n,γ)^{154}Nd, with the uncertainty band from TALYS shown.

Similarly as in the ^{151}Nd case, the constrained neutron capture reaction rate on ^{153}Nd can be seen in Figure 8.7, in the shaded purple band. In the same figure, we have the overall TALYS band shown as the pink band, with the TALYS default shown as the dashed pink line. For all temperatures, the TALYS default reaction rate is within the experimentally constrained rate. However, here it is in the upper range of the experimentally constrained reaction rate here. The REACLIB rate [39] is not in good agreement with this work. Breaking down the constrained reaction rate based on the level density models, we can see a comparison of the (n,γ) capture on ^{153}Nd based on the fitted TALYS level density models 5 and 6 in Figure 8.8. Here, we can see the LD5 and LD6 options which have the experimentally constrained γSF included. This is lower than any of the combinations of these level density models combined with all possible models of the γSF available

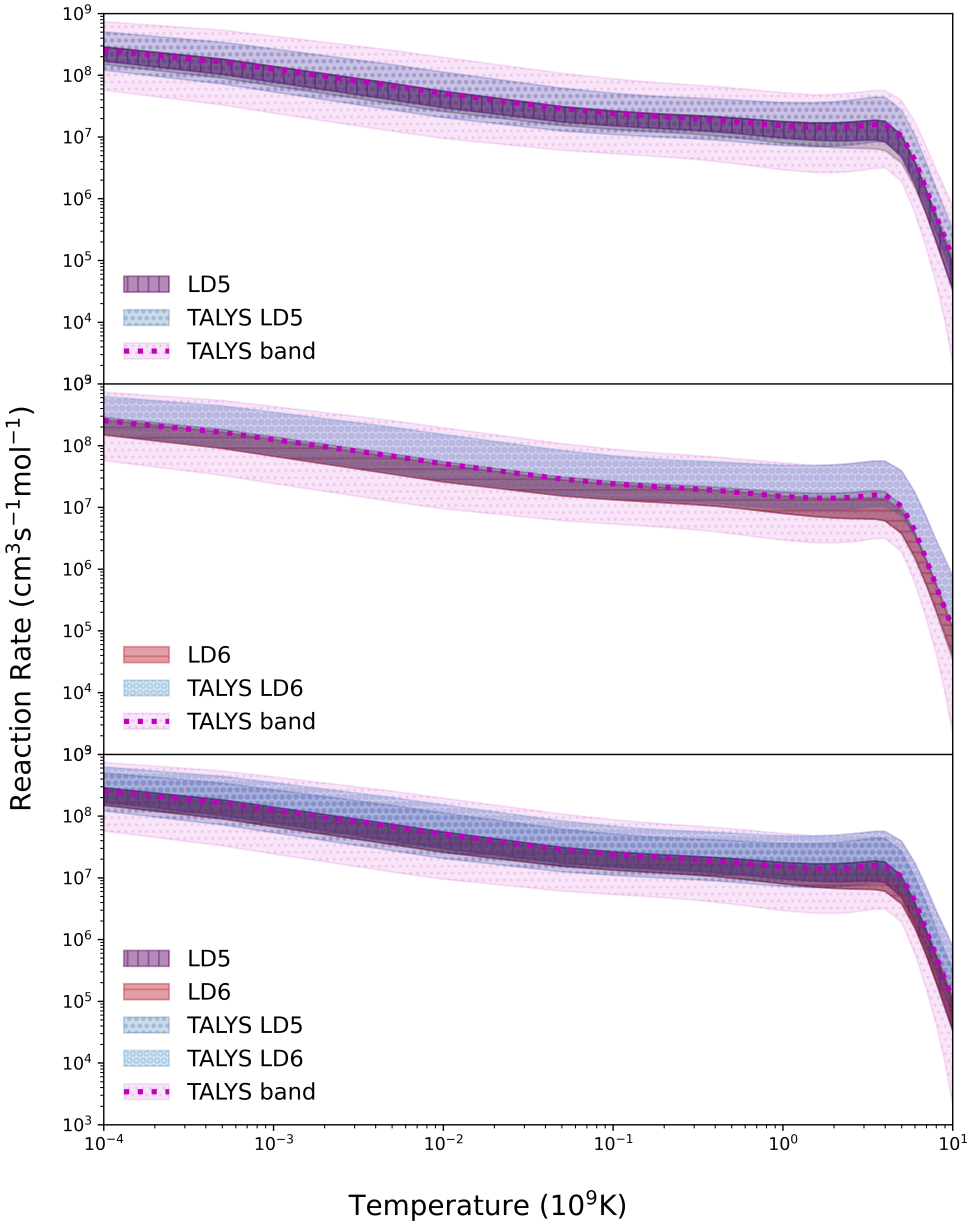

Figure 8.8 Comparison of the reaction rates with the applied fit from the partial level density on the reaction rate, compared to the general uncertainty of the level density in TALYS with all possible γSF in TALYS.

in TALYS. Additionally, with level density models 5 and 6, we see that these are on the upper end of the TALYS default reaction rate, and within the general range of the TALYS uncertainty band shown in Figure 8.8.

8.3 Astrophysical implications

Based on these newly constrained neutron capture cross-sections, we performed calculations to constrain the abundance of Eu for the carbon-enhanced metal poor star as described in Section 3.5, with the results from Spyrou *et al.* shown in Figure 8.9 for comparison. Figure 8.10 shows how the constrained rate on ^{151}Nd affects the [Eu/La] ratio for two different N_n in Figure 8.10.

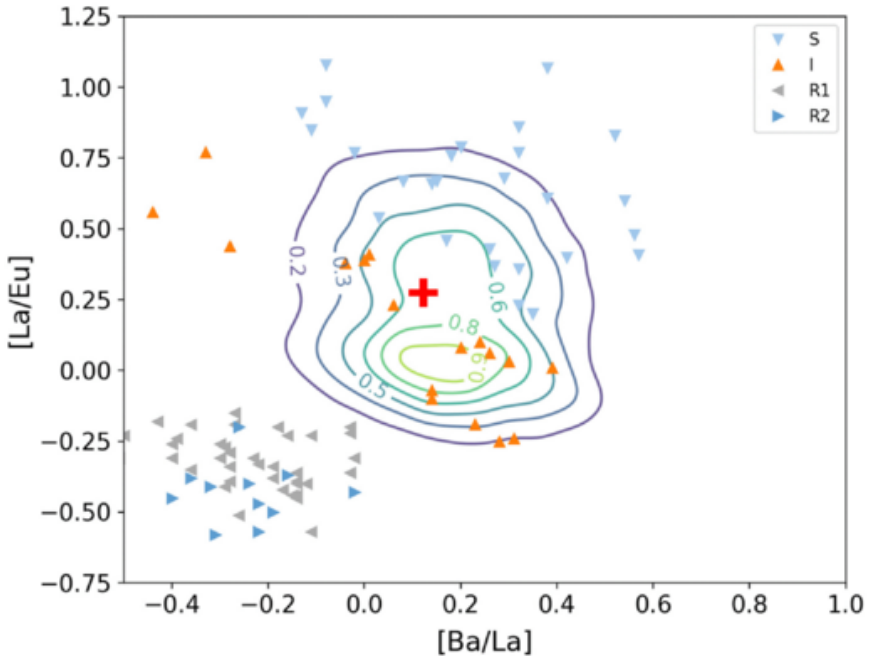

Figure 8.9 Constraining uncertainties in key neutron capture cross-sections can provide insights to potential sites of the i process. Top figure shows possible combinations of [La/Eu] to [Ba/La] ratios for i process, with a wide spread due to nuclear uncertainties in the ^{139}Ba(n,γ)^{140}Ba, with the constrained cross-section showing the effect in the bottom plot. Figure taken from Ref. [38].

For the $\log_{10} N_n(\mathrm{cm}^{-3}) = 13.5$ case, the [La/Eu] uncertainties are well constrained with these results. It can be seen that the contour overlaps several CEMP-i stars, which gives an indication that these stars could have the same neutron densities as the simulation. For the higher neutron density, $\log_{10} N_n(\mathrm{cm}^{-3}) = 14.5$, the results seem to have less of an impact in constraining the uncertainties in the [La/Eu] abundance ratio. This is most likely due to the pathway changing as higher neutron densities may lead to production of more neutron rich nuclei. In Ref. [88], they show that the sensitivity of the neutron capture cross-sections involved changes with the neutron density. With this in mind, it could be that other neutron capture cross-sections need to be constrained to reduce

the uncertainty in the predicted abundance ratios.

For lower neutron densities, the constrained neutron capture cross-section on ^{153}Nd did not have a significant impact on reducing the uncertainty in the [La/Eu], as was later detailed in [88]. However, it becomes important for $\log_{10} N_n \left(\mathrm{n\,cm^{-3}}\right) = 15.4$. This is probably due to higher neutron densities pushing the i process pathway further from stability, as the probability of neutron capture increases due to the increased density. Additionally, with more nuclei involved in the nucleosynthesis, this can change the sensitivity towards which nuclei are involved in creating europium.

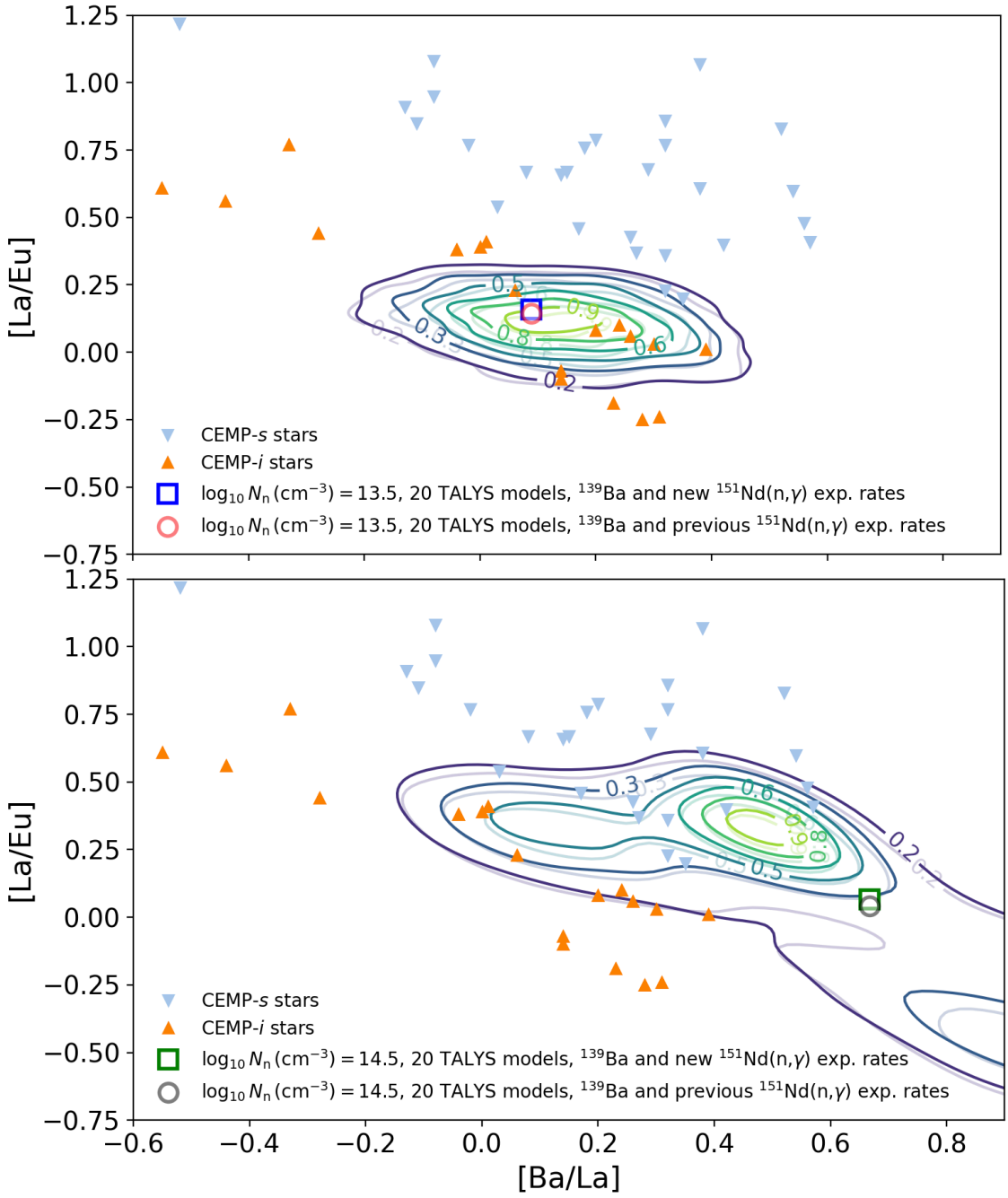

Figure 8.10 With the constrained reaction rates on ^{151}Nd, including this in the i process network calculations affects the possible ratios of [La/Eu] to [Ba/La], plotted together with observations of CEMP-s/i stars. Figures from [89]. Top) New constrained the uncertainties for $\log_{10} N_n(\mathrm{cm}^{-3}) = 13.5$ based on this work. Bottom) New constrained the uncertainties for $\log_{10} N_n(\mathrm{cm}^{-3}) = 14.5$ based on this work.

CHAPTER 9

SUMMARY AND CONCLUSION

Based on the sensitivity study from Denissenkov *et al.*[32], an experiment was designed using the β-Oslo method to constrain important neutron captures for the i-process nucleosynthesis. The experiment was run using the CARIBU facility at Argonne National Lab (ANL). The beam settings used for the experiment were A=152,153,154. For each beam setting, we measured the β-particles with SuNSPOT, in coincidence with any outgoing γ rays detected in our total absorption spectrometer, SuN. To be able to isolate our nuclei of interest, we used the SuNTAN tape station with different beam on/off cycles based on the half-lives in the respective decay chains.

After the experiment, the SuN detector was calibrated using well-known radioactive sources. Applying time gates on the coincidences and appropriate energy thresholds on both SuN and the SuNSPOT detector reduced background noise. The data from the nuclei of interest was found by gating on certain parts of the tape cycle, and in the case of ^{154}Nd, gating on the appropriate parts of the tape cycle to extract the background, then doing a scaled subtraction to get the final results. The final product for the nuclei of interest was the particle-γ matrix.

Using the β-Oslo method, the E_x–E_γ matrices were unfolded to take into account the detector response, both for the γ rays, E_γ, and the excitation energy, E_x. After the unfolding, an iterative procedure was used to find the primary-γ ray matrices, which show the first emitted γ in the cascade. From this first generation matrix, the functional forms of statistical properties can be extracted, given the region used is representative of statistical behavior in the nucleus.

In this work, the statistical properties of ^{152}Nd and ^{154}Nd have been extracted, and normalized. The magnitude of the partial level densities was normalized to discrete levels in ^{152,154}Nd, while the slopes of the γ-strength functions and partial level densities were fit to data from [14]. For the normalization, a large part of this work was developing and writing the code for this procedure, which involved many different variations of fitting procedures, uncertainty propagation and sampling routines.

To constrain the ^{151,151}Nd(n,γ)^{152,154}Nd cross section and reaction rate, two level densities in

TALYS were fit to the partial level densities, and the extracted γ-strength functions were fit with functions capturing the behavior of the resonances present, along with the option of a low-energy enhancement or no low-energy enhancement. With these assumptions, the extracted statistical properties were used in the Hauser-Feshbach code TALYS to calculate the neutron-capture cross section and the nuclear reaction rate, propagating the uncertainty from the experiment and the normalization procedure.

Finally, the constrained reaction rate for the neutron capture on ^{151}Nd was used to constrain possible conditions for i-process nucleosynthesis based on the [La/Eu] abundance ratio for two different neutron densities. This newly constrained neutron capture reaction-rate reduced the uncertainty for $N_n = 3.16 \cdot 10^{14}$ n cm^{-3} especially [89]. From [88], the reaction rate for neutron capture on ^{153}Nd did not end up having a large effect on the uncertainty in the final abundance of Eu, thus no calculations were done on this.

In the future, the data from the same experiment can also be used to constrain the neutron-capture data on ^{152}Nd. This relies on more external data on the discrete levels in ^{153}Nd becoming available, which is needed for the normalization of the partial level density. From the experiment, it is also possible to do total abortion spectroscopy to extract the β-decay feeding intensity for the β decay from $^{152-154}$Pr to $^{152-154}$Nd.

APPENDIX A

CALIBRATION

Segment	1173 keV	1332 keV	59 keV	2614 keV	570 keV	1064 keV
B1	2606.18	2952.43	94.3127	5705.08	1297.02	2374.76
B2	2596.10	2940.58	80.1183	5688.36	1285.48	2,355.37
B3	2641.52	2991.19	107.713	5774.24	1312.27	2397.27
B4	2607.28	2955.8	90.5513	5715.18	1295.28	2375.40
T1	2615.86	2967.18	86.5992	5716.59	1297.44	2383.84
T2	2578.60	2921.99	71.2882	5661.10	1272.02	2337.72
T3	2626.38	2974.81	89.6804	5747.32	1297.96	2379.32
T4	2591.55	2940.82	88.6163	5679.54	1288.12	2364.15

Table A.1 Table showing the peaks used for calibration of the sun detector, along with the corresponding channel number that the peak was in, for each segment in the SuN detector after gainmatching.

APPENDIX B

γSF FIT PARAMETERS

B.1 Fits for ^{152}Nd

Table B.1 The Generalized Lorentzian GDR fit parameters, including a pygmy resonance, as shown as a blue band in Figure 7.7. This is assuming the magnitude is that of the ^{151}Nd γSF from Ref. [84]. Here, E is the energy, Γ the width and σ the strength of denoted resonances.

Parameter	μ	σ	μ_{weighted}	σ_{weighted}
σ_{pygmy} (mb)	6.49×10^{-1}	3.15×10^{-2}	6.47×10^{-1}	1.58×10^{-4}
Γ_{pygmy} (MeV)	6.37	1.28×10^{-1}	6.37	6.42×10^{-4}
E_{pygmy} (MeV)	4.24	1.03×10^{-1}	4.25	5.18×10^{-4}
σ_{GDR1} (mb)	2.13×10^{2}	2.47	2.13×10^{2}	1.24×10^{-2}
σ_{GDR2} (mb)	1.45×10^{2}	2.50	1.45×10^{2}	1.26×10^{-2}
E_{GDR1} (MeV)	1.34×10	9.63×10^{-2}	1.34×10	4.83×10^{-4}
E_{GDR2} (MeV)	1.65×10	3.96×10^{-1}	1.65×10	1.99×10^{-3}
Γ_{GDR1} (MeV)	6.70	2.25×10^{-1}	6.68	1.13×10^{-3}
Γ_{GDR2} (MeV)	4.00	2.01×10^{-1}	4.00	1.01×10^{-3}

Table B.2 The Generalized Lorentzian GDR fit parameters, including a pygmy resonance and a constant, C, added, as shown as a pink band in Figure 7.7. This is assuming the magnitude is that of the ^{151}Nd γSF from Ref. [84]. Here, E is the energy, Γ the width and σ the strength of denoted resonances.

Parameter	μ	σ	μ_{weighted}	σ_{weighted}
σ_{pygmy} (mb)	2.29×10^{-1}	1.15×10^{-2}	2.29×10^{-1}	5.49×10^{-5}
Γ_{pygmy} (MeV)	7.33×10^{-1}	1.47×10^{-2}	7.33×10^{-1}	7.02×10^{-5}
E_{pygmy} (MeV)	3.25	8.00×10^{-2}	3.25	3.82×10^{-4}
σ_{GDR1} (mb)	2.13×10^{2}	2.51	2.13×10^{2}	1.20×10^{-2}
σ_{GDR2} (mb)	1.45×10^{2}	2.51	1.45×10^{2}	1.20×10^{-2}
E_{GDR1} (MeV)	1.34×10	9.69×10^{-2}	1.34×10	4.63×10^{-4}
E_{GDR2} (MeV)	1.65×10	3.98×10^{-1}	1.65×10	1.90×10^{-3}
Γ_{GDR1} (MeV)	6.70	2.26×10^{-1}	6.68	1.08×10^{-3}
Γ_{GDR2} (MeV)	4.00	2.00×10^{-1}	4.00	9.54×10^{-4}
C	1.23	1.15×10^{-1}	1.21	5.50×10^{-4}

B.2 Fits for ^{154}Nd

For ^{154}Nd in Figure 7.8, the top plot shows the fit assuming that the magnitude is the same as that of ^{151}Nd from M. Guttormsen *et al.* [84], with a pygmy resonance. The blue band fit parameters is shown in Table B.5, while the pink band assumes there is also a constant added, and the fit parameters can be found in Table B.6.

Table B.3 The Generalized Lorentzian GDR fit parameters, including a constant, C, added, as shown as a pink band in the bottom plot of Figure 7.8. This is assuming the magnitude is that of the ^{151}Nd GDR. Here, E is the energy, Γ the width and σ the strength of denoted resonances.

Parameter	μ	σ	μ_{weighted}	σ_{weighted}
σ_{GDR1} (mb)	2.13×10^{2}	2.53	2.13×10^{2}	2.51×10^{-2}
σ_{GDR2} (mb)	1.45×10^{2}	2.47	1.45×10^{2}	2.46×10^{-2}
E_{GDR1} (MeV)	1.34×10	1.02×10^{-1}	1.34×10	1.01×10^{-3}
E_{GDR2} (MeV)	1.65×10	4.00×10^{-1}	1.65×10	3.98×10^{-3}
Γ_{GDR1} (MeV)	6.70	2.65×10^{-1}	6.80	2.64×10^{-3}
Γ_{GDR2} (MeV)	4.00	2.00×10^{-1}	4.01	1.99×10^{-3}
C	1.00×10^{-5}	9.92×10^{-7}	1.00×10^{-5}	9.86E-09

Table B.4 The Generalized Lorentzian GDR fit parameters, as shown as a blue band in the bottom plot of Figure 7.8. This is assuming the magnitude is that of the ^{151}Nd GDR. Here, E is the energy, Γ the width and σ the strength of denoted resonances.

Parameter	μ	σ	μ_{weighted}	σ_{weighted}
σ_{GDR1} (mb)	2.13×10^{2}	2.51	2.13×10^{2}	1.30×10^{-2}
σ_{GDR2} (mb)	1.45×10^{2}	2.52	1.45×10^{2}	1.31×10^{-2}
E_{GDR1} (MeV)	1.34×10	9.59×10^{-2}	1.34×10	4.98×10^{-4}
E_{GDR2} (MeV)	1.65×10	4.01×10^{-1}	1.65×10	2.08×10^{-3}
Γ_{GDR1} (MeV)	6.70	2.10×10^{-1}	6.66	1.09×10^{-3}
Γ_{GDR2} (MeV)	4.00	1.98×10^{-1}	4.00	1.03×10^{-3}

Table B.5 The Generalized Lorentzian GDR fit parameters, including a pygmy resonance as shown as a blue band in the top plot of Figure 7.8 for ^{154}Nd. This is assuming the magnitude is that of the ^{151}Nd γSF from Ref. [84]. Here, E is the energy, Γ the width and σ the strength of denoted resonances.

Parameter	μ	σ	μ_{weighted}	σ_{weighted}
σ_{pygmy} (mb)	5.12×10^{-1}	2.51×10^{-2}	5.11×10^{-1}	1.01×10^{-4}
Γ_{pygmy} (MeV)	1.94	3.88×10^{-2}	1.94	1.56×10^{-4}
E_{pygmy} (MeV)	3.56	8.48×10^{-2}	3.57	3.41×10^{-4}
σ_{GDR1} (mb)	2.13×10^{2}	2.52	2.13×10^{2}	1.01×10^{-2}
σ_{GDR2} (mb)	1.45×10^{2}	2.51	1.45×10^{2}	1.01×10^{-2}
E_{GDR1} (MeV)	1.34×10	9.62×10^{-2}	1.34×10	3.87×10^{-4}
E_{GDR2} (MeV)	1.65×10	4.01×10^{-1}	1.65×10	1.61×10^{-3}
Γ_{GDR1} (MeV)	6.70	2.16×10^{-1}	6.68	8.71×10^{-4}
Γ_{GDR2} (MeV)	4.00	2.03×10^{-1}	4.00	8.19×10^{-4}

Table B.6 The Generalized Lorentzian GDR fit parameters, including a pygmy resonance and a constant, C, added, as shown as a pink band in the top plot of Figure 7.8. This is assuming the magnitude is that of the ^{151}Nd γSF from Ref. [84]. Here, E is the energy, Γ the width and σ the strength of denoted resonances.

Parameter	μ	σ	μ_{weighted}	σ_{weighted}
σ_{pygmy} (mb)	4.10×10^{-1}	2.05×10^{-2}	4.10×10^{-1}	8.30×10^{-5}
Γ_{pygmy} (MeV)	9.72×10^{-1}	1.95×10^{-2}	9.71×10^{-1}	7.89×10^{-5}
E_{pygmy} (MeV)	3.40	8.08×10^{-2}	3.40	3.27×10^{-4}
σ_{GDR1} (mb)	2.13×10^{2}	2.52	2.13×10^{2}	1.02×10^{-2}
σ_{GDR2} (mb)	1.45×10^{2}	2.52	1.45×10^{2}	1.02×10^{-2}
E_{GDR1} (MeV)	1.34×10	9.66×10^{-2}	1.34×10	3.91×10^{-4}
E_{GDR2} (MeV)	1.65×10	3.99×10^{-1}	1.65×10	1.62×10^{-3}
Γ_{GDR1} (MeV)	6.70	2.17×10^{-1}	6.69	8.77×10^{-4}
Γ_{GDR2} (MeV)	3.99	2.02×10^{-1}	4.00	8.18×10^{-4}
C	3.69×10^{-1}	3.68×10^{-2}	3.69×10^{-1}	1.49×10^{-4}

BIBLIOGRAPHY

[1] E. M. Burbidge, G. R. Burbidge, W. A. Fowler, *et al.*, "Synthesis of the elements in stars," *Reviews of Modern Physics*, vol. 29, pp. 547–650, 4 Oct. 1957.

[2] National Nuclear Data Center, *Nudat 3.0 (nuclear structure and decay data)*, Brookhaven National Laboratory, Plot extracted from the NuDat database with permission. Accessed [04/04/26], 2026.

[3] S. J. Ling, J. Sanny, and W. Moebs, *University Physics Volume 3*, [Accessed 2024-06-20] Image is licensed under the CC 4.0. To view a copy of this license, visit http://creativecommons.org/licenses/by/4.0/., Sep. 2022.

[4] T. Kibedi, P. M. Davidson, T. W. Burrows, *et al.*, *Internal conversion coefficients - how good are they now?* Jul. 2008.

[5] C. Dembski, A. Spyrou, B. A. Brown, *et al.*, "Extreme Shape Coexistence observed in ^{70}Co," *Communications Physics*, vol. 8, no. 1, Feb. 2025.

[6] T. Renstrøm, H. Utsunomiya, H. T. Nyhus, *et al.*, "Verification of detailed balance for γ absorption and emission in Dy isotopes," *Physical Review C*, vol. 98, no. 5, pp. 1–14, 2018.

[7] T. Ericson, "The statistical model and nuclear level densities," *Advances in Physics*, vol. 9, no. 36, pp. 425–511, 1960.

[8] L. Moretto, "Thermodynamical properties of a paired nucleus with a fixed number of quasiparticles," *Nuclear Physics A*, vol. 243, no. 1, pp. 77–99, 1975.

[9] V. Zelevinsky, S. Karampagia, and A. Berlaga, "Constant temperature model for nuclear level density," *Physics Letters B*, vol. 783, pp. 428–433, 2018.

[10] M. Guttormsen, M. Aiche, F. L. Bello Garrote, *et al.*, "Experimental level densities of atomic nuclei," *The European Physical Journal A*, vol. 51, no. 12, Dec. 2015.

[11] A. Koning, S. Hilaire, and S. Goriely, *Talys-2.0 simulation of nuclear reactions*, 2024.

[12] S. Goriely, S. Hilaire, and A. J. Koning, "Improved microscopic nuclear level densities within the hartree-fock-bogoliubov plus combinatorial method," *Physical Review C*, vol. 78, p. 064 307, 6 Dec. 2008.

[13] J. Kopecky, *Gamma-ray strength functions*, Aug. 1998.

[14] M. Guttormsen, K. O. Ay, M. Ozgur, *et al.*, *Evolution of the γ-ray strength function in neodymium isotopes*, This work is licensed under the Creative Commons Attribution 4.0 International License. To view a copy of this license, visit http://creativecommons.org/

licenses/by/4.0/., Sep. 2022. arXiv: 2204.08852v2 [nucl-ex].

[15] R. Capote, M. Herman, P. Obložinský, *et al.*, "RIPL – Reference Input Parameter Library for Calculation of Nuclear Reactions and Nuclear Data Evaluations," *Nuclear Data Sheets*, vol. 110, no. 12, pp. 3107–3214, 2009.

[16] K. H. Monjiro, *Scissors Mode in atomic nuclei: the proton (p) and neutron (n) rotors precess around their bisector*, This work is licensed under the Creative Commons Attribution 3.0 International License. To view a copy of this license, visit http://creativecommons.org/licenses/by/3.0/., 2013.

[17] N. L. Iudice and F. Palumbo, "New isovector collective modes in deformed nuclei," *Physical Review Letters*, vol. 41, pp. 1532–1534, 22 Nov. 1978.

[18] D. Bohle, A. Richter, W. Steffen, *et al.*, "New magnetic dipole excitation mode studied in the heavy deformed nucleus 156gd by inelastic electron scattering," *Physics Letters B*, vol. 137, no. 1, pp. 27–31, 1984.

[19] A. Voinov, E. Algin, U. Agvaanluvsan, *et al.*, "Large Enhancement of Radiative Strength for Soft Transitions in the Quasicontinuum," *Phys. Rev. Lett.*, vol. 93, no. 14, p. 142 504, Sep. 2004.

[20] J. E. Midtbø, A. C. Larsen, T. Renstrøm, *et al.*, "Consolidating the concept of low-energy magnetic dipole decay radiation," *Physical Review C*, vol. 98, no. 6, p. 64 321, 2018.

[21] A. C. Larsen, N. Blasi, A. Bracco, *et al.*, "Evidence for the Dipole Nature of the Low-Energy γ Enhancement in ^{56}Fe," *Physical Review Letters*, vol. 111, no. 24, p. 242 504, 2013.

[22] A. Koning and J. Delaroche, "Local and global nucleon optical models from 1 kev to 200 mev," *Nuclear Physics A*, vol. 713, no. 3, pp. 231–310, 2003.

[23] M. Arnould and S. Goriely, "The p-process of stellar nucleosynthesis: Astrophysics and nuclear physics status," *Physics Reports*, vol. 384, no. 1, pp. 1–84, 2003.

[24] J. J. Cowan and W. K. Rose, "Production of C-14 and neutrons in red giants," en, *The Astrophysical Journal*, vol. 212, p. 149, Feb. 1977.

[25] R. Reifarth, C. Lederer, and F. Käppeler, *Neutron reactions in astrophysics*, This work is licensed under the Creative Commons Attribution 3.0 International License. To view a copy of this license, visit http://creativecommons.org/licenses/by/3.0/, Mar. 2014. arXiv: 1403.5670v1 [astro-ph].

[26] M. R. Drout, A. L. Piro, B. J. Shappee, *et al.*, "Light curves of the neutron star merger gw170817/sss17a: Implications for r-process nucleosynthesis," *Science*, vol. 358, no. 6370, pp. 1570–1574, 2017. eprint: https://www.science.org/doi/pdf/10.1126/science.aaq0049.

[27] M. Asplund, D. L. Lambert, T. Kipper, *et al.*, "The rapid evolution of the born-again giant sakurai's object," *Astronomy and Astrophysics*, vol. 343, pp. 507–518, Mar. 1999.

[28] L. Dardelet, C. Ritter, P. Prado, *et al.*, "I process and CEMP-s+r stars," in *Proceedings of XIII Nuclei in the Cosmos — PoS(NIC XIII)*, Debrecen, Hungary: Sissa Medialab, Oct. 2015.

[29] P. A. Denissenkov, F. Herwig, P. Woodward, *et al.*, "The i-process yields of rapidly accreting white dwarfs from multicycle he-shell flash stellar evolution models with mixing parametrizations from 3d hydrodynamics simulations," *Monthly Notices of the Royal Astronomical Society*, vol. 488, no. 3, pp. 4258–4270, Jul. 2019. eprint: https://academic.oup.com/mnras/article-pdf/488/3/4258/29110443/stz1921.pdf.

[30] F. Herwig, M. Pignatari, P. R. Woodward, *et al.*, "Convective-reactive proton-12c combustion in sakurai's object (v4334 sagittarii) and implications for the evolution and yields from the first generations of stars," *The Astrophysical Journal*, vol. 727, no. 2, p. 89, Feb. 2011.

[31] I. U. Roederer, A. I. Karakas, M. Pignatari, *et al.*, "The diverse origins of neutron-capture elements in the metal-poor star hd 94028: Possible detection of products of i-process nucleosynthesis," *The Astrophysical Journal*, vol. 821, no. 1, p. 37, Apr. 2016.

[32] P. A. Denissenkov, F. Herwig, G. Perdikakis, *et al.*, "The impact of (n,γ) reaction rate uncertainties of unstable isotopes on the i-process nucleosynthesis of the elements from Ba to W," *Monthly Notices of the Royal Astronomical Society*, vol. 503, no. 3, pp. 3913–3925, Mar. 2021. eprint: https://academic.oup.com/mnras/article-pdf/503/3/3913/36856479/stab772.pdf.

[33] Choplin, A., Siess, L., and Goriely, S., "The intermediate neutron capture process - iii. the i-process in agb stars of different masses and metallicities without overshoot," *Astronomy & Astrophysics*, vol. 667, A155, 2022.

[34] A. Choplin, S. Goriely, L. Siess, *et al.*, "Synthesis of actinides and short-lived radionuclides during i-process nucleosynthesis in agb stars," *The European Physical Journal A*, vol. 61, no. 4, Mar. 2025.

[35] M. Wiedeking, S. Goriely, M. Guttormsen, *et al.*, "Unlocking i-process nucleosynthesis by bridging stellar and nuclear physics," *Nature Reviews Physics*, vol. 7, no. 12, pp. 696–712, Nov. 2025.

[36] A. Abohalima and A. Frebel, "JINAbase—A Database for Chemical Abundances of Metal-poor Stars," *The Astrophysical Journal Supplement Series*, vol. 238, no. 2, p. 36, Oct. 2018.

[37] F. Herwig, P. Denissenkov, and O. Clarkson, *A classification of cemp stars based on neutron density that reveals the important role of the i process and the need for better nuclear physics data*, This work is licensed under the Creative Commons Attribution 4.0 International License. To view a copy of this license, visit http://creativecommons.org/licenses/by/4.0/.,

Sep. 2019.

[38] A. Spyrou, D. Mücher, P. A. Denissenkov, *et al.*, "First study of the ^{139}Ba$(n,\gamma)^{140}$Ba reaction to constrain the conditions for the astrophysical *i* process," *Physical Review Letters*, vol. 132, p. 202 701, 20 May 2024.

[39] R. H. Cyburt, A. M. Amthor, R. Ferguson, *et al.*, "The jina reaclib database: Its recent updates and impact on type-i x-ray bursts," *The Astrophysical Journal Supplement Series*, vol. 189, no. 1, p. 240, Jun. 2010.

[40] Goriely, S., Hilaire, S., and Koning, A. J., "Improved predictions of nuclear reaction rates with the talys reaction code for astrophysical applications*," *Astronomy & Astrophysics*, vol. 487, no. 2, pp. 767–774, 2008.

[41] A. Koning and D. Rochman, "Modern nuclear data evaluation with the talys code system," *Nuclear Data Sheets*, vol. 113, no. 12, pp. 2841–2934, 2012, Special Issue on Nuclear Reaction Data.

[42] J. A. Johnson and M. Bolte, "The s-process in metal-poor stars: Abundances for 22 neutron-capture elements in cs 31062-050*," *The Astrophysical Journal*, vol. 605, no. 1, p. 462, Apr. 2004.

[43] P. Denissenkov, Private communication, Feb. 2021.

[44] R. Vondrasek, J. Clark, A. Levand, *et al.*, "Operational experience with the Argonne National Laboratory Californium Rare Ion Breeder Upgrade facility and electron cyclotron resonance charge breeder," *Review of Scientific Instruments*, vol. 85, no. 2, 2014.

[45] C. J. Prokop, S. N. Liddick, B. L. Abromeit, *et al.*, "Digital data acquisition system implementation at the national superconducting cyclotron laboratory," *Nuclear Instruments and Methods in Physics Research Section A: Accelerators, Spectrometers, Detectors and Associated Equipment*, vol. 741, pp. 163–168, 2014.

[46] Argonne National Laboratory, *CARIBU Beams*, https://www.anl.gov/atlas/caribu-beams, [Accessed 09-07-2023], 2023.

[47] Argonne National Laboratory, *ATLAS Facility Layout with Beam Locations*, https://www.anl.gov/atlas/reference/atlas-facility-layout-with-beam-locations, [Accessed 12 – 02 – 2024], 2021.

[48] A. Simon, S. J. Quinn, A. Spyrou, *et al.*, "SuN: Summing NaI(Tl) gamma-ray detector for capture reaction measurements," *Nuclear Instruments and Methods in Physics Research Section A: Accelerators, Spectrometers, Detectors and Associated Equipment*, vol. 703, pp. 16–21, 2013.

[49] C. M. Harris, M. K. Smith, A. Spyrou, *et al.*, "Suntan: A new tape-transport system for β-decay experiments," *Nuclear Instruments and Methods in Physics Research Section A: Accelerators, Spectrometers, Detectors and Associated Equipment*, vol. 1084, p. 171 185, 2026.

[50] E. Browne and J. Tuli, "Nuclear data sheets for A = 60," *Nuclear Data Sheets*, vol. 114, no. 12, pp. 1849–2022, 2013.

[51] C. Nesaraja, "Nuclear data sheets for A = 241," *Nuclear Data Sheets*, vol. 130, pp. 183–252, 2015.

[52] M. Basunia, "Nuclear data sheets for A = 237," *Nuclear Data Sheets*, vol. 107, no. 8, pp. 2323–2422, 2006.

[53] K. Abusaleem, "Nuclear data sheets for A = 228," *Nuclear Data Sheets*, vol. 116, pp. 163–262, 2014.

[54] E. Browne and J. Tuli, "Nuclear data sheets for a = 220," *Nuclear Data Sheets*, vol. 112, no. 4, pp. 1115–1161, 2011.

[55] S.-C. Wu, "Nuclear data sheets for a = 216," *Nuclear Data Sheets*, vol. 108, no. 5, pp. 1057–1092, 2007.

[56] K. Auranen and E. A. McCutchan, "Nuclear data sheets for a=212," *Nuclear Data Sheets*, vol. 168, pp. 117–267, 2020.

[57] M. Martin, "Nuclear data sheets for a = 208," *Nuclear Data Sheets*, vol. 108, no. 8, pp. 1583–1806, 2007.

[58] E. Browne and J. Tuli, "Nuclear Data Sheets for A = 137," *Nuclear Data Sheets*, vol. 108, no. 10, pp. 2173–2318, 2007.

[59] M. Martin, "Nuclear data sheets for A = 152," *Nuclear Data Sheets*, vol. 114, no. 11, pp. 1497–1847, 2013.

[60] C. Reich, "Nuclear data sheets for A = 154," *Nuclear Data Sheets*, vol. 110, no. 10, pp. 2257–2532, 2009.

[61] A. Schiller, L. Bergholt, M. Guttormsen, *et al.*, "Extraction of level density and γ strength function from primary γ spectra," *Nuclear Instruments and Methods in Physics Research Section A: Accelerators, Spectrometers, Detectors and Associated Equipment*, vol. 447, no. 3, pp. 498–511, 2000. arXiv: 9910009 [nucl-ex].

[62] P. A. Moldauer, "Why the hauser-feshbach formula works," *Physical Review C*, vol. 11, pp. 426–436, 2 Feb. 1975.

[63] M. Markova, A. C. Larsen, G. M. Tveten, *et al.*, "Nuclear level densities and γ-ray strength functions of ^{111,112,113}Sn isotopes studied with the oslo method," *Physical Review C*, vol. 108, p. 014 315, 1 Jul. 2023.

[64] V. W. Ingeberg, S. Siem, M. Wiedeking, *et al.*, "First application of the oslo method in inverse kinematics," *The European Physical Journal A*, vol. 56, no. 2, Feb. 2020.

[65] H. C. Berg, "Solving the mysteries of ^{133}Xe with inverse kinematics," M.S. thesis, University of Oslo, 2019.

[66] T. K. Olafsen, "The γ-ray strength function and nuclear level density in ^{85}Kr," M.S. thesis, University of Oslo, 2022.

[67] N. D. Pathirana, R. G. T. Zegers, B. Gao, *et al.*, "Extraction of neutron-capture cross sections on ^{92}zr using the charge-exchange oslo method," *Physical Review C*, Dec. 2025.

[68] A. Spyrou, S. N. Liddick, A. C. Larsen, *et al.*, "Novel technique for constraining r -process (n, γ) reaction rates," *Physical Review Letters*, vol. 113, no. 23, pp. 1–5, 2014.

[69] M. Guttormsen, T. Tveter, L. Bergholt, *et al.*, "The unfolding of continuum γ-ray spectra," *Nuclear Instruments and Methods in Physics Research Section A: Accelerators, Spectrometers, Detectors and Associated Equipment*, vol. 374, no. 3, pp. 371–376, 1996.

[70] M. Guttormsen, T. Ramsøy, and J. Rekstad, "The first generation of γ-rays from hot nuclei," *Nuclear Instruments and Methods in Physics Research Section A: Accelerators, Spectrometers, Detectors and Associated Equipment*, vol. 255, no. 3, pp. 518–523, 1987.

[71] S. N. Liddick, A. Spyrou, B. P. Crider, *et al.*, "Experimental neutron capture rate constraint far from stability," *Physical Review Letters*, vol. 116, p. 242 502, 24 May 2016.

[72] S. Agostinelli, J. Allison, K. Amako, *et al.*, "GEANT4—a simulation toolkit," *Nuclear Instruments and Methods in Physics Research Section A: Accelerators, Spectrometers, Detectors and Associated Equipment*, vol. 506, no. 3, pp. 250–303, 2003.

[73] J. Allison, K. Amako, J. Apostolakis, *et al.*, "Geant4 developments and applications," *IEEE Transactions on Nuclear Science*, vol. 53, no. 1, pp. 270–278, 2006.

[74] J. Allison, K. Amako, J. Apostolakis, *et al.*, "Recent developments in geant4," *Nuclear Instruments and Methods in Physics Research Section A: Accelerators, Spectrometers, Detectors and Associated Equipment*, vol. 835, pp. 186–225, 2016.

[75] A. C. Larsen, J. E. Midtbø, M. Guttormsen, *et al.*, "Enhanced low-energy γ-decay strength of ^{70}Ni and its robustness within the shell model," *Physical Review C*, vol. 97, p. 054 329, 5 May 2018.

[76] D. M. Brink, "Some aspects of the interaction of fields with matter," Ph.D. dissertation, Oxford University, 1955.

[77] P. Axel, "Electric Dipole Ground-State Transition Width Strength Function and 7-Mev Photon Interactions," *Physical Review*, vol. 126, no. 2, pp. 671–683, Apr. 1962.

[78] M. Markova, P. von Neumann-Cosel, A. C. Larsen, *et al.*, "Comprehensive test of the brink-axel hypothesis in the energy region of the pygmy dipole resonance," *Physical Review Letters*, vol. 127, p. 182 501, 18 Oct. 2021.

[79] D. Mücher, A. Spyrou, M. Wiedeking, *et al.*, "Extracting model-independent nuclear level densities away from stability," *Physical Review C*, vol. 107, p. L011602, 1 Jan. 2023.

[80] B. Singh, "Nuclear data sheets for a = 151," *Nuclear Data Sheets*, vol. 110, no. 1, pp. 1–264, 2009.

[81] N. Nica, "Nuclear data sheets for A = 153," *Nuclear Data Sheets*, vol. 170, pp. 1–498, 2020.

[82] J. E. Midtbø, F. Zeiser, E. Lima, *et al.*, "A new software implementation of the oslo method with rigorous statistical uncertainty propagation," *Computer Physics Communications*, vol. 262, p. 107 795, 2021.

[83] M. Guttormsen, Y. Alhassid, W. Ryssens, *et al.*, "Strong enhancement of level densities in the crossover from spherical to deformed neodymium isotopes," *Physics Letters B*, vol. 816, p. 136 206, 2021.

[84] M. Guttormsen, K. O. Ay, M. Ozgur, *et al.*, "Evolution of the γ-ray strength function in neodymium isotopes," *Physical Review C*, vol. 106, p. 034 314, 3 Sep. 2022.

[85] M. Guttormsen, F. Zeiser, J. E. Midtbø, *et al.*, *Oslocyclotronlab/oslo-method-software: Oslo method v1.1.6*, version v1.1.6, Feb. 2022.

[86] S. Hilaire, M. Girod, S. Goriely, *et al.*, "Temperature-dependent combinatorial level densities with the d1m gogny force," *Phys. Rev. C*, vol. 86, p. 064 317, 6 Dec. 2012.

[87] T. RAUSCHER and F.-K. THIELEMANN, "Tables of nuclear cross sections and reaction rates: An addendum to the paper "astrophysical reaction rates from statistical model calculations"," *Atomic Data and Nuclear Data Tables*, vol. 79, no. 1, pp. 47–64, 2001.

[88] P. Denissenkov, S. Baltaci, S. Coil, *et al.*, "Constraining i-process nucleosynthesis through first-peak element abundances in cemp stars," From private communication., 2025.

[89] P. Denissenkov, Private communication, Feb. 2026.